Surface Modification of Hydrogen-Terminated Silicon Nanoparticles

A DISSERTATION
SUBMITTED TO THE FACULTY OF THE GRADUATE SCHOOL
OF THE UNIVERSITY OF MINNESOTA
BY

Jason Daniel Holm

IN PARTIAL FULFILLMENT OF THE REQUIREMENTS
FOR THE DEGREE OF
DOCTOR OF PHILOSOPHY

Prof. Jeffrey T. Roberts, Adviser
Prof. Uwe R. Kortshagen, Adviser

September 2009

Acknowledgements

Thanks to the following people are in order: Amanda Niwnow and Ying-Chih Liao for assistance with TDMA measurements, Greg Haugstad for assistance with ToF-SIMS measurements, Bing Luo for assistance with particle refluxing and characterization by NMR, John H. Thomas, III for assistance with XPS measurements and spectral interpretation, Melissa Fierke for assistance with DSC measurements, Yuriy Nesmelov for assistance with EPR characterization, and Ozan Ugurlu for assistance with TEM. Thanks also to Prof. Jeffrey Roberts and Prof. Uwe Kortshagen for providing the opportunity and resources to perform this research.

Table of Contents

List of Tables

List of Figures

List of Schemes

Nomenclature

DRIFTS	Diffuse reflectance infrared Fourier transform spectrometry
DSC	Differential scanning calorimetry
FTIR	Fourier transform infrared spectroscopy
HEPA	High efficiency particulate air
LO	Longitudinal optical
nDMA	Nano differential mobility analyzer
NMR	Nuclear magnetic resonance
RF	Radio-frequency
TDMA	Tandem differential mobility analysis
TEM	Transmission electron microscope
TO	Transverse optical
ToF-SIMS	Time-of-flight secondary ion mass spectroscopy
UCPC	Ultrafine condensation particle counter
XPS	X-ray photoelectron spectroscopy
XRD	X-ray diffraction

Previously Published Work

Chapter 2 has been previously published and is reproduced in part with permission from the Journal of the American Chemical Society, Copyright 2007, American Chemical Society. (Holm, J. and Roberts, J. T. *J. Am. Chem. Soc.*, **2007**, *129* (9), pp 2496–2503.)

Chapter 3 has been previously published and is reproduced in part with permission from Langmuir, Copyright 2007, American Chemical Society. (Holm, J. and Roberts, J. T. *Langmuir*, **2007**, *23* (22), pp 11217–11224.)

Chapter 4 has been previously published and is reproduced in part with permission from Langmuir, Copyright 2009, American Chemical Society. (Holm, J. and Roberts, J. T. *Langmuir*, **2009**, *25* (12), pp 7050–7056.)

Chapter 6 has been previously published and is reproduced in part with permission from the Journal of Physical Chemistry C, Copyright 2009, American Chemical Society. (Holm, J. and Roberts, J. T. *J. Phys. Chem. C* **2009**, *113* (36), pp 15955–15963.)

Chapter 1.

Introduction

One of the original purposes of this work was to create a continuous process in which nanoparticles could be synthesized, surface tailored, and then characterized using aerosol-based techniques. Because the particle synthesis process was initially thought to be developed sufficiently well, the primary thrust of this work was to focus on tailoring and then characterizing the modified silicon particles. Two particle surface tailoring schemes were to be employed. The first was thermal oxidation by molecular oxygen in conjunction with a flow tube furnace. The second was thermally promoted hydrosilylation, a reaction commonly employed in solution-based processes. As a start, uptake of relatively simple organic molecules (e.g., 1-alkenes and 1-alkynes) at the particle surfaces was studied, and the efficacy of different parameters – particle size, particle preheating temperature, reaction zone temperature, aerosol residence time in the tube furnace, organic precursor partial pressure, and reactant type and molecular weight – were investigated. Of those parameters, only particle preheating temperature showed promise. For example, regardless of the other parameter settings, preliminary results demonstrated that a temperature of 700 °C or greater was required to elicit notable uptake of organic precursors as suggested by *in situ* FTIR spectra. This was not necessarily a problem in and of itself. However, one of the desirable characteristics of the silicon nanoparticles, visible photoluminescence under UV irradiation, was eliminated when the particles were heated to temperatures greater than ~500 °C. Therefore, a more thorough understanding of how the particles changed with applied heat was deemed necessary.

Much of the experimental work described in this dissertation focuses on how hydrogen terminated silicon nanoparticles change when they are heated. In particular, changes in conformation of hydrogen at particle surfaces are investigated, and consequences for surface tailoring are considered. The particle synthesis technique (a continuous-flow non-thermal RF plasma) and its ability to impart different conformations of silicon-hydrogen functionality at particle surfaces is experimentally examined, and the radical chain propagation step of thermally induced hydrosilylation is also considered. Although each of the following chapters reads as an independent entity, they are interrelated in that each provides further insight into how the particle surfaces can be manipulated in ways consistent with reaching a long term goal of tailoring silicon particle surfaces in continuous aerosol-based processes.

The dissertation is organized as follows. Chapter 2 focuses on thermally-induced hydrogen desorption from particle surfaces. Several traditional and nontraditional materials characterization techniques are employed to gain a more thorough understanding of how particles change as hydrogen is driven from the surfaces. Chapter 3 focuses on thermal oxidation. Particles are oxidized by molecular oxygen in a flow tube reactor, and oxide growth and composition is characterized as a function of temperature. Chapter 4 focuses on the hydrosilylation reaction mechanism. Specifically, isotopic substitution techniques are employed to examine how the reaction propagates on silicon nanoparticle surfaces. This chapter is different from the others in that solution phase processing is used to modify the particle surfaces rather than gas/aerosol phase processing. In addition to describing evidence suggesting that the reaction propagates through a radical chain process, the influence of the initial state of silicon hydride

functional groups adsorbed at particle surfaces and its effect on the proposed reaction scheme is considered. Chapter 5 is a follow-up to Chapter 4 in that the focus is on using the plasma to control the silicon-hydrogen functionality at particle surfaces. This chapter describes several ways that the plasma reactor can be used to change states of adsorbed hydrogen at particles surfaces, and in some instances how the reactor can provide a particle surface composition that could be more amenable to modification by hydrosilylation. Chapter 6 focuses on sintering and coalescence of hydrogen-terminated silicon nanoparticles. Hydrogen is shown to persist at particle surfaces well above the experimentally reported melting temperature of the silicon nanoparticles. The significance of the persistent surface hydrogen is considered. Chapter 7 summarizes the major conclusions derived from this work and provides brief recommendations for future efforts.

This document deviates somewhat from the traditional dissertation format. Since the document is primarily composed of published or nearly published reports, an entire chapter specifically dedicated to a review of the pertinent literature is not included. The relevant literature specific to each chapter is presented in the introductory paragraphs of the respective chapter.

Chapter 2.

Surface Chemistry of Aerosolized Silicon Nanoparticles: Evolution and Desorption of Hydrogen from 6 nm Diameter Particles

The surface chemistry of fresh, 6-nm silicon nanoparticles has been investigated. The particles were produced in an RF plasma and studied using a tandem differential mobility analysis (TDMA) apparatus, Fourier transform infrared spectroscopy (FTIR), time-of-flight secondary ion mass spectrometry (ToF-SIMS), and transmission electron microscopy (TEM). Particles were extracted from the plasma, which operates at ~20 Torr, into an atmospheric pressure aerosol flow tube, and then through a variable-temperature furnace that could be adjusted between room temperature and 1200 °C. DMA measurements show freshly generated silicon particles shrink with heating, with particle diameters decreasing by ~0.25 nm between 350 and 400 °C. FTIR results indicate freshly generated particles are primarily covered with SiH_2 groups and smaller amounts of SiH and SiH_3. Spectra recorded as a function of heating temperature indicate the amount of surface hydrogen, as measured by the intensity of modes associated with SiH, SiH_2, and SiH_3, decreases with heating. ToF-SIMS measurements also suggest that hydrogen desorbs from the particle surfaces over the same temperature range that the particles shrink.

2.1 Introduction

Silicon nanoparticles are receiving attention for diverse applications such as luminescent devices,[2.1] non-toxic biological markers,[2.2] and single particle transistors,[2.3] and for improving photovoltaic conversion in hydrogenated, amorphous silicon (a-Si:H) solar cells.[2.4] Because many proposed applications rely on particle size control, accurately monitoring, manipulating, and preserving individual particle sizes are all of critical importance. Additionally, many applications require specifically functionalized particle surfaces to elicit desired characteristics or responses. Knowledge of the pristine nanoparticle surface chemistry is therefore of interest. By determining the particle surface chemistry, one may also gain valuable insight into appropriate functionalization techniques and materials. For instance, hydrosilylation is well-established as a method for providing organic functionalization to the surface of silicon wafers.[2.5-2.8] Because hydrosilylation involves the reaction of an organic modifying agent with one or more surface Si–H bonds, the nature of a pristine surface, and in particular the coverage and state of adsorbed hydrogen, will partly determine whether hydrosilylation is an appropriate functionalization strategy.

Particle mobility diameter changes in the aerosol phase are often measured by tandem differential mobility analysis (TDMA).[2.9] The technique has frequently been used to evaluate size distribution changes due to volatization of atmospheric aerosols,[2.10] and, more recently, growth of silicon nanoparticles due to thermal oxidation[2.11] and uptake of organic molecules on silicon nanoparticles.[2.12] During the thermal oxidation experiments,[2.11] a small decrease in electrical mobility diameter was consistently observed when the particles were heated to temperatures greater than ~350-400 °C in

nonreactive gases (N_2 or Ar). This temperature range is consistent with reports of hydrogen evolution from silicon nanoparticles,[2.13] porous silicon,[2.14] and extended crystalline silicon surfaces.[2.15]

Although the particles produced by the technique used here (a non-thermal RF plasma method) were previously thought to be hydrogen-terminated, a detailed examination of the pristine surface chemistry as a function of temperature has not been reported until now. In this chapter, a method of characterizing the surface chemistry of aerosolized Si nanoparticles is described. The particle surface composition as a function of temperature is evaluated using both Fourier transform infrared spectroscopy (FTIR) and static time-of-flight secondary ion mass spectroscopy (ToF-SIMS). Effects of temperature on particle morphology, as monitored by transmission microscopy (TEM) are described. A concomitant relationship between electrical mobility diameter, morphology, surface chemistry, and temperature is also presented.

2.2 Experimental

Hydrogen-terminated silicon nanoparticles were produced in an RF plasma using a method similar to that outlined by Magolini et al.[2.16] Crystalline particles are produced by this technique, as demonstrated in that report and elsewhere.[2.12,2.17] Briefly, particle synthesis proceeded as follows. SiH_4 (0.5% in Ar) obtained from BOC Edwards was mixed with ultrahigh purity argon (PraxAir, St. Paul, MN) before being introduced into a low-pressure, non-thermal, quartz tube plasma reactor. Gas flows were 5–10 sccm of the SiH_4/Ar mixture and 400 sccm of ultrahigh purity Ar. RF power at 13.56 MHz was coupled to a 10-mm i.d. (12-mm o.d.) quartz tube reactor using two ring electrodes and a

matching network as shown in Figure 2.1. The RF amplifier was an Electronics & Innovation Model A150 and the signal generator was a Tektronics AFG3021. Power output from the amplifier was approximately 30 W.

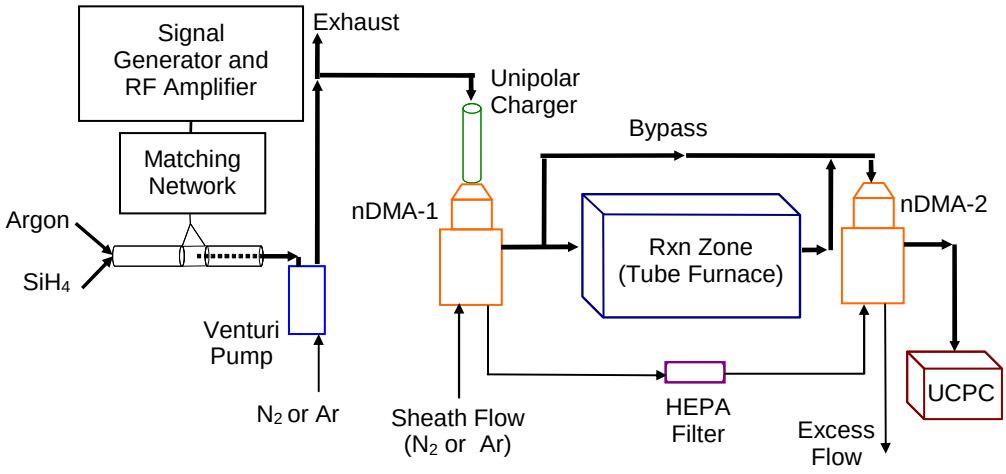

Figure 2.1 Experimental setup for particle synthesis and mobility measurements.

Silicon nanoparticles were formed at a plasma pressure of ~20 Torr. The pressure was controlled using one of two methods depending on the particular analysis technique. For FTIR measurements and ToF-SIMS sample collection, a Model 1400 Welch vacuum pump was used. An Air-Vac Model UV143H two-stage venturi pump was used in conjunction with TDMA measurements. The venturi pump also served as the means by which the particles were brought from the plasma operating pressure up to atmospheric pressure. Essentially, the venturi pump created a low-pressure region by quickly forcing a large volume of gas through a small diameter passage. A port tapped into the small diameter passage served as the vacuum source. This port was coupled directly to the plasma reactor tube, allowing the plasma to run at ~20 Torr. Particles flowing from the

plasma through the venturi pump became entrained in the rapidly flowing gas and were diluted, thus minimizing coagulation. The aerosolized particles in the venturi pump exhaust flow were vented to a larger diameter atmospheric pressure exhaust line from which the aerosol sample was extracted. Gas vent lines from either liquid argon or liquid nitrogen cylinders (Praxair, St. Paul, MN) were used to obtain the volumetric flow rates required to reach the desired pressure.

Changes in particle mobility diameter as a function of temperature were measured using the TDMA apparatus shown schematically in Figure 2.1. Both DMAs were Model 3085 nano DMAs (TSI, Inc., Shorewiew, MN) and the particle counter was an ultrafine condensation particle counter (UCPC) Model 3025A (TSI, Inc.). A unipolar aerosol diffusion charger similar to one developed by Chen and Pui[2.18] was used to charge the particles which is required for TDMA analysis. Flow rate ratios in the TDMA apparatus were maintained at 10:1. Sheath and aerosol gases were identical for each set of measurements to avoid potential diffusiophoretic effects[2.19] and further restricted to either nitrogen or argon to minimize reactions between carrier gas and pristine silicon nanoparticles. Electrode voltages were calculated using room temperature air properties. No modifications were made for viscosity, mean free path, or slip correction when switching between nitrogen and argon.

The TDMA measurements described here were obtained as follows. Aerosol flow was extracted from the atmospheric pressure venturi pump exhaust at 1 L/min in a direction perpendicular to the main exhaust flow. Sampling in this configuration may be considered anisokinetic and could result in a particle size distribution slightly different than that produced by the plasma. However, although the apparatus can certainly be

adjusted to make isokinetic sampling feasible, the intent here was not to accurately measure particle size distributions produced by the plasma. As such, the current configuration allowed sampling of a sufficient number of particles so that mobility diameter changes due to thermal processing could be examined.

The aerosol sample was immediately introduced into the unipolar charger where particles acquired at most a single charge. (Multiple charging is not expected to occur for particles of diameter less than 20 nm.) For these experiments, positively charged particles were selected for analysis. The aerosol was then directed into the first nDMA, where by adjusting the applied voltage, particles of a specific narrow electrical mobility band were selected for analysis. Those particles selected by the first nDMA were passed through either a single zone tube furnace (Lindberg/Blue Model # HTF 55122A) or an equivalent length bypass line into the second nDMA. Tubes used in the furnace were either 12-mm o.d. (10 mm i.d.) quartz or 12.7 mm o.d. (11 mm i.d.) Inconel 600. Furnace settings ranged from room temperature to 950 °C. Representative furnace temperature profiles are shown in Figure 2.2. Radiation heating effects were examined in a previous report using shielded and unshielded type k thermocouples.[2.20] No significant temperature profile differences were found between shielded and unshielded measurements.

The second nDMA electrode voltage was incrementally stepped over the range of particle mobilities, and particle number concentrations were measured at each voltage with the UCPC. Those number concentration measurements were combined to form representative particle mobility diameter distributions. A normal Gaussian curve was fit to each distribution using the Levenberg–Marquardt algorithm, and the center of each

fitted curve was denoted as the equivalent mobility diameter. At each furnace temperature setting, particle size distributions from both the bypass and the furnace were measured a minimum of three times and averaged.

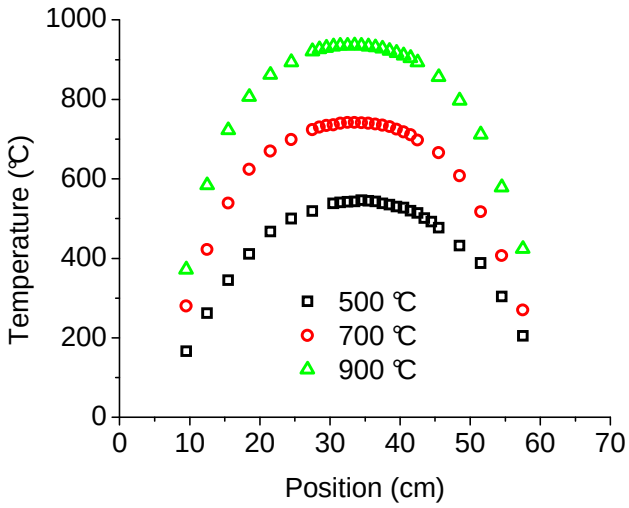

Figure 2.2. Tube furnace temperature profiles for three different furnace settings. Profiles were measured with a sheathed k-type thermocouple and 1 L/min nitrogen flow to replicate aerosol flow reactor operating conditions.

Particle surface composition was characterized as a function of temperature using an FTIR spectrometer and static ToF-SIMS. FTIR spectra were obtained in the transmission mode using a Magna-IR, Model 550 Spectrometer. With the plasma off, the FTIR spectrometer readily detected SiH_4 in the SiH_4/Ar gas mixture over a path length of 15 cm. With the plasma on, however, no statistically meaningful signal from the SiH_4 or the Si nanoparticles was detected over the same length. Therefore, to characterize the pristine nanoparticle surface chemistry without exposure to air, and to minimize particle losses due to diffusion, a small hybrid gas cell was constructed. This technique provided

a means of simultaneously analyzing particle surface chemistry while collecting particles for future stability characterization after exposure to various atmospheres.

To collect a sufficient quantity of particles for FTIR analysis, a piece of fine stainless steel (SST) mesh was mounted perpendicular to the aerosol flow between two short sections of stainless steel tube. (Any suitable IR-transparent filter media could work in place of SST mesh.) The tubes were connected with a quick-flange style clamp. ZnSe windows were mounted on the outer end of each tube to seal the apparatus while simultaneously allowing the IR beam to pass through the hybrid gas cell and mesh. Ports were attached to each tube section on opposite sides of the mesh to provide an inlet and outlet through which the particle-laden gas could flow. As the particles from the plasma reactor flowed through the modified gas cell, a thin layer of silicon nanoparticles accumulated on the mesh. Samples were collected on clean pieces of mesh for a minimum of 20 minutes before final spectra were recorded. Under the flow conditions used here, the average amount of collected mass was ~0.3 mg.

Samples for ToF-SIMS (Charles Evans and Associates) analysis were also collected on SST mesh in a similar manner. However, samples were kept in their as-produced environment during transport to the instrument by sealing the small gas cell with two valves. This was done to minimize adventitious reactions resulting from exposure to ambient air before loading into the ToF-SIMS analysis chamber. The incident ion beam was gallium, chamber pressure for these measurements was approximately 2 (10^{-8}) Torr, and the extraction voltage was 15 kV. Positive ion spectra were recorded.

Polydisperse particles were collected on carbon TEM grids either by use of an electrostatic sampling device or by impaction. A Tecnai T12 transmission electron microscope (FEI Co., Hilsboro, OR) operating at 120 kV was used to obtain particle images.

2.3 Results

Typical particle mobility diameter distributions measured with components of the TDMA apparatus are shown in Figure 2.3. The diameters in the nonsymmetric overall distribution range from 4 nm to 20 nm, with the most probable diameter near 10 nm. The 6-nm selected distributions are symmetric. As shown by the TEM image in Figure 2.4, particles sampled from the polydisperse aerosol are essentially spherical and non-agglomerated.

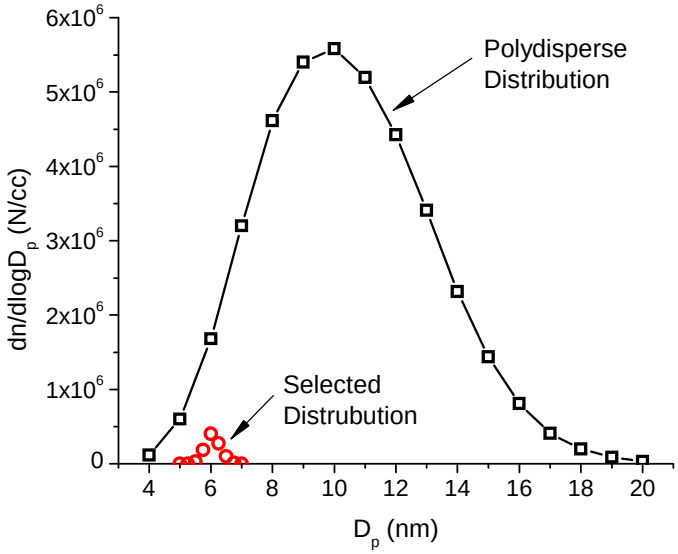

Figure 2.3. A typical polydisperse distribution prior to mobility selection and a selected distribution corresponding to 6 nm particles.

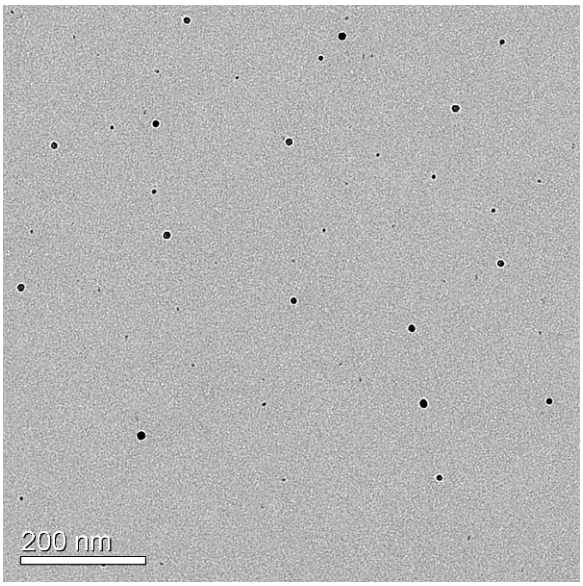

Figure 2.4. TEM image showing particles collected without size-classification from the venturi pump exhaust. Particles are discrete and essentially spherical.

As an indication of repeatability and distribution changes due to thermal processing, number concentration measurements corresponding to particles heated to 500 °C in nitrogen carrier gas are shown in Figure 2.5. Measurements from the bypass closely overlap as do those from the furnace. Because the particles examined here are less than 20 nm in diameter, they acquire a single charge at most in the unipolar charger, and therefore the contribution of doubly charged particles to the distributions is unimportant.

Measured mobility diameter changes as a function of furnace setting are summarized in Figure 2.6 for particles of 6-nm selected mobility in Ar and N_2 carrier gases. Diameters begin to decrease at 300 °C, and by 400 °C, diameter decreases are 0.25 nm. Although not shown, the same decrease is observed, within experimental error, for 10-nm particles. Between 400 and 600 °C, the change in particle diameter is constant.

Above 600 °C an additional decrease occurs, with total shrinkage increasing to 0.3–0.35 nm between 700 and 800 °C. Particles flowing through the bypass line show negligible diameter changes. With the exception of the highest furnace settings studied, distribution dispersity was essentially constant with a distribution full width at half-maximum (fwhm) of ~0.6 nm.

As shown in Figure 2.6, mobility diameters measured in nitrogen are generally slightly larger than those measured in argon. However, *differences* in mobility diameter between particles sent through the bypass and those sent through the tube furnace at selected furnace settings are more relevant to the immediate discussion rather than the ultimate TDMA sizing accuracy. If only those diameter differences are considered, then measurements in nitrogen and argon indicate that results are identical, within experimental error. They support the precision of the TDMA apparatus when used to measure very small aerosol size distribution changes in different carrier gases.[2.21]

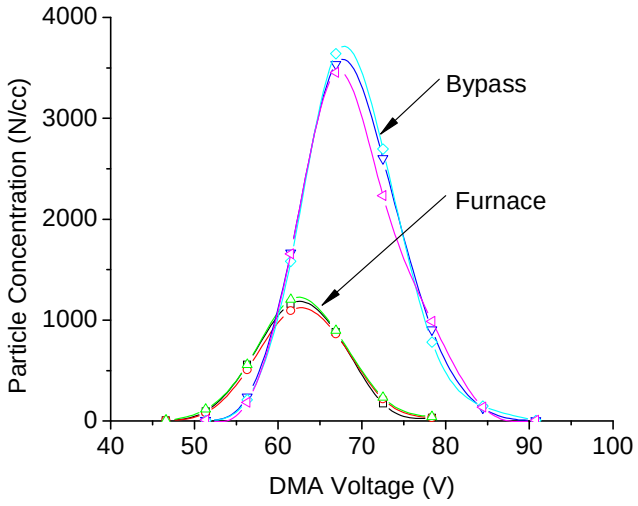

Figure 2.5. Particle number concentration distributions at 500 °C in nitrogen.

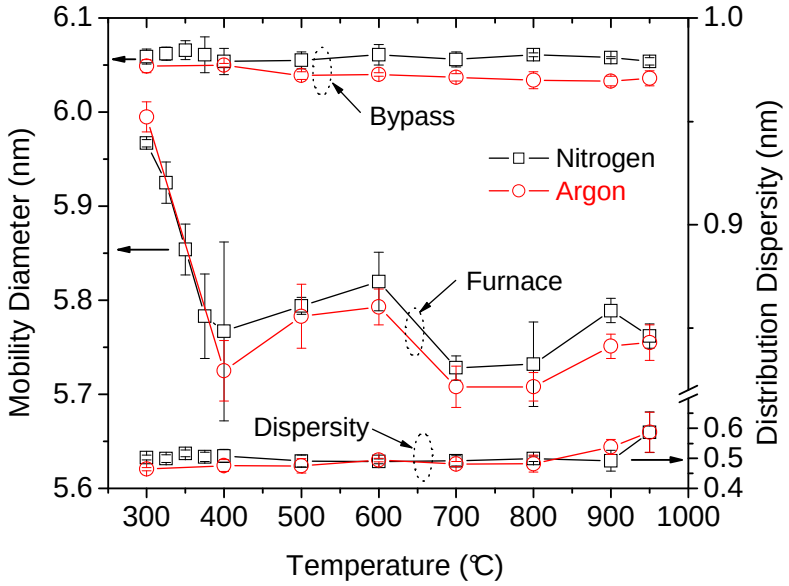

Figure 2.6. Particle mobility diameter in argon and nitrogen carrier gases as a function of furnace temperature setting. Measurements from the bypass line are nearly constant at approximately 6.05 nm. Dispersity refers to widths of size-selected particle distributions passed through the furnace. (FWHM = 1.175 * Dispersity.)

Two prominent signals are visible in FTIR spectra of collected particles, of which representative examples are shown in Figure 2.7. One of the bands is centered near 2100 cm^{-1} and a doublet appears near 900 cm^{-1}. The region near 2100 cm^{-1}, associated with SiH_x stretching, is shown expanded in Figure 2.8a for unheated particles and in Figure 2.8b for particles subjected to processing at 500 °C. The principal peak in Figure 2.8a is centered near 2113 cm^{-1} with a shoulder near 2141 cm^{-1}. These peaks have been attributed to stretching vibrations of SiH_2 and SiH_3, respectively.[2.22] A less distinct contribution from the SiH stretch vibration is also present near ~2095 cm^{-1}. At higher furnace temperature settings, the contributions from SiH_3 and SiH_2 rapidly diminish until

between 400 and 500 °C the spectrum is composed of various small contributions likely attributable to different SiH configurations.[2.23,2.24] Because the particles considered here are essentially spherical, small facets of different crystalline surfaces and transition regions between those facets present opportunities for numerous SiH_x structures. Any disorganized surface content further complicates assignment of the remaining narrow SiH stretch peak to specific structural configurations.

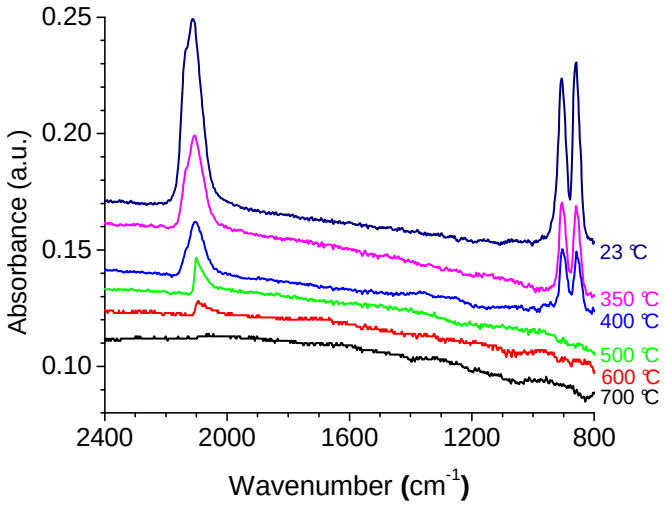

Figure 2.7. FTIR spectra of silicon nanoparticles as a function of furnace temperature setting.

The doublet near 900 cm^{-1}, shown expanded in Figure 2.9, is associated with the bend-wag deformation modes of the SiH_2 and SiH_3 species.[2.22] Upon closer inspection, two sets of doublets are present. The first set has been attributed to the SiH_2 scissors and wag deformation modes with peaks occurring at 891 cm^{-1} and 849 cm^{-1}, respectively. The second set has been assigned to the degenerate and symmetric deformation modes of SiH_3 with peaks occurring at 907 cm^{-1} and 863 cm^{-1}, respectively. Between 400 and 500

°C, contributions from the bend-wag deformation modes disappear as shown in Figure 2.7. Their absence correlates well with the disappearance of peaks in the stretch region attributed to SiH_2 and SiH_3 groups.

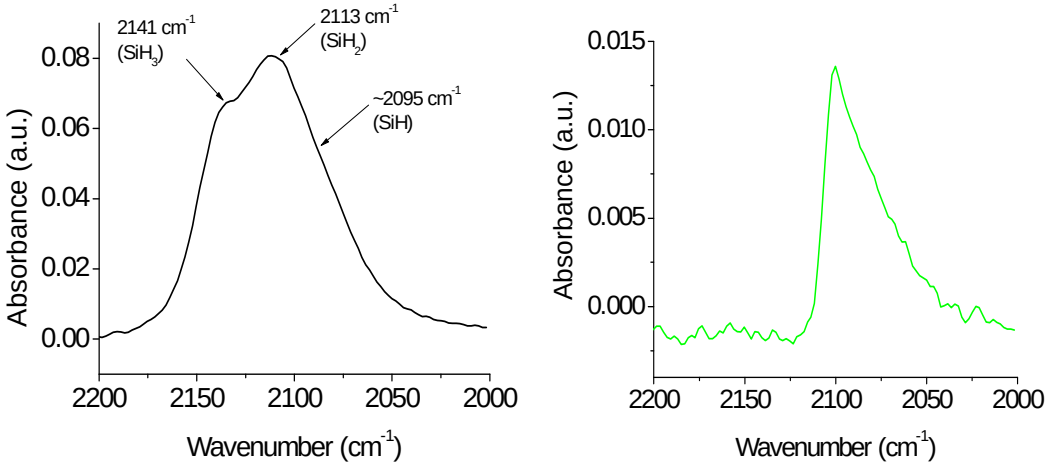

(a) (b)

Figure 2.8. Expanded views of FTIR spectra. (a) Si–H_x stretch region for unheated particles and (b) particles subjected to 500 °C. Note the much smaller signal-to-noise ratio in (b).

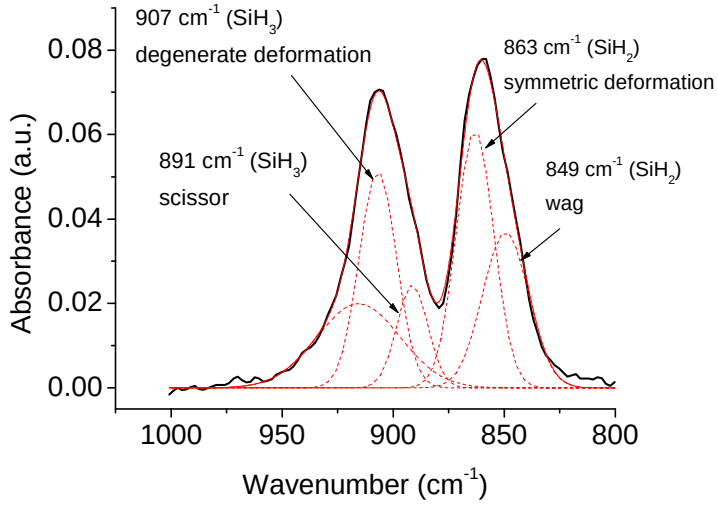

Figure 2.9. FTIR spectra in the Si–H_x deformation region for unheated particles.

ToF-SIMS results shown in Figures 2.10 and 2.11 are generally consistent with the FTIR results. In all spectra, the dominant hydrogen-related signal is due to SiH (*m/z* = 29) while contributions from SiH_2 and SiH_3 are much smaller. As the furnace setting is increased evertheless, all SiH_x peaks decrease in relation to the Si peak (*m/z* = 28), demonstrating that surface hydride concentration decreases with increasing furnace temperature. A much smaller hydrogen ion peak also exists, but the intensity does not appear to correlate with the decrease in the SiH-related peaks. Numerous small extrinsic hydrocarbon (C_xH_y) peaks and a less prominent oxide-related peak also appear in the ToF-SIMS spectra. Because the corresponding extrinsic signals do not appear in the FTIR spectra, their appearance may be attributed to ambient air exposure while the samples were transferred from the collection apparatus to the ToF-SIMS sample holder.

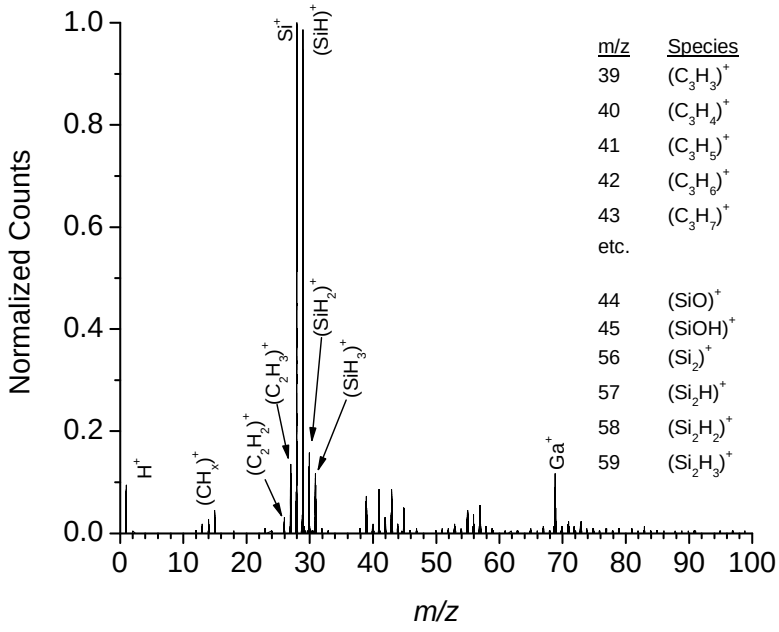

Figure 2.10. Positive ion ToF-SIMS spectra of unheated particles. All peaks are normalized with respect to *m/z* = 28.

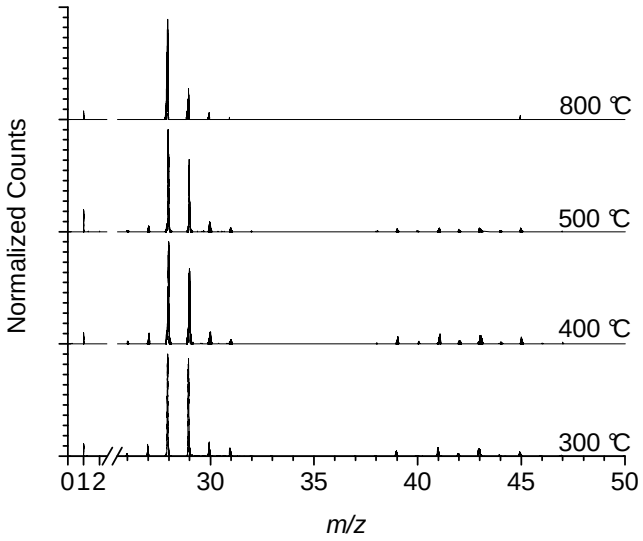

Figure 2.11. Positive ion ToF-SIMS spectra of heated particles. All peaks are normalized with respect to *m/z* = 28.

There are several possibilities for the relatively weak SiH_2 and SiH_3 features in the ToF-SIMS spectra. ToF-SIMS is inherently a destructive technique. The collision cascade caused by heavy ion impact could induce changes in the surrounding surface structure especially if highly strained bonding configurations exist in the particles. The FTIR technique as applied here does not suffer from this destructive characteristic. FTIR and ToF-SIMS spectra have also been compared side by side in a report by Benninghoven et al. regarding the repeatable production of porous silicon.[2.25] (Porous silicon exhibits complex surface structure akin to that on nanoparticles produced by the method used here: that is, surface termination with SiH_x groups in diverse orientations.[2.26]) The FITR spectra in that report also implied that SiH_2 was more prevalent than SiH or SiH_3, while in the ToF-SIMS spectra, SiH peaks were more

abundant. No reasons were suggested for the differences. In regard to the ToF-SIMS technique, the ionization potential of SiH (~7.9 eV) is less than the ionization potential of both SiH_2 (~8.9 eV) and SiH_3 (~8.7 eV).[2.27] SiH should therefore exhibit a higher ion yield than SiH_2 or SiH_3. Because of the air exposure during transfer to the ToF-SIMS apparatus and the inherently destructive nature of the technique, the FTIR results probably more closely represent the true pristine particle surface chemistry. However, the ToF-SIMS spectra still qualitatively demonstrate that the particles lose hydrogen as they are processed to higher temperatures, and that higher hydride species lose hydrogen first.

Particle mobility diameter changes correlate well with the disappearance of hydrogen-related peaks in the FTIR spectra. The majority of the particle shrinkage occurs by ~400 °C, above which point higher hydride contributions to the FTIR spectra are essentially absent. Although the complete disappearance of the SiH_2- and SiH_3-related peaks occurs at a slightly higher temperature than the initial major particle shrinkage, it should be noted that particle residence time in the tube furnace was somewhat different for the two test conditions. For the TDMA-based size measurements, the flow entering the 10-mm i.d. tube was 1 L/min at atmospheric pressure. The residence time in the furnace for the FTIR results was somewhat less since the flow entering the furnace was 410 sccm at ~20 Torr through an 11 mm i.d. tube. This residence time difference could account for the minor discrepancy between the temperature range at which the majority of the size changes occur and the complete disappearance of the higher hydride signals. A slightly larger diameter decrease occurring between 600 and 700 °C coincides with the disappearance of the SiH stretch

contribution in the FTIR spectra. Finally, a slight size increase is exhibited for the highest temperatures. This increase is likely a result of material released from the SST tube adsorbing to the particles.

Attempts were also made to readsorb hydrogen to the particle surfaces by first passing the polydisperse flow through an identical tube furnace set at 400 °C. From those thermally pre-treated aerosol distributions, particles of specific mobility diameter were selected by the first nDMA. Immediately downstream from the first nDMA, a small amount of hydrogen was introduced into the carrier gas. This mixture was then allowed to flow through the remainder of the TDMA apparatus and subsequently characterized for apparent mobility diameter changes. No lateral shifts in the distributions were observed, implying that hydrogen did not readsorb to the particles. This result is perhaps not surprising given the low dissociative sticking coefficients that have been reported for hydrogen on single-crystal silicon surfaces.[2.28]

Because the subject of light emission from silicon nanoparticles is also of broad interest, a few brief comments regarding photoluminescence behavior as a function of thermal processing are offered. Upon ultraviolet illumination, particles subjected to room temperature processing emitted visible red light. As the particles were subjected to increasing furnace temperatures, the photoluminescent behavior changed. Red light was still visible for processing temperatures up to ~500 °C, but between 400 and 500 °C the intensity dropped significantly. When particles were subjected to temperatures greater than ~600 °C, no emission was detectable by eye.

2.4 Discussion

The question naturally arises: Why do the particles shrink in the high temperature furnace? Nanoparticles could shrink due to thermal processing for various reasons. One possible reason is restructuring of amorphous content.[2.29] The spectra shown in Figure 2.7 exhibit some similarity to those from a-Si:H thin films.[2.30] On the other hand, IR spectra of highly crystalline particles[2.17] appear strikingly similar both to those presented here and to the a-Si:H films. Although the plasma particle synthesis technique is known to produce highly crystalline particles,[2.12,2.16,2.17] there could be some disorganized fraction comprising the particles, even if just an outer layer. Hofmeister et al. studied thermal annealing effects on amorphous silicon (a-Si) nanopowders using high-resolution transmission electron microscopy (HRTEM).[2.29] After annealing the particles for ~1 hour at temperatures from 300-600 °C, they found no significant structural, or surface roughness changes in the amorphous particles. Annealing for 1 hour at 700 °C produced distinct crystalline regions, and at 900 °C almost completely crystalline particles were observed. However, the authors state no considerable particle size changes, surface roughness, or increased agglomeration was observed. Since the crystallization time scales in the HRTEM experiments were much greater than the time particles examined here spent in the tube furnace, restructuring of a disorganized or amorphous outer layer is not likely to be the reason for the observed shrinkage occurring around 400 °C.

Even though no apparent size or surface roughness changes were observed by Hofmeister et al. using HRTEM, size changes observed here are near the resolution limit of most TEMs.[2.31] Mobility diameter measurements using the TDMA apparatus, on the other hand, are sensitive to changes in particle shape.[2.32,2.33] However, as shown in the

bright field images of Figure 2.12, particles processed at room temperature appear essentially the same as particles processed at 500 °C. While subtle shape factor changes leading to small mobility diameter shifts cannot be entirely ruled out, particle shape changes are not apparent in Figure 2.12, nor were they observed elsewhere during *in situ* heating experiments while being monitored by HRTEM.[2.21] Quantifying subtle particle shape changes is a formidable task and is beyond the capacity of the techniques available here.

Alternative to thermal restructuring phenomena, desorption of various surface species such as hydrogen[2.13] and/or poly-(silicon) hydrides[2.34] could be responsible for the observed size decreases. Desorption of surface volatiles could be enough to produce detectable mobility diameter changes, but it could simultaneously allow structural relaxation at the particles surface as well (*vide infra*).

Biswas and Pan examined hydrogen evolution from silicon nanocrystals in an amorphous matrix using molecular dynamics simulations.[2.13] Their report indicated two hydrogen evolution peaks: the first occurred at ~400 °C and the second between 700 and 800 °C. They attributed the low-temperature peak to hydrogen evolution from the nanocrystal surface and the high-temperature peak to dilute hydrogen evolving from the amorphous matrix. However, they did not specifically report effects due to SiH_3. Other groups[2.35] have also observed two-peak hydrogen desorption structures from amorphous silicon nanoparticles using differential scanning calorimetry, albeit the peaks were much closer than those simulated by Biswas and Pan. They attributed the lower-temperature peak (~300 °C) to hydrogen desorption from near-surface regions or surfaces of internal voids. Their explanation of the higher-temperature peak (~410 °C) was that, as a result

of restructuring after the low temperature desorption, the material became more compact; and therefore the desorption process was diffusion-controlled. The authors did not report data for temperatures above 600 °C.

For a-Si:H films grown 'on the edge of crystallinity',[2.36] two hydrogen evolution peaks were also observed: one at ~400 °C and another at ~600 °C. The authors attributed the low-temperature peak to the presence of very small Si crystals in the amorphous matrix which readily allowed H_2 to diffuse to the sample surface along the grain boundaries. The higher-temperature peak was related to hydrogen diffusion from the bulk a-Si:H film.

Desorption of various silicon hydrides could also lead to the observed particle size changes. Gates et al. used TPD and SSIMS to monitor evolution of hydrogen and silicon hydrides from the Si (100) surface.[2.34] They found a correlation between the presence of SiH_3 and silane desorption: the SiH_3 either decomposed into SiH_2 and SiH or evolved as SiH_4 at 350–375 °C. A maximum of 4% of the hydrogen desorbed as silane, thus removing about 1% of a silicon monolayer. This temperature range is consistent with the regime where most of the particle shrinkage occurs but is approximately 50 °C less than the low-temperature molecular hydrogen desorption peak from SiH_2 indicated in their results. Both the FTIR spectra in Figure 2.7 and ToF-SIMS spectra in Figures 2.10 and 2.11 indicate the presence of SiH_3 which could promote silane desorption, thus producing the observed size changes. Gates et al. also observed desorption of poly(silicon) hydrides occurring at temperatures co-incident with the low-temperature H_2 desorption peak due to SiH_2 decomposition around 425 °C. However, the quantity of desorbed poly(silicon) hydrides was significantly less than the amount of desorbed H_2. Similar desorption

phenomena could occur in the particles examined here, thus contributing to the observed size changes. Desorption of significant amounts of SiH_4 and/or Si_xH_y, however, are likely to result in particle mobility diameter decreases much larger than that observed here.

These reports suggest two desorption regimes exist, both of which correlate fairly well with the results presented here: a lower-temperature range where hydrogen most readily desorbs as H_2, and a higher-temperature range where more dilute or isolated hydrogen probably evolves. Temperature ranges of these simulations and experiments correlate fairly well with the FTIR results and may be used to explain the observed mobility diameter changes for temperatures up to ~600 °C. Perhaps the most plausible explanation of the initial shrinkage is that the diameter changes are primarily a result of molecular hydrogen desorption from SiH_2 since the shrinkage occurs at approximately the correct temperature for hydrogen desorption, and the observed changes (approximately 0.25-nm decrease in diameter) match fairly well with the Si–H bond length of ~0.15 nm.[2.37] Although there is still a small hydrogen signal present in the FTIR spectra at 600 °C, it is possible that the Si–H bonds are not oriented normal to the particle surfaces and/or could be providing a particle structure stabilizing effect. To explain the slightly larger mobility diameter decrease for temperatures greater than 600 °C, silicon nanostructure simulations are considered.

Yu et al.[2.38] used a molecular dynamics simulation to study properties of silicon nanostructures covered with different amounts of surface hydrogen. By simulating a 1000 K environment and subsequent cooling to 0 K, they found fully hydrogen-terminated surfaces enabled nanostructures to retain their original bulk crystalline

structure. Only a small lattice contraction of 0.01 to 0.02 Å was observed in the outermost 2–3 layers, and an even smaller lattice expansion was simulated for the interior of the cluster. However, for crystalline nanostructures with incomplete hydrogen termination, the trend was for the bulk tetrahedral configuration to become more distorted as more hydrogen was removed. For example, annealing a structure with ~50% surface hydrogen coverage allowed the interior tetrahedral structure to remain essentially intact. However, removing 70–80% of the surface hydrogen caused structures to develop a more compact form no longer exhibiting the preannealed crystalline structure. No overall size changes were reported. Although quantitative determination of nanoparticle hydrogen coverage from FTIR or ToF-SIMS spectra is not straightforward, Figures 2.7 and 2.11 suggest that very little hydrogen exists on the particles for temperatures above 600 °C. Therefore, based on the molecular dynamics simulations by Yu et al.,[2.38], the conclusions of which are consistent with tight-binding calculations by the same group,[2.39] restructuring to a more compact, non-crystalline form may be occurring as a result of decreasing hydrogen concentration. This could account for increased shrinkage at temperatures greater than 600–700 °C where the hydrogen content is significantly lower than at room temperature.

Experimental evidence supporting the restructuring explanation is shown in Figure 2.12 where bright spots in the dark field images are suggestive of crystalline material. As shown in the images, the number of bright spots is much greater for particles processed at room temperature than for particles processed at 500°C. This implies particle crystallinity is decreasing as a result of elevated temperature processing. According to the FTIR results, particles processed at 500 °C contain very little hydrogen.

Based on the results presented by Yu et al.,[2.37] therefore, restructuring to more compact forms could be occurring. Loss of crystallinity could also partially explain the photoluminescent behavior changes associated with increased processing temperature.

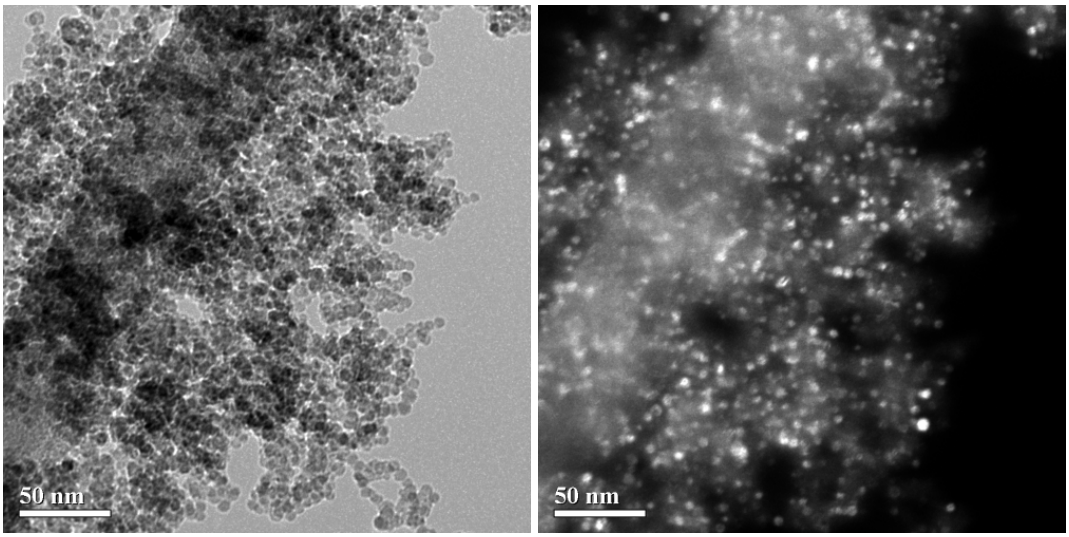

(a)

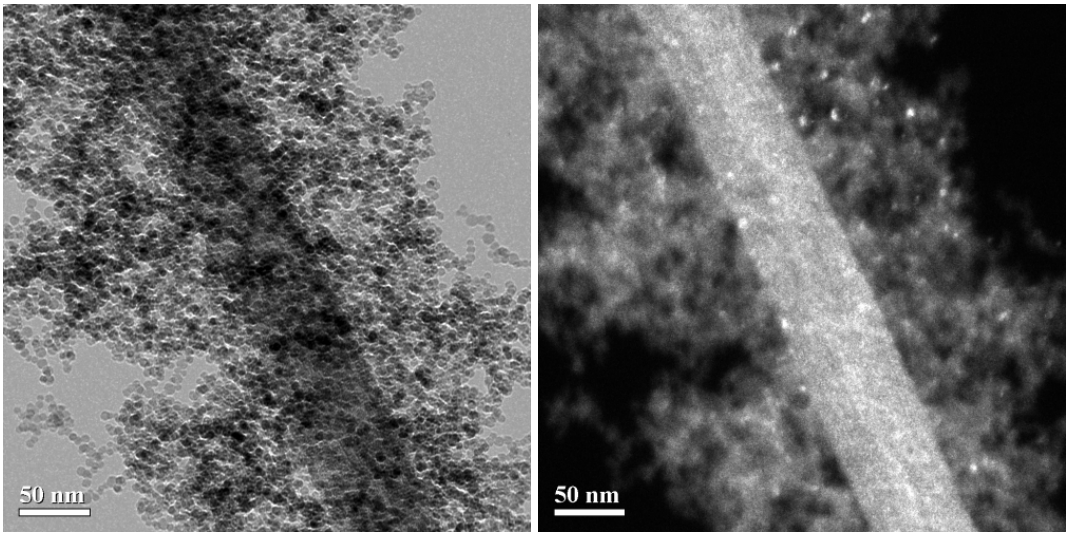

(b)

Figure 2.12. Bright field (left) and the corresponding dark field (right) TEM images of size-polydisperse particles collected electrostatically from the aerosol stream immediately downstream from the tube furnace at ~20 Torr. (a) Particles processed at room temperature. (b) Particles processed at 500 °C.

2.5 Conclusion

The surface chemistry of pristine silicon nanoparticles has been evaluated without ambient air exposure. Effects of thermal processing on the chemistry of hydrogen-terminated nanoparticles produced in a non-thermal RF plasma were evaluated with FTIR, ToF-SIMS, and a TDMA apparatus. FTIR spectra indicated that pristine particle surfaces were primarily covered by SiH_2 groups with lesser amounts of SiH and SiH_3, while ToF-SIMS spectra indicated slightly different surface composition. FTIR results showed that SiH_2- and SiH_3-related signals largely disappeared at temperatures lower than that of SiH. Regardless of the differences, both techniques demonstrated that the surface hydrogen coverage decreased as the processing temperature increased. Heating the particles also produced modest reductions in mobility diameter which correlated well with the disappearance of hydrogen signals in the FTIR and ToF-SIMS spectra. Both the surface chemistry and mobility diameter changes reported here are important considerations for techniques used to impart passivation or functionalization layers to the particles if the as-produced particle properties are to be retained.

Chapter 3.

Thermal Oxidation of 6 nm Aerosolized Silicon Nanoparticles: Size and Surface Chemistry Changes

The earliest stages of thermal oxidation of 6 nm diameter silicon nanoparticles by molecular oxygen are examined using a tandem differential mobility analysis (TDMA) apparatus, Fourier-transform infrared (FTIR) spectroscopy, time-of-flight secondary ion mass spectroscopy (ToF-SIMS), and X-ray photoelectron spectroscopy (XPS). Particles are synthesized in and then extracted from a non-thermal RF plasma operating at ~ 20 Torr into the atmospheric pressure TDMA apparatus. The TDMA apparatus was used to measure oxidation-induced size changes over a broad range of temperature settings and N_2–O_2 carrier gas mixtures. Surface chemistry changes are evaluated *in situ* with an FTIR spectrometer and a hybrid flow-through cell, and *ex situ* with ToF-SIMS and XPS. Particle size measurements show that at temperatures less than ~500 °C, particles shrink regardless of the carrier gas oxygen concentration, while FTIR and ToF-SIMS spectra demonstrate a loss of hydrogen from the particles and minimal oxide formation. At higher temperatures, FTIR and XPS spectra indicate that an oxide forms which tends towards, but does not fully reach, stoichiometric SiO_2 with increasing temperature. Between 500 and 800 °C, size measurements show a small increase in particle diameter with increasing carrier gas oxygen content and temperature. Above 800 °C, particle growth rapidly reaches a plateau while FTIR and XPS spectra change little. ToF-SIMS signals associated with O–Si species also show an increase in intensity at 800 °C.

3.1 Introduction

Oxidation at extended silicon surfaces has been extensively studied and modeled.[3.1,3.2] Much of the research has focused on understanding Si and SiO_2 for use in electronic device applications. More recently, silicon nanoparticles are also being examined for use in electronic devices,[3.3] visible light emission applications,[3.4-3.6] and improving photovoltaic conversion in solar cells.[3.7] Although silicon nanoparticles have been synthesized by numerous methods, some of those methods do not lend themselves well to producing narrow size distributions, while other methods produce particles too large for the quantum confinement characteristics that are believed to be a prerequisite for visible light emission. Regardless of the production method, further processing is often required to elicit the desired particle properties.[3.4,3.5,3.8]

In general, silicon nanoparticles are highly susceptible to oxidation. Despite the significant amount of research already directed towards understanding oxide formation on extended surfaces, numerous groups are directing significant effort towards understanding the role of the oxide layer on properties unique to silicon nanostructures.[3.5,3.9,3.10] For example, as an oxide shell grows on a silicon particle, the silicon core may be either partially or wholly consumed depending on the processing conditions. This phenomenon has been proposed as one method to obtain the desired particle core dimensions required for visible light emission.[3.11] On the other hand, efforts are also being directed towards passivating particles against oxidation.[3.12]

A non-thermal RF plasma is employed in this chapter to continuously produce discrete, relatively monodisperse, silicon nanoparticles via gas-to-particle conversion.[3.13] This method naturally lends itself to both tailoring and interrogating the particles using

gas/aerosol-phase techniques. For example, rather than depositing particles on or growing them within a substrate, thermally oxidizing them, and then attempting to reclassify the particle size distribution using microscopy or other techniques, particles can be produced in the RF plasma, and thermally oxidized as they flow through a tube reactor. Size changes due to oxide formation can be quantified online using differential mobility analysis, a well known technique for aerosol characterization.[3.14] By processing discrete aerosolized particles, particle–substrate and particle–particle effects that could alter oxide growth are avoided. Furthermore, aerosol-based analysis makes it possible to study oxide growth on free particles rather than on particles embedded within an SiO_2 substrate or encapsulated in a native SiO_x shell, as was done previously.

Nanoparticle residence times in an aerosol flow tube reactor can be very short because of gas expansion effects as processing temperatures are increased. This places some restrictions on the time over which reactions such as thermal oxidation are allowed to occur in an aerosol flow tube reactor. However, short residence times are also beneficial in a fundamental sense in that they allow one to probe changes in particle surface chemistry and oxide growth at the earliest stages of thermal oxidation and thus collect experimental data under conditions to which the vast majority of published reports can only extrapolate.

This chapter describes the growth and surface chemistry changes of 6 nm diameter silicon nanoparticles that are thermally oxidized by molecular oxygen in an aerosol flow tube reactor. Particles are swept through the flow tube reactor in carrier gases comprised of different N_2–O_2 mixtures at a number of different temperature settings, and particle size changes due to thermal processing are quantified on-line using

a tandem differential mobility analysis (TDMA)[3.15] apparatus. In TDMA, particles of a specific size are selected by a first differential mobility analyzer (DMA) according to their electrical mobility. Those selected particles are physically or chemically processed, for example in a flow tube reactor, and then passed through a second DMA and into a particle counter. By appropriately incrementing the voltage applied to the second DMA and measuring the particle number concentration at each voltage increment, changes in particle size due to different processing conditions within the flow tube reactor can be quantified. Those particle size changes can then be related to fundamental processes such as oxide growth kinetics.

Aerosol particles may exhibit different geometric morphologies. Therefore, the concept of an equivalent particle diameter is often invoked when employing aerosol differential mobility analysis techniques. The equivalent diameter relevant to the results presented here is the electrical mobility diameter, or the diameter of a sphere with the same electrical mobility behavior as an irregularly shaped particle.[3.16] The particles examined in this chapter are essentially spherical and small enough such that the probability of multiply charged particles is negligible. Therefore, the electrical mobility diameter can be related to the physical diameter in a straightforward manner and taken as a surrogate for the geometric particle diameter.[3.17] Particle surface chemistry changes are characterized using Fourier transform infrared spectroscopy (FTIR), time of flight secondary ion mass spectroscopy (ToF-SIMS), and X-ray photoelectron spectroscopy (XPS). In conjunction with the FTIR measurements, we also describe a hybrid flow-through gas cell developed in our laboratory. This device allows particles to be collected for *in situ* particle surface chemistry characterization, and also provides a convenient

means by which particles can be collected for further interrogation or integration into other processing schemes.

3.2 Experimental

The experimental system consisted of four primary components: a particle source, a reaction zone, a method of measuring particle size changes while the particles are flowing in a carrier gas, and various spectroscopic instruments to evaluate particle surface composition. The particle source was a low pressure, non-thermal RF plasma.[3.13] Silane highly diluted in argon (0.5% SiH_4 in Ar from BOC Edwards) was further diluted with argon (Praxair, St. Paul, MN) before being introduced into a quartz tube plasma reactor. Gas flows were 5-10 sccm of the SiH_4/Ar mixture and 400 sccm of argon. RF power at 13.56 MHz was coupled to a 10 mm i.d. quartz tube reactor through a matching network and two copper ring electrodes as shown schematically in Figure 3.1. The RF amplifier was an Electronics & Innovation Model A150 (Rochester, NY) and the signal generator was a Tektronics AFG3021. Power output indicated by the matching network was ~30 W.

Silicon nanoparticles were formed in the plasma reactor at pressures of ~18–20 Torr. For particle size selection and classification, the plasma pressure was obtained using a gas-operated venturi pump (Model UV143H, Air-Vac, Seymour, CT). Gas vent lines from liquid nitrogen cylinders (Praxair, St. Paul, MN) provided the high volumetric flow rate gas needed to obtain the pressure for sustaining the plasma glow discharge in the quartz tube reactor. As particles flowed from the plasma through the pump, they became entrained into the high volumetric flow rate N_2. The particles were rapidly

diluted, thus lowering the particle number concentration and minimizing agglomeration during the transition from sub-atmospheric to atmospheric pressure.

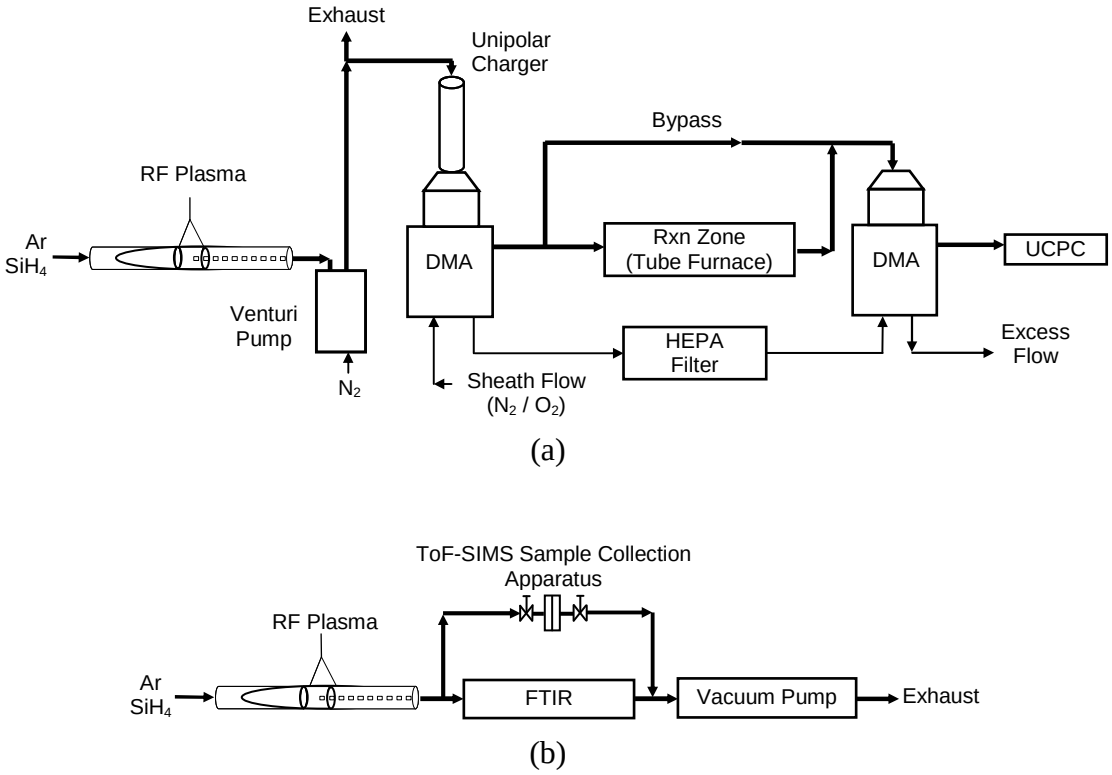

Figure 3.1. Schematic of experimental setup used to measure (a) particle diameter changes, and (b) compositional changes. A hybrid flow-through gas cell as described in the text was used in conjunction with FTIR spectrometer. Particles flow along the bold lines.

Particle size changes were classified as follows. Aerosol flow was sampled from the atmospheric-pressure venturi pump exhaust at a rate of 1 lpm though a 6.4 mm i.d. tube mounted normal to the exhaust flow direction. Although not strictly isokinetic sampling, extracting aerosolized particles in this manner allowed a sufficient number of 6

nm diameter particles to be obtained for subsequent thermal processing and further quantification of the accompanying particle size changes. The sampled aerosol was directed through a unipolar diffusion charger similar to one developed by Chen and Pui,[3.18] where the particles acquired at most a single charge, and subsequently into the first differential mobility analyzer (DMA) (Model 3085, TSI, Inc., Shoreview, MN). A constant voltage was applied to the first DMA to select positively charged 6 nm particles. Selected particles were either passed through a single zone tube furnace (Lindberg/Blue Model HTF 55122A, Asheville, NC) where thermal oxidation occurred, or a through an equivalent-length bypass line. Tubes used in the furnace were either 10 mm i.d. quartz or 10.9 mm i.d. Inconel 600, and temperature settings ranged from room temperature to 1100 °C. The temperature profile within the tube furnace was previously evaluated in detail and was well-represented by a fourth-order polynomial.[3.19] Radiative heating was minimal,[3.20] and particles were assumed to be in thermal equilibrium with the surrounding gas as they flowed through the furnace.[3.14]

Particles flowed from either the bypass or the tube furnace into the second DMA where the applied voltage was stepped in small increments. At each voltage increment, particle number concentrations were measured with an ultrafine condensation particle counter (UCPC) (Model 3025A, TSI, Inc.). Those number concentration measurements were assembled into number concentration distributions as a function of the voltage applied to the DMA, and used to determine the most probable particle diameter for each set of experimental conditions. Number concentration versus voltage distributions were measured a minimum of three times and averaged for each set of experimental conditions. A normal Gaussian curve was fit to each averaged distribution using the

Levenberg–Marquardt algorithm, and the center of each fitted curve was denoted as the most probable selected particle diameter for a given set of experimental conditions. The TDMA apparatus in series with the plasma reactor is shown schematically in Figure 3.1a. Dry oxygen (industrial grade, 99.5% pure, Praxair, St. Paul, MN) was introduced into the system via the sheath flow of the first DMA. Calibrated rotameters were used to vary the sheath flow composition from nearly 100% nitrogen to approximately 90% oxygen / 10% nitrogen, and DMA flows were kept at 10 lpm sheath gas, 1 lpm aerosol.

Particle composition was evaluated *in situ* by Fourier-transform infrared (FTIR) spectroscopy. For these measurements, flow from the plasma reactor was introduced into the tube furnace and then directly into a hybrid gas cell (*vide infra*) without size selection (Figure 3.1b). Oxygen was introduced immediately upstream of the furnace at a rate of 10 sccm, resulting in a carrier gas oxygen content of ~2.5% by volume. The furnace tube was Inconel 600, and temperature settings ranged from room temperature to 950 °C. A Model 1400 Welch vacuum pump was used rather than the venturi pump for these measurements. Spectra were recorded in the transmission mode using a Magna-IR Spectrometer Model 550 (Nicolet Instrument Corp., Madison, WI) and the hybrid flow-through gas cell that consisted of a short length of tube capped on both ends by IR-transmitting windows.[3.21] Two ports on opposite ends of the gas cell were used to flow aerosol continuously through the hybrid cell. In this configuration, the IR spectrometer readily detected 0.5% silane in argon over a 10 cm path length when the plasma was not on. When the plasma was on, however, the particle concentration was not high enough to collect a meaningful spectrum over the same path length. Therefore, a small piece of fine wire mesh was mounted within the cell. As the aerosol flowed through the hybrid gas

cell, the mesh collected a sufficient number of particles for IR analysis. Particles were collected for 20 minutes after which final spectra were recorded at 2 cm^{-1} resolution and averaged over 32 scans. Spectra were also recorded during the 20 minute collection period to determine if the particles already captured within the gas cell continued to oxidize as the carrier gas flowed across them.

For ToF-SIMS (Charles Evans and Associates, Redwood City, CA) analysis, samples were collected in a manner similar to the FTIR sample collection method and sealed in their as-collected environment by two valves before and during transport to the instrument to minimize adventitious reactions with ambient air. The analysis chamber pressure was approximately 5×10^{-9} Torr, the incident ion beam was gallium, and the extraction voltage was 15 kV. Both positive and negative ion spectra were recorded.

XPS analysis was carried out in a Surface Science Instruments SSX-100 system using monochromated Al K_α-rays. Base pressure was less than 10^{-8} Torr. Survey and high-resolution spectra were recorded at 150 and 50 eV pass energies, respectively. Sample charging offsets were referenced to the C 1*s* peak. Particles were collected for XPS analysis in the same manner as those collected for ToF-SIMS analysis.

3.3 Results

Typical particle number concentration versus voltage curves measured with the TDMA apparatus are shown in Figure 3.2. The abscissa represents the voltage applied to the DMA, and the ordinate represents the number of particles per cubic centimeter measured with the UCPC. As shown in the figure, the overall polydisperse number concentration distribution is non-symmetric with a maximum near 200 volts which

corresponds to a most probable particle diameter of 10 nm. Also shown in Figure 3.2 is a typical distribution selected by the first DMA and subsequently sent through the bypass. The distribution is symmetric about the mode and represents ~6 nm diameter particles.

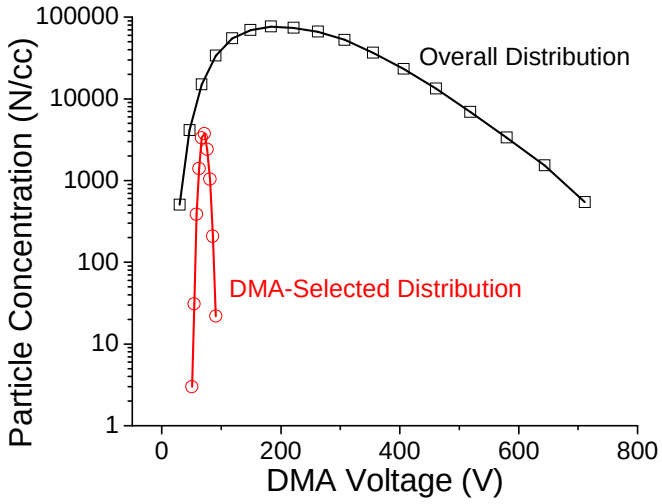

Figure 3.2. Particle number concentration distributions as a function of applied DMA voltage. Overall distribution refers to the flow extracted from the venturi pump exhaust quantified with a single DMA and the UCPC. DMA-selected distribution refers to 6 nm particles selected by the first DMA and quantified by the second DMA and the UCPC.

Figure 3.3 shows several number concentration distributions for particles oxidized at different temperatures in carrier gas containing ~38% O_2 and 62% N_2. A typical set of three distributions that were averaged to determine representative particle diameters is shown in Figure 3.3a. Figure 3.3b shows averaged particle number concentration distributions corresponding to several furnace settings. Each curve represents the average of at least three successively measured distributions. Two features are apparent in the

figure. First, particle number concentrations decreased as the furnace temperature setting was increased. When the furnace was shut off, distributions of particles passed through the furnace were essentially the same as those passed through an equivalent-length bypass line. Therefore, the decrease in particle number concentration can be primarily attributed to thermophoretic losses because of the temperature gradient at the furnace exit. Particles were also lost due to electrostatic charging of the quartz tube. Quartz tubes used at the highest furnace temperature settings for extended periods tended to stop transmitting particles. This was the primary reason for using the Inconel 600 tube. The second feature apparent in the figure is that the distribution peaks shift first to lower and then to higher voltages with increasing furnace setting, indicating both diameter reduction and growth, respectively.

Particle size measurements are summarized in Figure 3.4. Figure 3.4a shows particle diameter as a function of carrier gas oxygen content at different temperature settings. At a temperature setting of ~500 °C particles exhibit a small shrinkage regardless of the carrier gas oxygen concentration. Between 600 and 700 °C particles exhibit a small amount of growth, but generally only at the highest carrier gas oxygen concentrations. At a temperature setting of 800 °C, particles begin to exhibit more extensive growth over all carrier gas compositions, and a growth plateau begins to emerge. By 900°C, the growth plateau is well developed.

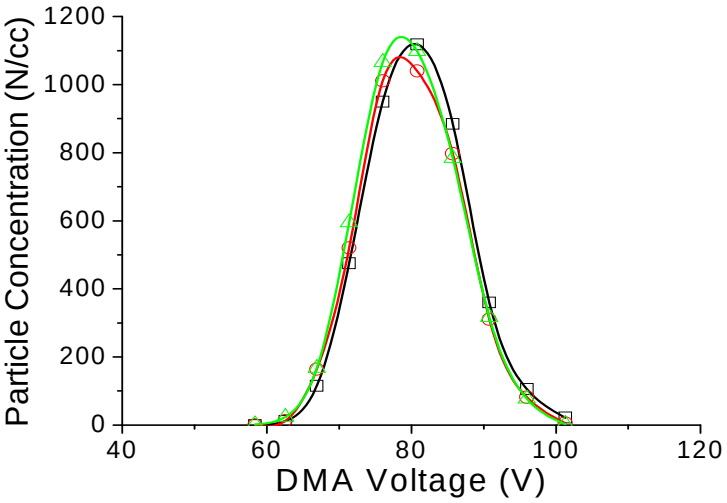

(a)

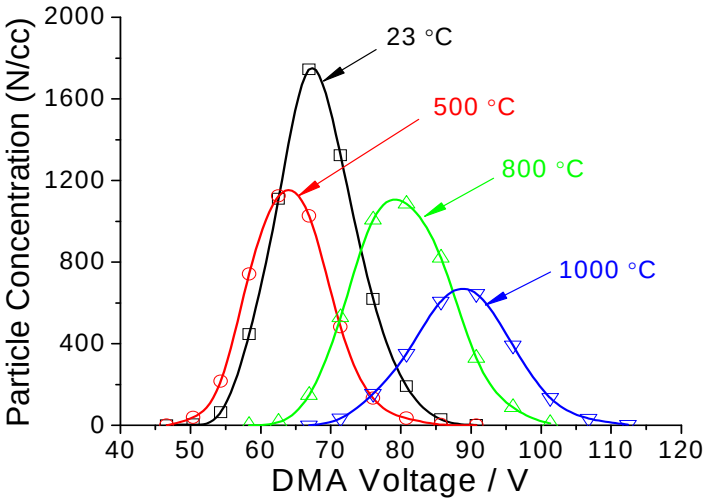

(b)

Figure 3.3. Various particle number concentration distributions from 38% oxygen content carrier gas conditions. (a) A typical set of 3 consecutive scans that were averaged for each set of processing conditions. The furnace temperature setting was 800 °C for this particular set of three scans. (b) Distributions for several furnace temperature settings.

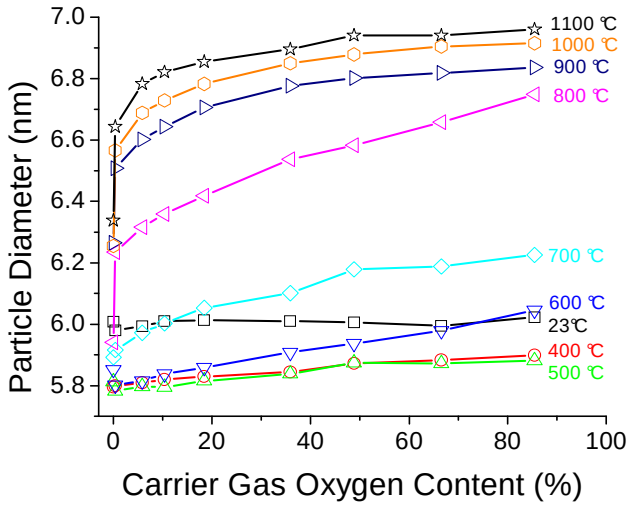

(a)

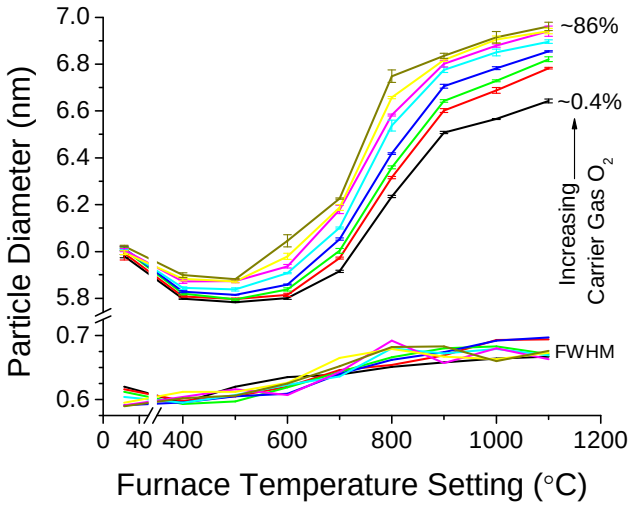

(b)

Figure 3.4. Particle diameter (a) as a function of carrier gas oxygen content at different temperature settings, and (b) as a function of furnace temperature setting at different carrier gas oxygen contents. Error bars represent the standard deviation of averaged distribution peaks. Also shown is the FWHM trend of the averaged distributions.

When particles are heated in the furnace at a temperature that causes growth, very little oxygen is required to bring about most of the size change. For example, the smallest carrier gas oxygen content considered here (0.4%) was enough to yield ~10% particle diameter growth at 1100 °C, while the largest growth, ~15% increase in diameter, occurred at 1100 °C in the highest carrier gas oxygen concentration.

Figure 3.4b shows the same data presented such that the initial particle shrinkage is more apparent. Successively measured distributions for each individual set of processing conditions are nearly coincident as indicated by the error bars in Figure 3.4b. Particle distribution dispersities at each set of processing conditions, as quantified by the distribution full width at half maximum (FWHM), are also shown. Distributions exhibit a slight increase in width as the temperature setting is increased but remain relatively constant as the carrier gas oxygen content is varied at each temperature setting.

FTIR results are summarized in Figure 3.5. Figure 3.5a shows spectra recorded with no oxygen added to the carrier gas. Pristine particles are unoxidized and terminated by SiH_x groups (x = 1, 2, 3) at room temperature. A band at 2113 cm^{-1} that is associated with Si–H stretching in SiH_2 is most intense, followed by bands attributed to SiH_3 (2140 cm^{-1}) and SiH (2095 cm^{-1}).[3.22] The doublet between 850 and 900 cm^{-1} represents deformation modes of SiH_2 and SiH_3 and is only present for particles processed at furnace settings below ~400 °C. Above 500 °C, the doublet is absent, and the only remaining signals may be attributed to modes associated with Si–H. By 700 °C, hydrogen-related peaks are absent indicating that essentially all hydrogen-containing species have desorbed from the particles.

Figure 3.5b shows FTIR spectra of fresh particles processed at different temperature settings and 2.5% carrier gas oxygen content. Spectra were also recorded at 10% carrier gas oxygen conditions to determine whether differences in oxygen fraction could produce changes in oxide composition. The spectra were essentially identical for the two carrier gas conditions.

FTIR spectra were also periodically recorded as the particles accumulated on the mesh to evaluate whether or not the particles continued to oxidize on the mesh during the collection process. No new peaks or shifting peak shifts occurred over the collection duration suggesting that oxidation did not continue to occur as the carrier gas flowed over the particle-laden mesh. The only difference between periodically collected spectra for a given sample was an increase in IR peak intensity because of longer collection times.

For furnace settings up to 400 °C the IR spectra in Figure 3.5b are similar to those with no oxygen intentionally introduced into the system. The primary differences are the small shoulders near 800, 960, and 1050 cm^{-1} on either side of the SiH_x deformation doublet, all of which indicate the onset of oxide formation. At 400 °C the spectra also exhibit an overall decrease in signal intensity compared to the room-temperature spectrum, and the SiH_3 stretch peak is attenuated relative to the SiH and SiH_2 peaks. By 500 °C, the doublet between 850-900 cm^{-1} exhibited by the fresh particles is no longer present, and stronger indications of oxidation appear: a broad absorbance with maximum intensity near 1020 cm^{-1}, several small distinct peaks at 980, 2168, 2261 cm^{-1}, and a few small features near 800 cm^{-1}.

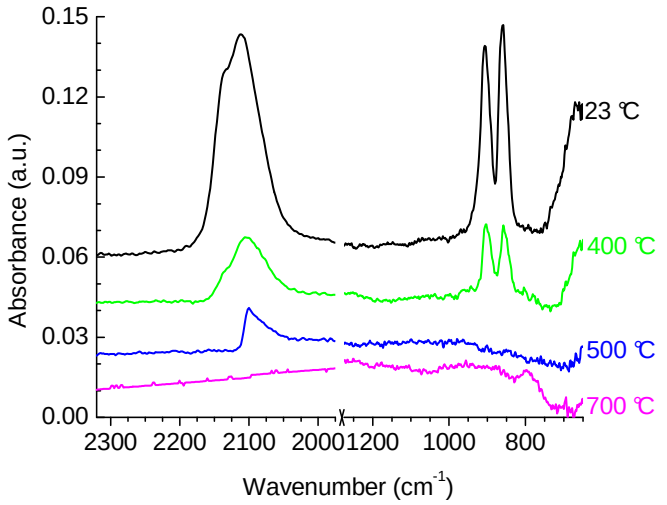

(a)

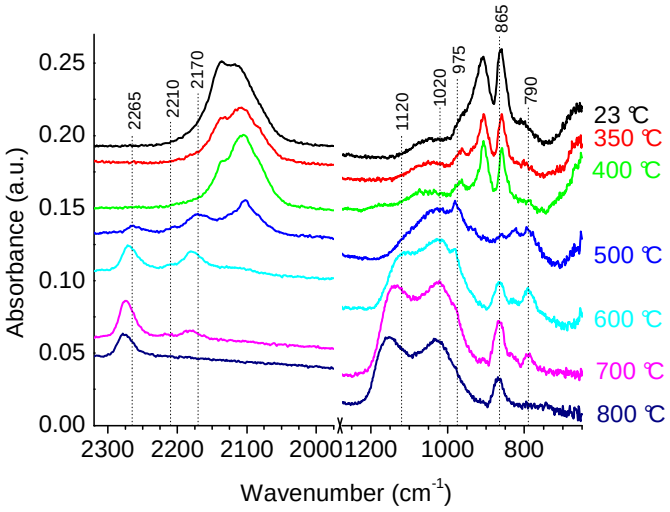

(b)

Figure 3.5. FTIR spectra as a function of temperature with (a) no oxygen introduced into the carrier gas and (b) with 10 sccm O_2 added to the carrier gas.

By 600 °C, the intensity of the peak near 1020 cm^{-1} increases and shifts to ~1026 cm^{-1}. Distinct peaks emerge near 865 and 1127 cm^{-1}, and the peak at 790 cm^{-1} becomes more pronounced. Peaks in the Si–H stretch region also exhibit changes. The original

room-temperature SiH_x stretch modes are essentially absent, and the other two peaks at 2166 and 2260 cm^{-1} grow in area and shift to slightly higher wavenumbers. Peaks near 790 and 2180 cm^{-1} are distinctly visible only from ~500-700 °C and exhibit maximum intensities around 600 °C.

In general, as the furnace temperature setting is increased oxide-related peaks shift to higher wavenumbers. Although not shown, spectra acquired at 900 and 950 °C follow the same trend but the peak shifts are much less pronounced. Furthermore, the overall shapes and relative peak intensities do not change significantly at temperatures higher than 800 °C, and no additional absorptions appear or disappear. Bands that are characteristic of SiOH (~3650 cm^{-1}) are not present in the spectra.

Positive ion ToF-SIMS spectra shown in Figure 3.6 are dominated by the Si peak (*m/z* = 28) with much smaller contributions from SiH, SiH_2 and SiH_3. Other peaks associated with hydrocarbons are also present but to a much lesser extent. Because no hydrocarbon signatures appear in the FTIR spectra, the hydrocarbon-related peaks are attributed to ambient air exposure during sample transfer into the ToF-SIMS instrument. As the furnace temperature setting is increased, SiH_x peaks show a decrease in intensity while the peak associated with OSiH (*m/z* = 45) shows a small increase in intensity.

Negative ion ToF-SIMS spectra shown in Figure 3.6 are dominated by H (*m/z* = 1) and O (*m/z* = 16), with lesser amounts of OH, and several small hydrocarbon related peaks. Si, SiH_x, and OSiH were also detected but at a lesser intensity than those shown in the positive ion spectra. The intensity of both the O and OH peaks increase with increasing furnace temperature setting while the hydrogen peak retains a strong presence over all the furnace temperature settings. At 800 °C, oxygen uptake by the particles is

more evident as indicated by the peaks due to O_2Si (*m/z* = 61), O_2SiH (*m/z* = 62), O_3Si (*m/z* = 76), and O_3SiH (*m/z* = 77).

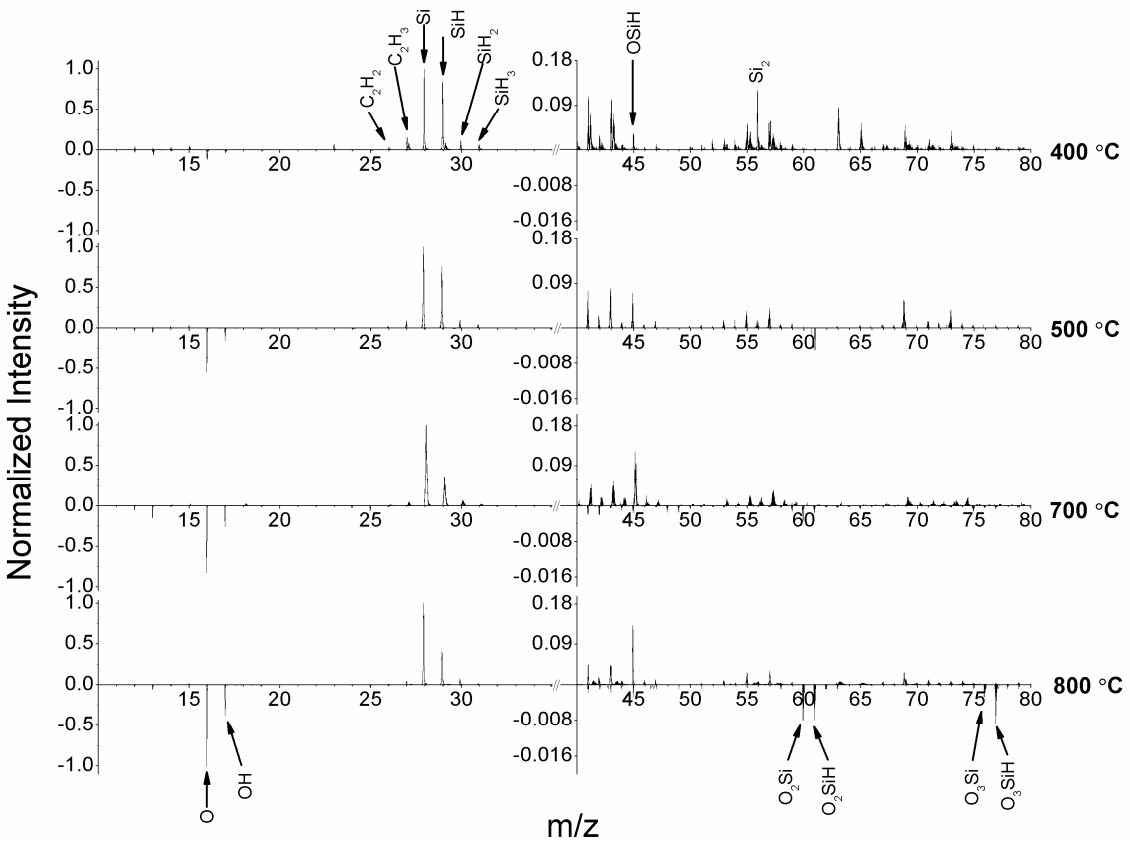

Figure 3.6. Positive and negative ion ToF-SIMS spectra showing silicon and oxygen-related peaks at several processing temperatures. Positive and negative spectra are normalized with respect to *m/z* = 28 and *m/z* = 1, respectively. Note that the axes are scaled differently for both positive and negative ions at *m/z* ≥ 40.

High resolution XPS spectra of the Si 2*p* region are shown in Figure 3.7 for several oxidation processing temperatures. The evolution of the shoulder on the high binding energy side of the bulk Si 2p peak (~99 eV) established the following. First, as

shown by the gradual shift of the shoulder to higher binding energies with increasing temperature, the particles processed at higher temperatures exhibit more highly oxidized states than those processed at lower temperatures. The oxide formed also consists of different sub-stoichiometric components based on the broad features and the lack of a peak at the binding energy normally associated with SiO_2. Second, the spectra do not exhibit significant changes above an oxidation processing temperature of 800 °C, which is in good agreement with the IR results. Third, the persistence of the bulk Si peak at all examined processing temperatures demonstrates that the particles do not fully oxidize, and therefore that a silicon core remains.

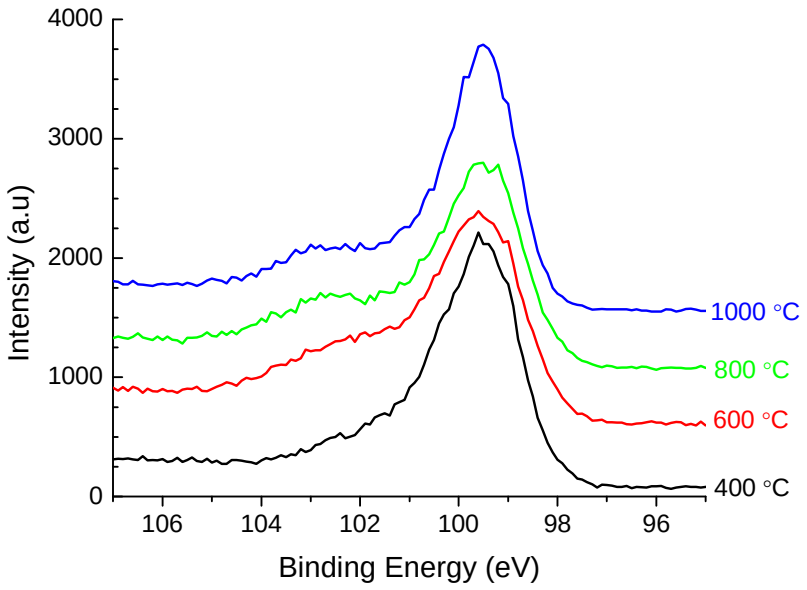

Figure 3.7. High resolution XPS spectra of the Si 2*p* region for particles oxidized at several temperature settings.

3.4 Discussion

Figures 3.2 and 3.3 demonstrate that the TDMA apparatus is capable of selecting a specific narrow size distribution of particles from a much broader overall distribution and quantifying small size changes due to thermal processing. Figure 3.4 indicates that particles exhibit a decrease in diameter at processing temperatures between ~400-500 °C. This temperature range is consistent with hydrogen desorption from other silicon surfaces,[3.23] including silicon nanoparticles.[3.21] At similar temperatures, FTIR spectra in Figure 3.5a indicate that the higher hydrides (SiH_2 and SiH_3) disappear, while smaller signals attributable to modes associated with SiH remain. Positive-ion ToF-SIMS spectra also show that the intensities of SiH_x-related peaks decrease with increasing temperature setting. Therefore, the observed particle shrinkage is likely related to desorption of hydrogen or hydrogen-related species.

Because of hydrogen desorption particles become more susceptible to oxidation as demonstrated by the FTIR spectra shown in Figure 3.5b. Both the FTIR and ToF-SIMS spectra in Figure 3.6 both indicate that peaks commonly related to oxide formation do not exhibit a strong presence below 500 °C, a temperature at which hydrogen still exists on the particles. Thus, oxidation is hindered by the hydrogen. Size measurements in Figure 3.4b show that the particles do not exhibit growth at temperature settings below ~500 °C regardless of the carrier gas oxygen concentration, and further substantiate that oxidation is hindered by the hydrogen.

When particles do grow, the large variation in carrier gas oxygen content has a smaller effect than the temperature setting variation as shown in Figure 3.4b. For example, increasing the oxygen concentration from ~5% to 50% at given temperature

setting does not lead to significant differences in particle growth. However, holding the carrier gas oxygen content at a constant value and increasing the furnace temperature setting from 700 °C to 1000 °C leads to significant particle diameter growth, with a notable increase occurring near 800 °C. In another report,[3.24] differential scanning calorimetry and thermo-gravimetric analysis were used to examine the oxidation process of hydrogen-terminated, amorphous Si nanoparticles. There, oxidation was also preceded by dehydrogenation, and oxygen partial pressure had little effect on oxygen uptake. Measurements observed in this report are consistent with the concept of surface hydrogen passivating particles against oxidation and the lesser effect of carrier gas O_2 content on oxygen uptake.

The IR region from ~650 to 1300 cm^{-1} is commonly associated with various structures comprised of silicon, oxygen, and hydrogen, and their respective stretching and/or deformation modes.[3.2,3.25-3.27] Because the particles examined here are essentially spherical[3.21] and the IR beam is unpolarized, all IR-active modes are able to be simultaneously detected and recorded over the range of the IR detector (650–4000 cm^{-1}). This complicates peak assignments, but distinct trends in the spectra are still apparent.

According to Pai et al.,[3.25] oxide stoichiometry may be estimated by considering the asymmetric Si–O–Si stretching mode ranging from ~950 to 1075 cm^{-1}. In that report, the value of x in SiO_x varied almost linearly with wavenumber: $SiO_{0.5}$ and SiO_2 were associated with peaks at ~975 and ~1075 cm^{-1}, respectively. As shown in Figure 3.5b, the peaks in this region also vary with furnace temperature setting. On the basis of the interpretation by Pai et al., the broad peak near 1016 cm^{-1} and 500 °C roughly correlates with SiO. While at 800 °C, the Si–O–Si peak appears at ~1035 cm^{-1}, roughly correlating

with $SiO_{1.5}$. Peaks shift to slightly higher wavenumbers for particles processed at higher tempetratures, but still do not reach values representative of SiO_2. Although an oxide layer forms, it is probably not stoichiometric SiO_2 according to these results.

Both the asymmetric Si–O–Si stretching signature used to estimate oxide stoichiometry by Pai et al.,[3.25] and the broad shoulder on the higher wavenumber side of that peak have also been examined in conjunction with the transition region between Si and SiO_2. Moreover, the evolution of these two peaks has also been correlated with the earliest stages of oxide formation. For example, Weldon et al.[3.28] studied the initial oxidation stages of silicon by H_2O and suggested that peaks at 975 and 1125 cm^{-1} could be precursors to the transverse optical/longitudinal optical (TO/LO) mode pair commonly observed on extended surfaces. In a subsequent report regarding HF-thinned thermal oxides, two broad peaks at 975 and 1125 cm^{-1} were reported to be the respective signatures of the TO and LO modes of thinned oxides.[3.29] Essentially, as the oxide was chemically thinned the LO- and TO-related peaks shifted from higher wavenumbers to lower wavenumbers with the LO peak shifting more than the TO peak. The thinnest oxides reported there were ~0.6 nm. The TDMA apparatus used here is not able to determine oxide thickness. But because the silicon particle core is ”consumed” as an oxide shell grows, and the maximum increase in particle diameter was less than 1 nm, the oxide thickness is probably somewhat greater than 0.5 nm. These IR observations correlate fairly well with the particle size measurements shown in Figure 3.4.

Lambers and Hess[3.28] also employed IR to examine the early stages of silicon oxide formation using pulsed laser photoinduced oxidation of hydrogen terminated Si. Their spectra recorded in oblique incidence appear strikingly similar to the ones shown in

Figure 3.5b, particularly at furnace settings between 500 and 700 °C. As shown in Figure 3.5b, the small shoulder near ~960 cm^{-1} in the 23 °C spectrum shifts to ~975 cm^{-1} at 500 °C; the broader shoulder at 1020 cm^{-1} also becomes more fully developed. With increasing temperature setting, the peak at 975 cm^{-1} does not shift in the spectra presented here or in that reported by Lambers and Hess, but the broader shoulder increases in area and shifts to higher wavenumbers more commonly associated with the substoichiometric TO mode. These reports substantiate the idea that the oxide layer formed on the particles is SiO_x ($x < 2$) rather than SiO_2. Moreover, particle size measurements are consistent with other reports indicating a substoichiometric transition region between Si and SiO_2 generally less than a few nanometers thick.[3.30]

FTIR absorption peaks at ~2175 and ~2270 cm^{-1} have been associated with two and three oxygen atoms back-bonded to surface silicon as O_2SiH_2 and O_3SiH, respectively.[3.31] The peak near 865 cm^{-1} has also been associated with the deformation mode of O_3SiH.[3.26,3.32] In accord with these observations is the evolution of peaks at 865 and 2270 cm^{-1} in Figure 3.5b at temperature settings greater than 500 °C. The evolution of the peaks near 790 cm^{-1} at temperature settings between 500 and 700 °C also follows that of the peaks near 2175 cm^{-1}. Therefore, these two absorbances are likely due to related structures and are tentatively associated with O_2SiH_2.

As shown in Figure 3.4, the particles appear to reach a growth plateau after an initial rapid growth. This plateau could be due to several effects. First, as the furnace temperature setting is increased, particle residence time within the tube furnace decreases due to gas expansion effects. For example, at room temperature the particle residence time within the furnace is on the order of 1 s. At 1000 °C, the residence time is estimated

to be ~ 0.06 s. Therefore, the processing times may not be sufficient to allow formation of stoichiometric SiO_2. Second, formation of volatile suboxide species such as SiH_2SiO could lead to desorption of SiO. On extended silicon surfaces at low oxygen pressures and high substrate temperatures, a so-called "active" oxidation process has been proposed to occur.[3.33] Under "active" process conditions, the reaction of molecular oxygen with a silicon substrate produces SiO, a volatile suboxide which readily desorbs from the substrate leaving behind a clean silicon surface. Volatile suboxide desorption has been cited elsewhere to explain shrinkage during thermal oxidation of aerosolized Si nanoparticles,[3.10] and unexpected loss of Si in the case of thermally oxidized Si nanowires[3.34] though no compositional analysis was provided in either report. In our results, the IR peaks at 790 and 2175 cm^{-1} in Figure 5b are only visible between 500 and 700 °C. Moreover, the peak at ~2175 cm^{-1} has also been associated with the volatile suboxide SiH_2SiO.[3.35] These two IR peaks suggest that the limited growth at temperatures less than ~700 °C could be due to suboxide desorption. However, we observed no decrease in particle diameter at conditions similar to those in the report where nanoparticle shrinkage was observed. Perhaps a more plausible explanation is that the peaks at 790 and 2175 cm^{-1} are due to O_2SiH_2 rather than SiH_2SiO, and that at temperatures above 700 °C, additional oxygen backbonds to the O_2SiH_2 producing O_3SiH.

Although it is difficult to make a direct quantitative comparison between the FTIR, ToF-SIMS, and XPS data, these techniques all qualitatively demonstrate that more oxygen is incorporated as the furnace temperature setting is increased. ToF-SIMS data indicate that Si–O related species are not abundant on the particle surfaces at

temperatures below ~800 °C, the temperature at which particle growth begins to exhibit a definite plateau. The FTIR and TDMA data indicate that once intermediate suboxide species such as O_2SiH_2 evolve to O_3SiH at temperatures ≥ ~ 800 °C, particle growth exhibits a plateau; changes in particle surface chemistry are limited. XPS results further substantiate that at temperatures above 800 °C, little change is apparent in the particle surface chemistry with increasing temperature.

One of the original purposes for conducting these experiments was to employ the particle size selection capacity of the DMAs to examine oxide growth kinetics on different sized particles when processed under similar conditions. A key conclusion of a previous report regarding 10 nm particle kinetics was that particle growth occurred in two regimes.[3.14] The first regime was one in which oxygen had direct access to the silicon surface resulting in rapid oxide formation and particle growth. The second regime was one in which growth above and beyond that exhibited in the first regime was much slower due to the presence of an oxide shell. Oxygen therefore had to diffuse through the shell to react at the Si–oxide interface making growth kinetics diffusion-controlled. Data for both 6 and 10 nm particles indicate that at temperature settings of 800 °C and above, the transition between rapid and slow growth occurs after particles exhibit similar changes in diameter. The model developed by Liao et al.[3.14] captures the essence of this transition regime well. However, a direct comparison between kinetics parameters of the 6 and 10 nm particles is not straightforward for several reasons. One experimental improvement for these measurements was the ability to achieve a smaller carrier gas oxygen content than was studied for the 10 nm particles. For the 6 nm particle experiment, the smallest carrier gas oxygen content was 0.4%, nearly 10 times less than

the smallest considered in the 10 nm experiment. The primary effect is seen most readily in the initial slopes of the particle diameter vs. carrier gas oxygen fraction curves as shown in Figure 3.4. The initial slopes for 6 nm particles rise more abruptly than those did for the 10 nm particles, suggesting that at elevated temperatures silicon nanoparticles require very little oxygen to elicit growth due to oxide formation. If smaller amounts of carrier gas oxygen had been considered in the 10 nm experiments, the reported activation energy and oxidation rate constant would likely have been quite different. FTIR results reported here also show that hydrogen desorption and oxidation occur simultaneously, and XPS results confirm that the oxide formed is not SiO_2. These observations add significant complexity to the oxidation model previously proposed. Therefore, a direct kinetics comparison is not straightforward. At this point perhaps the most straightforward way to compare results from the two reports is on a particle diameter change basis. In that regard, 6 nm particles generally exhibit less growth than 10 nm particles when compared under similar processing conditions.

A self-limiting oxidation phenomenon is frequently cited as one reason why smaller particles exhibit less growth due to oxidation than larger particles.[3.9,3.36,3.37] The common explanation is that as the particles oxidize, a complex state of stress beyond that inherent to a curved particle surface[3.38] develops due to the lattice mismatch between the Si core and the SiO_x shell. As the oxide shell grows, the Si core shrinks and oxide is pushed out to accommodate growth of new oxide at the Si–SiO_x interface. The resulting compressive stress slows oxide growth by suppressing oxygen diffusion through the oxide shell to the silicon core, especially at temperatures below the viscoelastic transition temperature of SiO_2.[3.36] Since smaller particles have a greater radius of curvature, they

develop a greater compressive stress and therefore oxidize more slowly than larger particles.

Although self-limiting oxidation can partially explain the growth differences between 6 and 10 nm particles, we cannot directly compare our results to existing self-limiting models with confidence. First, in the absence of 10 nm particle growth data in 0.4% O_2 carrier gas, we can not conclusively state which particles grow more quickly in the initial fast oxidation regime. Many self-limiting oxidation models are also based upon significantly longer reaction times than are possible within an aerosol flow tube reactor. Extrapolating those results to time scales considered in this report are questionable at best. Second, most self-limiting nanoparticle oxidation models assume either explicitly or implicitly that the oxide is SiO_2. This could indeed be the case for larger particles, much thicker oxides, or oxidation times significantly longer than examined in this report. Our results, however, demonstrate that the oxide formed is sub-stoichiometric. Therefore, the assumption of an abrupt transition from Si to SiO_2 is not valid. Moreover, not all proposed silicon nanoparticle thermal oxidation models apply to hydrogen-terminated particles. We have shown that oxidation and hydrogen desorption occur simultaneously and that hydrogen remains even after processing under the highest oxidation temperatures. The presence and tenacity of hydrogen and its potential to impede oxide growth cannot be easily disregarded. In many silicon nanoparticle oxidation reports, the particles are also encapsulated within an oxide shell or embedded within an oxide layer on a wafer prior to data collection. Thus, particle oxidation has already occurred to some extent before controlled oxidation has even begun to be monitored.

A concise model describing thermal oxidation growth kinetics of hydrogen-terminated silicon nanoparticles should include similar data from particle sizes both smaller than 6 nm and larger than 10 nm. Smaller carrier gas oxygen fractions should also be considered if possible. For completeness, changes in surface chemistry, the state of stress, and oxide thickness would also be included.

3.5 Conclusions

Given the increasing interest in producing and tailoring nanoparticles entirely in gas-aerosol processes, a method has been demonstrated by which silicon nanoparticle surface chemistry changes can be evaluated *in situ*, and size changes can be measured online. Silicon nanoparticles produced in an RF plasma were thermally oxidized by molecular oxygen in an aerosol flow tube reactor. Size and compositional changes of oxidized 6 nm silicon particles were studied using a TDMA apparatus, FTIR, ToF-SIMS, and XPS. In their as-produced state, the particles were essentially hydrogen terminated. As the particles were heated, a small decrease in particle diameter was observed at temperatures less than 500 °C and attributed to hydrogen desorption. This temperature was not sufficient to cause significant oxidation as demonstrated by the IR measurements. Particle growth primarily occurred at processing temperatures greater than 700 °C, required very little oxygen, and was attributed to suboxide formation according to FTIR and XPS measurements. However, growth rapidly slowed after the formation of a substoichiometric layer at 800 °C.

Chapter 4.

Thermally Induced Hydrosilylation at Deuterium-Terminated Silicon Nanoparticles: An Investigation of the Radical Chain Propagation Mechanism

Isotopic labeling techniques were employed to study alkene addition to hydrogen- and deuterium-terminated silicon nanoparticles. Deuterium-terminated silicon nanoparticle synthesis is described, as is the characterization of fresh deuterium-terminated particles by transmission electron microscopy (TEM), X-ray photoelectron spectroscopy (XPS), and in situ Fourier transform infrared spectroscopy (FTIR). Particles were refluxed in pure 1-dodecene and subsequently characterized by FTIR and nuclear magnetic resonance (NMR) spectroscopy. ^{1}H NMR results showed features consistent with dodecyl-terminated nanoparticles. Infrared absorption spectra of refluxed particles showed strong evidence of new C-D bond formation, which is consistent with a radical chain mechanism for alkene addition by hydrosilylation.

4.1 Introduction

Silicon nanoparticles have received attention for their potential use in applications such as improved photovoltaic devices,[4.1] photoluminescent devices,[4.2] and biophotonics.[4.3] In many applications it is desirable to tailor the particle surfaces to optimize the desired physical properties (e.g., luminescent efficiency)[4.4] or to provide chemical functionality that promotes particle attachment to specific biological entities.[4.5] The ideal particle synthesis method would either directly install the desired surface functionality during synthesis or it would provide a surface amenable to easy post-synthesis modification.

One post-synthesis modification procedure involves hydrosilylation in which an alkene or alkyne reacts with a hydrogen-terminated Si surface to replace a Si–H bond with a Si–C bond. Thermal, catalytic, and photochemical methods have been developed to promote hydrosilylation on single-crystal silicon surfaces,[4.6,4.7] on porous silicon,[4.8-4.10] and on silicon nanoparticles.[4.4,4.11,4.12] Linford et al.[4.6] proposed that thermally driven hydrosilylation on hydrogen-terminated silicon occurs via a radical chain mechanism, as shown in Scheme I. The proposed initiation step is formation of a silyl radical at the hydrogen-terminated silicon surface. The newly formed silyl radical then attacks the C=C or C≡C bond of an unsaturated hydrocarbon, such as a terminal alkene or alkyne. The result is the formation of a new covalent Si–C bond and radical migration onto the secondary hydrocarbon carbon atom. The hydrocarbon radical next extracts a hydrogen atom from a neighboring Si–H bond at the H-terminated silicon surface, resulting in a satisfied hydrocarbon chain and a new silyl radical on the silicon surface. The end result is a closed-shell hydrocarbon chain and a new silyl radical on the silicon surface.

Another hydrocarbon molecule can react at this site; and in this manner, the reaction propagates the silicon surface. Other mechanisms have been proposed,[4.13] but experimental evidence is lacking. Different bonding configurations resulting in alkylated and/or 'cross-linked' particles have also been suggested as potential reaction products.[4.14]

Scheme I. The proposed radical chain hydrosilylation mechanism with a terminal alkene on a hydrogen–terminated silicon surface.

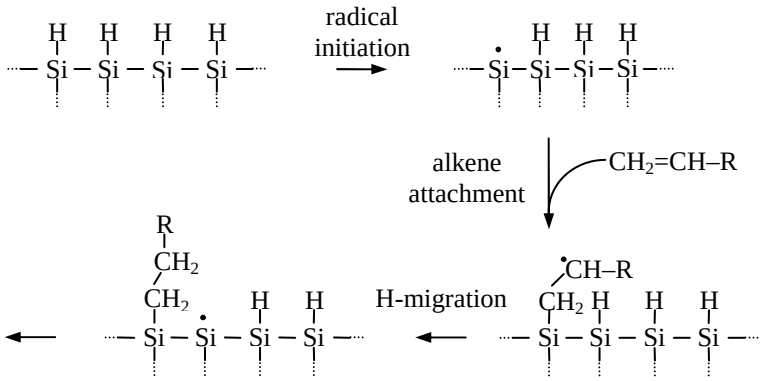

Strong experimental evidence supporting the radical chain mechanism on hydrogen-terminated single crystal silicon has been obtained under ultrahigh vacuum conditions using scanning tunneling microscopy.[4.7,4.15] Vapor phase adsorption kinetics data consistent with the proposed mechanism have also been reported.[4.16] However, experimental evidence in support of the radical chain mechanism on highly irregular hydrogen-terminated silicon surfaces such as porous silicon (p–Si) or silicon nanoparticles is scarce. In perhaps the most extensive study,[4.17] computational and experimental results of hydrosilylation on deuterated p–Si were presented. The authors of that study used infrared spectroscopy to monitor reactions of deuterium atoms that

were originally adsorbed at the p–Si surface. The idea was that if the radical chain mechanism was operative, deuterium–terminated p–Si refluxed with unlabelled terminal alkenes should react to form new C–D bonds. Although the alkylated p–Si sample exhibited increased infrared intensity in the region where C–D stretching vibrations were anticipated (~2100 – 2200 cm^{-1}), no distinct infrared signature was observed that could be unequivocally assigned to a C–D stretching vibration. The authors also presented computational results, which in concert with their experimental results, allowed them to infer that new C–D bonds had formed, thereby supporting a radical chain mechanism on an irregular surface like p–Si. One limitation of this study, however, is that the authors could not unambiguously distinguish between the C–D stretching vibration and the SiH stretching vibration of the back-bonded O_xSiH_y group.[4.18] To our knowledge, no experimental results supporting the radical chain mechanism on hydrogen- or deuterium-terminated silicon nanoparticles have been published.

In this chapter isotopic labeling techniques were employed to investigate 1-dodecene uptake by deuterium-terminated silicon nanoparticles. The experiments were specifically designed to interrogate the proposed radical propagation step, in which the secondary carbon radical abstracts hydrogen from a neighboring SiD group. Reaction initiation, which can occur in several ways, is not addressed in this work. The synthesis of deuterium-terminated silicon nanoparticles is described, and particle structure and composition are characterized by FTIR, XPS, and TEM. Fresh deuterium-terminated particles were subjected to reflux conditions in neat 1-dodecene and then examined with FTIR and NMR. FTIR spectra of the alkylated particles show unambiguous evidence for

C–D bond formation, thereby providing strong experimental support for the proposed radical chain mechanism.

4.2 Experimental

Deuterium-terminated silicon nanoparticles were synthesized via gas-to-particle conversion in a non-thermal, continuous flow RF plasma reactor similar to one described elsewhere.[4.19] As shown schematically in Figure 4.1, RF power at 13.56 MHz was coupled to a 20 cm long, 7 mm i.d. (9.5 mm o.d.) quartz tube reactor through an impedance matching network and two copper ring electrodes separated by 25 mm. Power to the matching network was controlled by setting the peak-to-peak voltage of a continuous sine wave applied to the RF amplifier input (E&I Model A150, Rochester, NY). Forward power of ~40 W, as indicated by the RF amplifier power meter, was used for these experiments. Reflected power was generally less than 2 W.

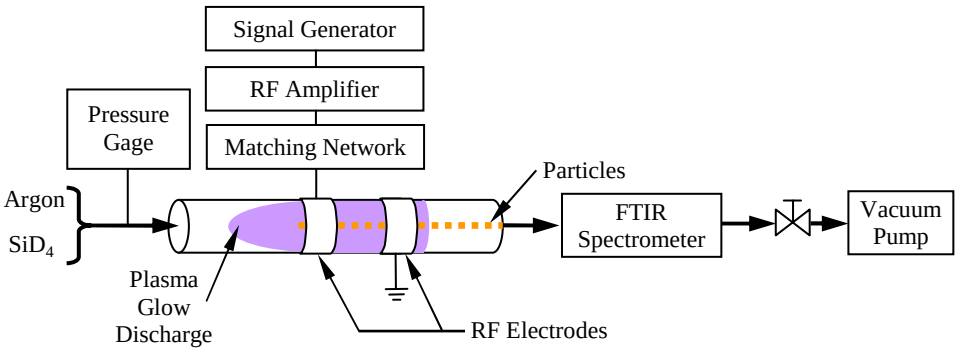

Figure 4.1. Schematic of the particle synthesis apparatus.

A silane-d_4/argon gas mixture (0.5% SiD_4 in 99.5% argon, hereafter referred to as silane) and argon were introduced into the quartz tube reactor though mass flow controllers set to provide 100 sccm argon and 50 sccm silane. The reactor pressure, ~6.5

Torr, was measured immediately upstream from the quartz tube and controlled with a pressure regulating valve positioned between the FTIR spectrometer (Magna-IR Spectrometer Model 550, Nicolet Instrument Corp. Madison, WI) and the vacuum pump (Leybold D90AC, Export, PA) as shown in Figure 4.1.

Nanoparticles synthesized within the plasma reactor flowed directly into the FTIR spectrometer analysis chamber for *in situ* characterization. Within the spectrometer analysis chamber, a hybrid flow-through gas cell consisting of a short length of stainless steel tube capped on both ends by infrared transparent windows was used to collect particles for analysis. Two ports located at opposite ends of the steel tube served as entry and exit points through which the aerosol from the plasma reactor flowed. Between the two ports, a small piece of wire mesh was placed across the inside of the hybrid gas cell. As aerosol from the plasma reactor flowed through the gas cell tube, particles were allowed to accumulate on the mesh for approximately 1 minute (the time required to produce an IR spectrum with acceptable signal-to-noise ratio). After sufficient mass had collected, gas flows to the plasma reactor were shut off or diverted through another vacuum pump; residual aerosol within the gas cell was evacuated; and spectra of particles accumulated on the mesh were recorded in transmission mode from 650–4000 cm^{-1} at 2 cm^{-1} resolution and averaged over 16 scans.

XPS was also employed to characterize fresh, deuterium-terminated particles. A Surface Science Instruments Model SSX–100 system (monochromated Al K_α X-rays) was used to record survey- and higher-resolution Si(2p) spectra at 150 and 50 eV pass energies, respectively. The analysis chamber base pressure was better than 5×10^{-9} torr, and sample charging offsets were referenced to the C(1s) peak at 284.6 eV. Particles for

XPS characterization were collected on wire meshes in a manner similar to that in which particles were collected for analysis by FTIR spectroscopy. To minimize adventitious contamination during transport between the particle synthesis apparatus and the XPS instrument, particle samples were sealed in their vacuum synthesis environment by two small valves. Particles were still exposed to air for several minutes, however, while being mounted on the sample stage and loaded into the airlock chamber.

Particle structure and morphology were studied by TEM at 300 kV (Technai G^2 F30, FEI Co., Hillsboro, OR). Copper TEM sample support grids coated with lacey carbon were attached to the end of a copper electrode and inserted into the aerosol flowing from the plasma reactor. Particles were then extracted electrostatically from the flowing aerosol stream onto the TEM sample grids by applying +300 VDC to the copper electrode for ~10 seconds.

Deuterium-terminated particles for surface modification by hydrosilylation were collected on wire mesh filters placed immediately downstream from the plasma reactor. When the filters were saturated with powder (~5–10 mg), particle-laden meshes were sealed in vacuum by two valves, and then transferred into a N_2-filled glove box where the meshes were immediately loaded into small flasks. Under N_2, 1-dodecene (12 mL) was transferred into the flasks, which were then sonicated to release particles from the mesh. Prior to use, 1-dodecene (Aldrich) was dried in CaH_2 and fractionally distilled under reduced pressure. Mixtures of 1-dodecene and particles were transferred into a refluxing apparatus in which all joints were sealed with Teflon sleeves. The reflux apparatus was covered with aluminum foil to limit the potential for unwanted photochemical reactions induced by ambient light, and the mixtures were subsequently refluxed (ca. 215 °C)

under N_2 for 2 hours with stirring. Solutions were cloudy prior to heating but appeared clear after approximately 15 minutes of heating.

After refluxing, the nanoparticles were isolated and purified by the following procedures. First, the nanoparticle/1-dodecene dispersion was concentrated to ca. 3 mL by removing excess 1-dodecene under vacuum and mild heat. Then, after cooling to room temperature, 15 mL of isopropanol (HPLC grade, Sigma-Aldrich) was added. The isopropanol was degassed and dried with 5 Å molecular sieves prior to use. Upon addition of isopropanol, nanoparticles precipitated out and were subsequently isolated by centrifuging. Liquids were then removed by applying vacuum overnight. This procedure afforded a brown, sticky product. A small amount of this product was spread onto a piece of stainless steel mesh and characterized by FTIR. Samples prepared in this manner are hereafter referred to as unwashed particles. Because the product isolated from this procedure was sticky, it was further purified by dissolution in 3 mL of toluene (spectrophotometric grade, Sigma-Aldrich) that had been dried in CaH_2 and freshly distilled. The nanoparticles were then precipitated by addition of 15 mL of isopropanol. After isolation via centrifuging and drying under vacuum overnight, a small collection of dry agglomerates was obtained. Samples prepared in this manner are hereafter referred to as washed particles. A small amount of the dry agglomerates was crushed onto a piece of stainless steel mesh for immediate characterization by FTIR using a diffuse reflectance (DRIFTS) accessory. Spectra were recorded from 650–4000 cm^{-1} at 2 cm^{-1} resolution and averaged over 16 or 32 scans. ^1H NMR spectra of the washed particles and 1-dodecene were collected in benzene-d_6 on a Varian 300 MHz spectrometer. The residual proton of the solvent at 7.15 ppm was used as the reference.

4.3 Results and Discussion

Representative TEM images of deuterium-terminated particles prior to refluxing are shown in Figure 4.2. The bright field image in Figure 4.2a shows a small section of a lacey carbon filament moderately covered with spheroidal particles. The size distribution of particles appears relatively narrow with most particles between ~ 4 and 6 nm in diameter. The inset in Figure 4.2a shows the corresponding selected area diffraction pattern in which three distinct rings are visible. These rings correspond well with the (111), (220), and (311) reflections of bulk crystalline silicon. The higher magnification image in Figure 4.2b, showing numerous particles exhibiting lattice fringes, further establishes that the particles are crystalline. D-terminated particles shown in the images are indistinguishable from H-terminated particles synthesized under similar conditions (Figure 4.2c).

XPS spectra of deuterium-terminated particles are shown in Figure 4.3. The survey scan in Figure 4.3a shows four main peaks at ~100 eV [Si(2p)], ~151 eV [Si(2s)], ~285 eV [C(1s)], and ~532 eV [O(1s)]. The Si(2p) peak shown in Figure 4.3b is symmetrical and with little evidence of chemically shifted features, as suggested by the single fitted (Gaussian–Lorentzian: 80%–20%) curve.

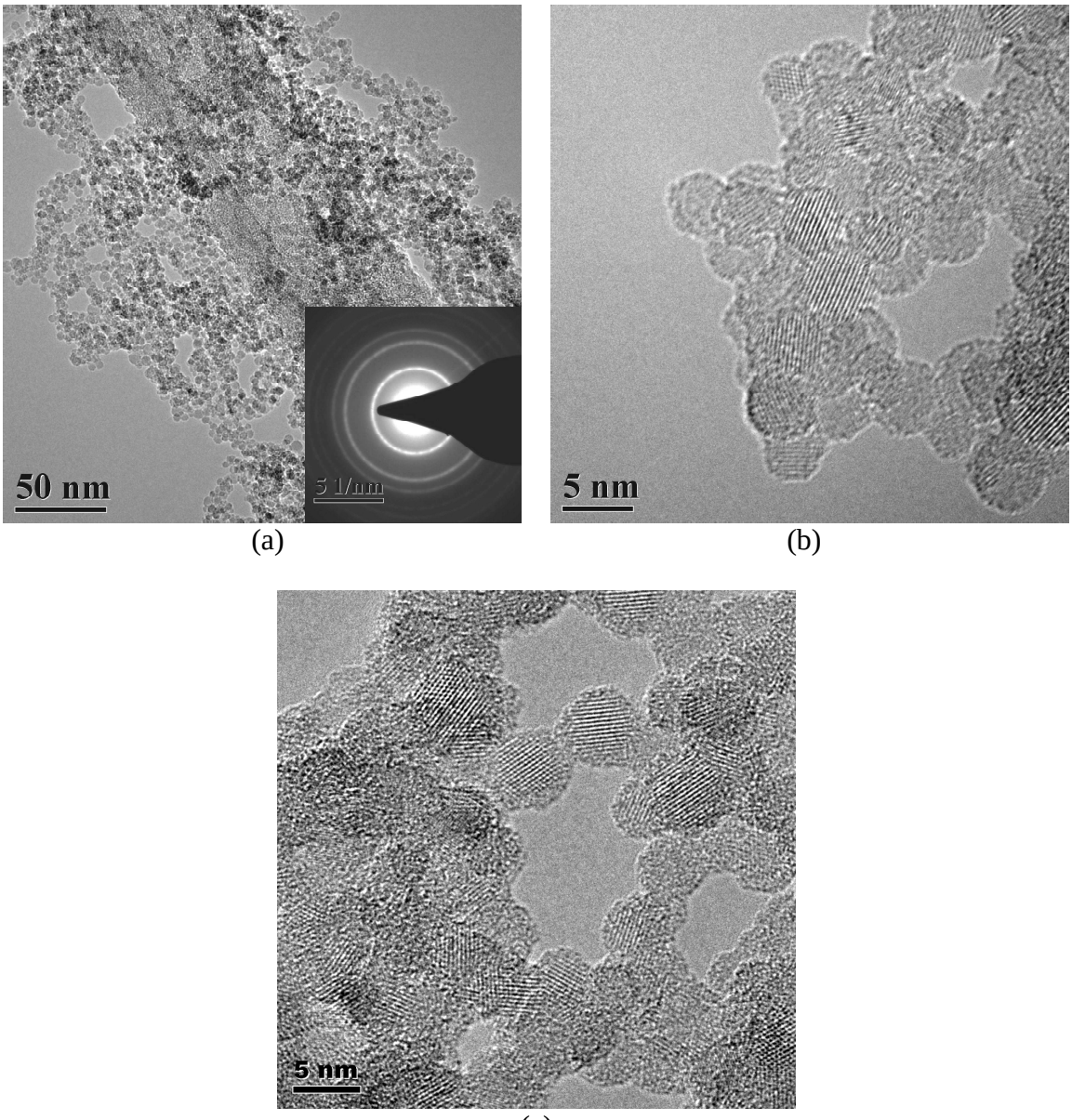

(a) (b)

(c)

Figure 4.2. Representative TEM images. (a) A bright field image showing agglomerated particles supported on a filament of lacey carbon. The inset selected area diffraction pattern shows three distinct rings corresponding to (111), (220), and (311) bulk Si reflections. (b) A higher magnification image showing lattice fringes suggestive of crystallinity. (c) Hydrogen-terminated silicon nanoparticles synthesized under the same conditions as deuterium-terminated particles.

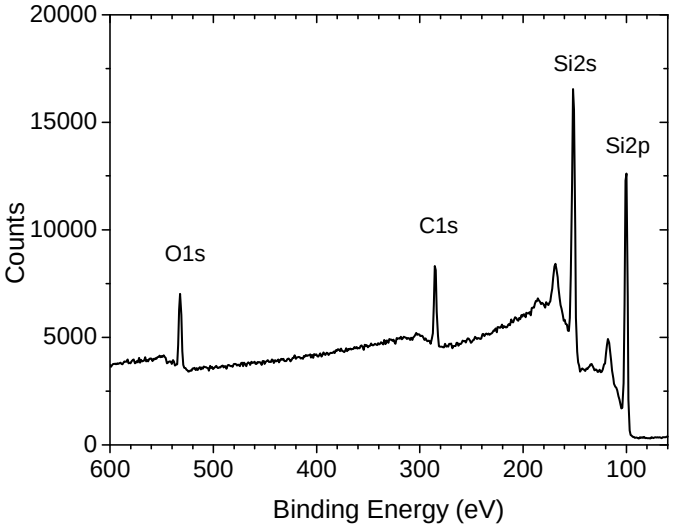

(a)

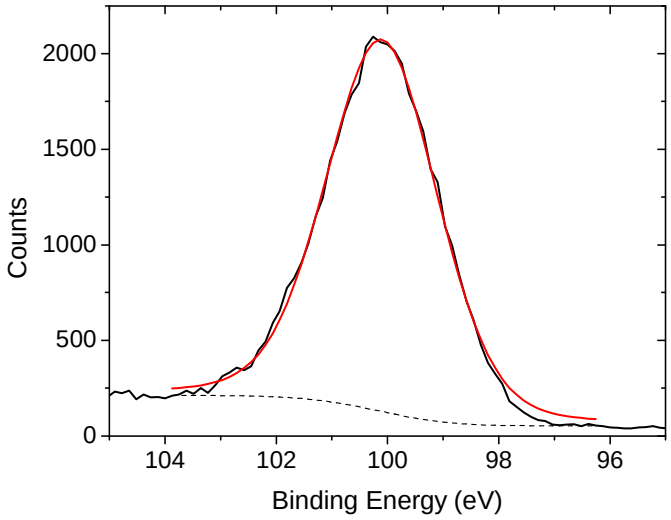

(b)

Figure 4.3. XPS spectra of deuterium-terminated particles. (a) Survey scan recorded at 150 eV pass energy and (b) a higher resolution Si(2p) peak recorded at 50 eV pass energy.

Quantitative analysis of the XPS spectrum in Figure 4.3a indicates that the concentration of oxygen associated with freshly prepared particle samples was less than 7 at %, assuming all oxygen was adsorbed onto the Si surface. Drawing more extensive conclusions about the state of oxidation from broadened peaks is not straightforward due to the nature of the particle sample and is outside the scope of this work. Nevertheless, if significant oxidation of the particles had occurred, chemically shifted peaks would appear at slightly greater binding energies than the elemental Si(2p) peak at ~100 eV, and the Si(2p) peak would exhibit more asymmetry towards the high binding energy side.[4.20] That the Si(2p) peak is broad can be partially explained as an artifact of roughness inherent to a nanoparticle powder sample.[4.21] Also inherent to a nanoparticle powder sample is the large surface-to-volume ratio compared to that of bulk silicon. If a bulk silicon sample and a silicon nanoparticle powder sample both exhibited suboxide surface layers of similar thickness and chemical composition, intensities of chemically shifted contributions to the Si(2p) region would be greater for the powder sample than the bulk sample. The low intensity O(1s) peak and the symmetric Si(2p) peak of Figure 4.3b demonstrate that oxide formation during particle synthesis is minimal. This conclusion is supported by the absence of CH_x and Si–O–Si stretching features in the *in situ* FTIR spectrum of fresh deuterium-terminated particles in spectrum 1 of Figure 4.4. The C(1s) and O(1s) peaks are therefore attributed to adventitious contamination.

Representative FTIR spectra of several particle samples are shown in Figure 4.4a. The *in situ* transmission spectrum of unmodified deuterium-terminated particles shown as spectrum 1 is dominated by an intense absorption comprising several peaks around 1525 cm^{-1}. A truncated feature also appears near 650 cm^{-1}. This feature no doubt extends

below the detection limit of the spectrometer. Spectrum 2, which was obtained in DRIFTS mode, was recorded of unwashed particles. Spectrum 3, also obtained in DRIFTS mode, was recorded of washed particles. The low intensity peaks between ~2000 and 2300 cm^{-1} of spectra 2 and 3 are especially germane to the proposed propagation step since they occur in the region anticipated of CD stretching vibrations.

A magnified view of the CD, SiH_x, and O_xSiH_y stretching region for each spectrum in Figure 4.4a is shown in Figure 4.4b. Spectrum 1, the *in situ* transmission spectrum of unmodified deuterium-terminated particles, exhibits almost no signal above the background noise level. Spectra 2 and 3, recorded of unwashed particles and washed particles, respectively, both show broad absorptions near 2140 cm^{-1} with small shoulders at lower wavenumbers. Absorptions were not observed between 2150 and 2250 cm^{-1} in any of the spectra recorded immediately after particles were exposed to air.

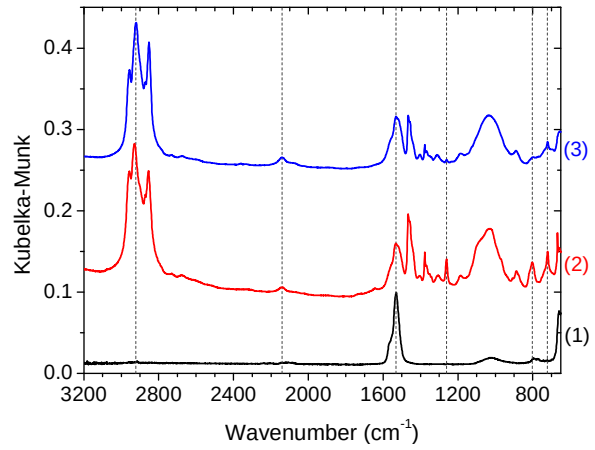

(a)

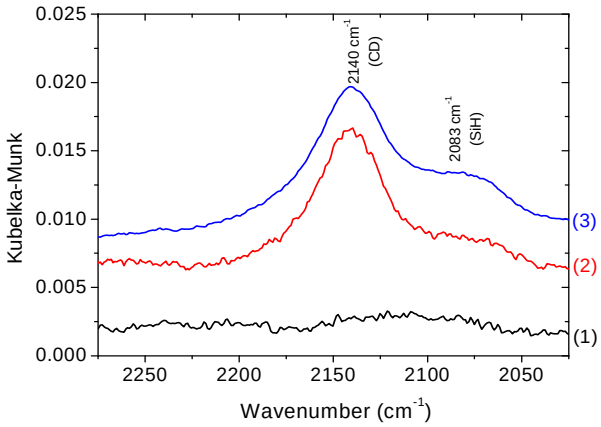

(b)

Figure 4.4. Representative FTIR spectra of several particle samples. Spectra have been offset along the abscissa to show features more clearly. (a) Numbered spectra correspond to (1) *in situ* transmission spectrum of deuterium-terminated particles, (2) DRIFTS spectrum of unwashed particles, and (3) DRIFTS spectrum of washed particles. (b) A closer view of the region in which CD, SiH, and O_xSiH_y exhibit infrared absorption. Note that the abscissa is shown in units of Kubelka–Munk. Strictly speaking, this conversion only applies to spectra 2 and 3. Spectrum 1 has not been converted and is shown in absorbance format.

The *in situ* spectrum of Figure 4.4, 1, shows peaks near 1525 cm^{-1} that correspond well with SiD_x stretching vibrations observed on other deuterated silicon surfaces.[4.22-4.27] On the basis of the anticipated frequency shift due to isotopic substitution, the truncated peak at 650 cm^{-1} is attributed to deformation modes of silicon deuteride groups. As the images in Figure 4.2 show, the particle synthesis conditions employed here lead to spheroidal particles. Although small facets of crystalline surfaces may be present, the highly curved particle surfaces present numerous structural environments for deuterium bonding states. Isolated SiD, SiD_2, SiD_3, clustered states, dimerized structures, and other polyhydrides are all probably contributing to the infrared absorption spectrum.[4.27,4.28] The surface composition of deuterium-terminated particles, potentially comprising a multitude of functional groups crowded together on highly curved particle surfaces, is far from an ideally-terminated, unstrained surface.[4.29] Nevertheless, evidence presented in this contribution (*vide infra*) suggests that the mechanism shown in Scheme I is feasible. Taken together, Figures 4.2–4.4 demonstrate that deuterium-terminated silicon nanoparticles have been synthesized, and that the particles largely comprise oxide-free, spheroidal, single-crystal entities.

Refluxed particles exhibit several infrared absorptions implying alkylation: 2800–3000 cm^{-1} (CH_x str.), ~1460 cm^{-1} (CH_3 asym. bend and CH_2 scissors), 1378 cm^{-1} (CH_3 sym. bend), and 722 cm^{-1} (CH_2 rock). From the FTIR spectra, it is not possible to deduce whether the attached ligands comprise intact, 12-atom-long chains of carbon. However, the small peak at ~722 cm^{-1} suggests that organic ligands longer than 4 carbon atoms are present.[4.30] SiD_x stretching vibration peaks near 1525 cm^{-1} also exhibit reduced intensity in spectra of refluxed particles compared to the *in situ* spectrum of fresh particles in

Figure 4.4a. Provided that thermal desorption behavior of hydrogen and deuterium from silicon nanoparticles is comparable, we do not expect to observe loss of deuterium to thermal desorption since the refluxing temperature used in this experiment is well below the temperatures necessary for thermal desorption of hydrogen from silicon nanoparticles.[4.31] According to Scheme I, intensity reduction of SiD_x peaks can partially be attributed to hydrocarbon radicals that extracted deuterium atoms from neighboring Si–D bonds at D-terminated particle surfaces.

Persistent absorptions due to SiD_x stretching modes observed of refluxed particles suggest that less than 100% of the particle surface sites are alkylated. This is not surprising since steric effects almost certainly preclude complete substitution of the surface hydrides with alkyl chains. As originally noted by Linford and Chidsey,[4.6] silicon atom spacing on the unreconstructed Si(111) surface (3.84 Å) is incompatible with 100% substitution of alkyl chains (4.6 Å diameter). Further experimental and computational studies have emphasized this point, and roughly 50% alkyl substitution on various H-terminated, bulk crystal silicon surfaces is generally considered maximal coverage.[4.32-4.35] Methyl groups imparted through a chlorination/alkylation process (*not* a hydrosilylation process) are one of the few hydrocarbon functional groups that have been observed to cover 100% of the surface sites on unreconstructed Si(111).[4.36] Estimates of the quantity of SiD_x bonds reacted away during reflux to quantify alkyl substitution were not pursued because no straightforward technique is available that allows a quantitative comparison of integrated peak areas between spectra recorded in transmission mode and diffuse reflectance mode. Nevertheless, persistent SiD_x modes after refluxing are consistent with

steric limitations, and regardless of the degree of coverage, alkylation was adequate to allow particles to remain stably dispersed in solution.

Several differences between unwashed and washed particles are apparent in the FTIR spectra of Figure 4.4. First, the methylene asymmetric stretching peak of washed particles occurs at lower wavenumbers (2920.7 cm^{-1}) than the same peak of unwashed particles (2928.4 cm^{-1}). The shift to lower wavenumbers suggests the adsorbed alkyl ligands exhibit some degree of ordering compared to free alkanes.[4.37] Second, other absorption features in spectrum 2 are not consistent with dodecyl ligands. For example, unwashed particles exhibit two strong peaks of similar intensity at ~802 cm^{-1} and ~1261 cm^{-1}. Considered together, these peaks point to $Si(CH_3)_2$ functionality.[4.38] This result was not expected. However, these peaks are essentially absent after washing the particles only once, which suggests that they are associated with species not strongly bound to the particle surfaces. The spectrum of unwashed particles also shows a small absorption at ~1640 cm^{-1} (C=C stretch) and a rather strong absorption at ~722 cm^{-1} (CH_2 rock) suggesting that unreacted 1-dodecene was physisorbed at unwashed particle surfaces. A broad absorption near 1030 cm^{-1} that is associated with early stages of silicon oxidation is also present in spectrum 2 and in spectrum 3. Notably, the intensity of this peak does not increase with washing. This is indirect evidence showing that the refluxed particles are passivated with alkyl ligands.

Although the mechanism of Scheme I indicates ligand attachment through the α-carbon of the parent alkene, attachment at the β-carbon is also feasible and has been demonstrated of porous silicon[4.39] and of silicon nanoparticles.[4.40] One primary difference between those reports and the current work is that hydrosilylation was

photochemically promoted rather than thermally promoted as was done here. With sufficient FTIR resolution, differences in bonding configurations should be detectable in isotopically labeled systems.[4.41] For example, infrared signatures of deuterated methylene (–CHD–) should occur if the Si–C bond forms at the α-carbon atom of the 1-alkene. Alternatively, if the Si–C bond forms at the β-carbon atom of the 1-alkene, signatures of deuterated methyl groups ($-CH_2D$) should occur. These signatures were not detected in this investigation, probably because of the weak oscillator strength of isotopically labeled of functional groups, which are likely overshadowed by infrared absorptions of unlabeled groups. Provided that particles can remain stably dispersed in solution, a distinct advantage of nanoparticle systems over bulk systems is that NMR techniques can provide a more complete picture of the alkyl functionality at particle surfaces. For example, bonding of the 1-alkene to silicon particles through the α- or β-carbon has been shown for several organic functional groups on silicon nanoparticles.[4.40,4.42] To that end, ^{1}H NMR spectra of purified 1-dodecene and washed particles were recorded.

Figure 4.5 shows ^{1}H NMR spectra of free 1-dodecene (i) and of alkylated, washed particles (ii), both of which were dissolved or dispersed in C_6D_6. Lines labeled with + are attributed to residual isopropanol, toluene, and small amounts of unreacted 1-dodecene, which attests to the difficulty of removing physisorbed 1-dodecene and other chemicals from particles processed in solution. As the figure shows, signatures of 1-dodecene protons at the C1, C2, and C3 positions are essentially absent in the spectrum of alkylated particles. For alklyated particles, the methyl triplet (0.9 ppm in 1-dodecene) shifts downfield to ~1.04 ppm (a), and the methylene protons (1.26 ppm in 1-dodecene) shift

downfield to ~1.5 ppm (b). Both peaks exhibit significant broadening due to the constrained motion of the alkyl ligands bound to the comparatively large particles that tumble at a slower rate than free 1-dodecene. Alkanethiol-capped gold nanoparticles exhibit similar features near 1.0 ppm (methylene protons) and 1.5 ppm (methyl protons).[4.43,4.44] A smaller peak also appears at ~0.54 ppm (c) in spectrum ii. The location of this peak, which incidentally does not appear in spectra of alkanethiol-capped gold particles, is in agreement with protons of methylene groups bound to silicon (Si–CH_2–), as has been observed of triethylsilane and trihexylsilane.[4.45] Small peaks near 3.65 ppm could be from protons adjacent to Si as in trihexylsilane.[4.45] Due to the significant line broadening, it is not easy to verify α- or β-carbon bonding. However, if protons of methylene groups bound to other carbon atoms contribute to the peak at 1.5 ppm (area ≈ 70), if protons of methyl groups contribute to the peak at 1.0 ppm (area ≈ 13.7), and if protons of methylene bound to silicon contribute to the peak at 0.54 (area ≈ 0.85), then quantitative analysis is consistent with ligands that are intact, 12-atom-long chains of carbon that are more likely bound to the particles through the α-carbon than the β-carbon.

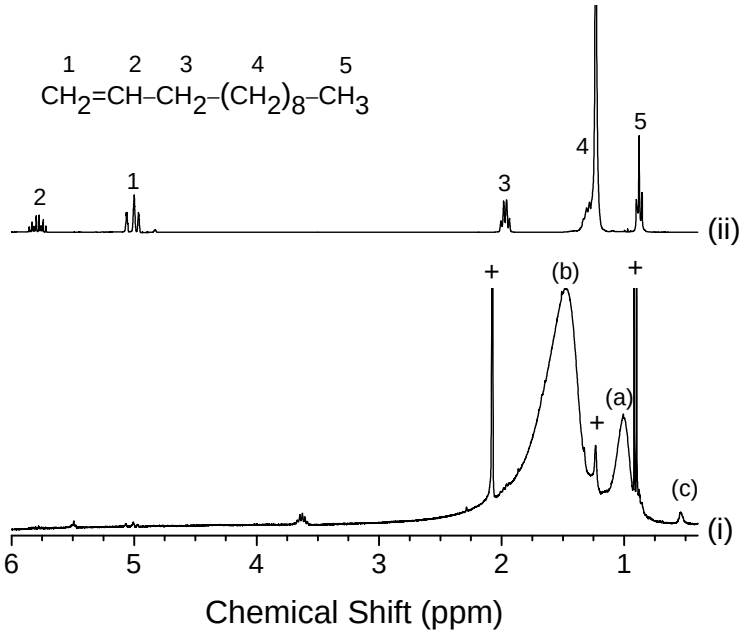

Figure 4.5. ^{1}H NMR spectra of (i) free 1-dodecene, and (ii) alkylated silicon particles, both in C_6D_6.

In Figure 4.4b, spectra 2 and 3 both show broad absorptions with a dominant peak at ~2140 cm^{-1} and a small shoulder centered near 2083 cm^{-1}. The peak at ~2140 cm^{-1} occurs in the correct region to consider attributing it to the C–D stretching vibration. Nevertheless, closer scrutiny is required since at least three assignments are possible. First, SiH_3 groups have been reported at similar wavenumbers on various hydrogen-terminated silicon surfaces.[4.46] However, since no appreciable intensity above background level is observed at similar wavenumbers in the *in situ* transmission spectrum of fresh deuterium–terminated particles, and the formation of SiH_3 groups is unlikely during the refluxing procedure, this assignment can be ruled out. For a similar reason, the peak is probably not related to oxygen backbonded to silicon in the form of $OSiH_3$

even though peaks near 1030 cm^{-1} suggest Si–O–Si bonds were present. The next logical assignment for the peak at 2140 cm^{-1} is the C–D stretching vibration. To confirm this assignment, peak evolution in the region between ~2050 and 2275 cm^{-1} was monitored as the particles were exposed to air. The idea was that if SiH_x (x = 1– 3) groups were all present on the particle surfaces at detectable levels after refluxing, peaks related to backbond oxidation should evolve with time, and intermediate oxidation states corresponding to $OSiH_3$ (~2150 cm^{-1}), O_2SiH_2 (~2200 cm^{-1}), and O_3SiH (~2250 cm^{-1}) would appear.[4.47] If the peak at 2140 cm^{-1} was due to C–D stretching, the peak should *not* exhibit appreciable shift as the particles oxidize.

Figure 4.6 shows how absorptions in the SiH_x, CD, and O_xSiH_y stretching region evolved during air exposure. For these spectra, washed particles supported on small pieces of stainless steel mesh were simply exposed to air, and FTIR spectra were periodically recorded in DRIFTS mode. Spectra shown in Figure 4.6 have been normalized to the peak near 2140 cm^{-1}. As the figure shows, with time a single peak evolves at ~2243 cm^{-1} (O_3SiH) accompanied by the simultaneous attenuation of the peak near 2083 cm^{-1} (SiH). Moreover, distinct peaks at 2150 cm^{-1} and 2200 cm^{-1} are not readily apparent, which implies that SiH_2 and SiH_3 groups are not present at detectable levels. The peak at 2140 cm^{-1} exhibits a minor shift to higher wavenumbers with continued exposure to air, but this shift is most likely due to the influence of the growing O_3SiH peak and the shrinking SiH peak. On the basis of these observations, the small shoulder at ~2083 cm^{-1} is attributed to SiH groups at the nanoparticle surfaces.

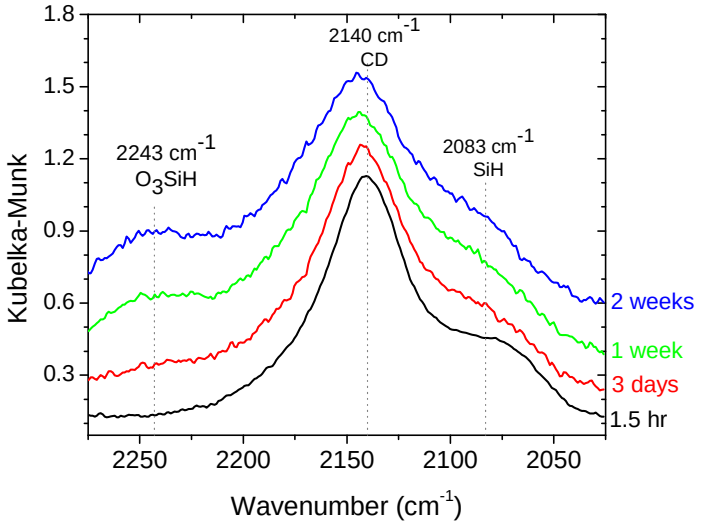

Figure 4.6. Evolution of SiH_x, O_xSiH_y, and CD stretching vibrations on alkylated particles due to native oxidation in air.

Peaks at ~2140 cm^{-1} in Figure 4.6 are attributed to the C–D bond. Several factors justify this assignment. Assuming the C–H bond force constant does not significantly change upon isotope substitution, the wavenumber shift of a deuterated methylene group can be estimated according to a simple harmonic oscillator approximation, $\bar{\nu}_{C-D}/\bar{\nu}_{C-H} = \sqrt{\mu_{C-H}/\mu_{C-D}} \approx 0.73$, where $\bar{\nu}$ is the wavenumber at which a particular vibrational mode is observed, and μ is the oscillator reduced mass.[4.48] The C–D stretching vibration peak should be observed near 2135 cm^{-1} according to this approximation. This estimate matches well with observations reported here. Perhaps a more convincing piece of evidence is that the peak at 2140 cm^{-1} in Figure 4.6 does not exhibit significant changes in shape or notable shifts to different wavenumbers during extended air exposure. If the peak at 2140 cm^{-1} was due to SiH_3, then the peak would

evolve from SiH_3 through different backbond oxidation states until it completely converted to the more thermodynamically stable O_3SiH commonly observed near 2250 cm^{-1}.[4.47]

The presence of CD functionality after refluxing suggests that the propagation stage of the hydrosilylation reaction could occur on silicon nanoparticles via the proposed radical chain route. As described previously, however, thermally induced hydrosilylation on deuterated porous silicon was regarded as a minority reaction pathway when using dilute 1-alkene solutions.[4.49] In that report it was concluded that the carbon radical intermediate was not satisfied by extracting deuterium from a neighboring Si–D group. Rather, the carbon radical was satisfied by abstracting a hydrogen atom from the solvent or an alkene molecule. However, the same authors later provided contrary evidence suggesting that the hydrosilylation reaction indeed propagated through a radical chain mechanism.[4.17] Results presented here provide strong experimental support for the proposed radical chain mechanism. However, hydrosilylation cannot be the only reaction taking place since it does not account for the presence of SiH or $Si(CH_3)_2$ groups observed of unwashed particles after refluxing. The source of these functional groups is not immediately apparent and requires further investigation.

One point that has not been addressed in the silicon nanoparticle hydrosilylation literature is the influence of the fresh particle surfaces on different steps of the hydrosilylation mechanism. This is relevant not only to silicon nanoparticles synthesized in non-thermal RF plasmas, but also to porous silicon, both of which can exhibit complex Si_xH_y surface structures. For example, consider higher hydrides such as SiD_2 and SiD_3 at particle surfaces. These functional groups almost certainly participate in hydrosilylation

by donating D atoms to satisfy carbon radicals formed during alkene addition to particle surfaces. Donation from these functional groups could terminate the propagation step while simultaneously leaving the local structure in an unstable configuration. Subsequent reorganization of Si and SiD_x bonds at the particle surfaces to lower energy configurations could then occur to satisfy newly formed dangling or strained Si bonds, or the newly formed dangling bonds could extract a H(D) atom from the refluxing alkene or solvent. These effects would partially account for both the persistent SiD_x functionality and the absorptions attributed to SiH bonds after refluxing. (This is another reason why estimations of SiD/SiH bonds reacted away during refluxing are not straightforward.) Unfortunately, the SiD_x stretching bands that persist after refluxing are sufficiently broadened so as to preclude artifact-free deconvolution and subsequent correlation to well characterized hydrogen-terminated Si surfaces. Alternatively, the SiH stretching peak appearing at ~2083 cm^{-1} after refluxing *is* consistent with the monohydride (SiH) peak observed on ideal, strain-free, extended Si(111) surfaces.[4.50] That infrared absorption occurs at 2083 cm^{-1} after refluxing can hardly be accidental given the disorder inherent to the deuterium-terminated nanoparticle surfaces considered here. In addition to Si–C bond formation, particle surface restructuring induced during hydrosilylation on nanoparticles is conceivable.

4.4 Conclusion

In summary, deuterium-terminated silicon nanoparticles were synthesized in a non–thermal, continuous flow RF plasma. Particles were ~4–6 nm in diameter and exhibited features characteristic of crystalline nanostructures. Particles refluxed in neat

1-dodecene exhibited features attributable to the formation of CD bonds in support of the radical chain propagation mechanism.

Chapter 5.

Modifying the Composition of Hydrogen–Terminated Silicon Nanoparticles Synthesized in a Non-Thermal RF Plasma

Hydrogen-terminated silicon nanoparticles were synthesized over a broad range of conditions in a continuous flow, non-thermal RF plasma. The effects of three operating parameters – RF power, reactor pressure, and hydrogen flow rate – were examined in terms of their effects on particle crystallinity, size, and surface composition. Silicon-hydrogen composition was characterized *in situ* by Fourier transform infrared (FTIR) spectrometry, and particle structural morphology was examined with a transmission electron microscope (TEM). By appropriately adjusting the operating parameters, amorphous or crystalline particles could be synthesized. Over the majority of settings examined, the minimum power required to produce crystalline particles was ~20-30 W. Depending on the parameter settings, particles could also exhibit hydrogen coverage ranging from predominantly monohydride (SiH) functional groups to more complex compositions of higher hydrides. For example, particles with the highest proportion of surface SiH bonds were consistently synthesized in the smallest diameter (4 mm i.d.) tube reactor.

5.1 Introduction

Silicon nanoparticle synthesis techniques are legion.[5.1] Many of the techniques strive to produce size monodisperse and crystalline nanoparticles, two properties that are desirable in many different applications.[5.2] One technique, gas-to-particle conversion in a continuous flow non-thermal RF plasma, has demonstrated the capacity to produce hydrogen-terminated, crystalline silicon nanoparticles with fairly narrow size distributions.[5.3] This technique also has other advantages such as low power requirements, a broad range of possible particle precursor gases and flow ratios, low apparatus temperatures compared to particle synthesis techniques employing thermal plasmas[5.4] or pyrolysis techniques in aerosol flow tubes,[5.5] and moderate pressures that do not require ultra-high vacuum processing techniques.

Particle synthesis in silane plasmas leads to hydrogen-terminated particles because the precursor gas contains hydrogen, and because SiH_x bonds at the particle surfaces are stable. Hydrogen at particle surfaces confers several benefits. It inhibits aggregation and sintering,[5.6] and it provides some passivation capacity towards unwanted reactions such as oxidation by air. Perhaps one of the more far-reaching benefits, however, is that a hydrogen adlayer provides a platform on which to implement sophisticated functionalization strategies such as hydrosilylation.[5.7-5.9] The inherent hydrogen termination also has the potential for simplifying surface tailoring modifications compared to other silicon nanoparticle synthesis techniques.[5.10] On the other hand, the surface composition of particles synthesized in a non-thermal RF plasma can be quite complex. Infrared spectra of silicon nanoparticles suggest that isolated SiH, SiH_2, SiH_3, clustered states, dimerized structures, and other polyhydrides could all be

crowded together on highly curved particle surfaces.[5.9,5.11-5.13] Some of those silicon hydrides may be undesirable in certain circumstances. Consider SiH_3, for example. Particles with this surface functional group are not necessarily optimized for hydrosilylation, a commonly applied silicon nanoparticle surface modification scheme. Another concern regarding SiH_3 is that it cannot strictly be considered part of the diamond cubic structure. Even though crystalline particles can be synthesized in non-thermal plasmas, surface silicon functional groups require at least two unstrained, covalent Si bonds with the underlying crystalline particle core to be considered part of the crystal.[5.14] SiH_3 can at most form a single Si–Si bond with the crystal core. Based on these two observations alone, better control and characterization of the gas-to-particle conversion process in non-thermal RF plasmas is desirable.

Particle formation in plasmas has been extensively examined both experimentally and computationally.[5.15] However, the extent to which the particle surface composition and structural morphology can be simultaneously controlled by making changes to plasma apparatus control variables is still not well documented or understood. High-level computational studies are generally limited to clusters or the very smallest particles because larger particles have too many atoms to allow computationally tractable simulations. Experimental studies regarding plasmas specifically designed to produce particles generally focus more attention on particle structural morphology (e.g., crystallinity) than on surface composition. As will be shown, plasma reactor control variables can be adjusted such that the particles are comprised of amorphous or crystalline silicon, or a combination of the two. Moreover, minor adjustments to the control variables can have significant impact on the final particle characteristics including

the surface hydride composition, an important parameter often only incidentally mentioned by experimentalists and generally left to more thorough investigation by computational means.[5.16] In addition to being important from the viewpoint of controlling particle surfaces for subsequent tailoring procedures, understanding the particle surface composition and structural morphology may also provide fundamental insight into reactions occurring within the plasma reactor, and therefore lead to a more complete understanding of silicon nanoparticle formation and their desirable photophysical attributes. Without the capacity to manipulate and control the silicon hydride functionality, the exact role of the particle surface in terms of desirable nanoparticle properties (e.g., luminescence) will also remain elusive.

In this chapter, a continuous flow non-thermal RF plasma is employed to study the extent to which plasma reactor control variables can be used to control the surface composition and structural morphology of hydrogen-terminated silicon nanoparticles. Reactor diameter, electrode spacing, power, pressure, and gas flow ratios provide an immense parameter space that can be explored and used to manipulate particle sizes, particle size distributions, and the chemical and structural morphologies. For these experiments, particles were synthesized over a wide range of operating parameters as summarized in Table A1 of Appendix I. Rather than presenting an analysis detailing the interaction of each control parameter, three specific examples are presented. In particular, the effects of RF power, reactor pressure, and hydrogen (H_2) flow rate are examined under slightly different processing conditions. Fourier transform infrared spectroscopy (FTIR) is used to characterize silicon–hydrogen functionality, and transmission electron microscopy (TEM) is used to examine structural morphology.

5.2 Experimental

Silicon nanoparticles were synthesized in a continuous flow non-thermal RF plasma reactor similar to one described elsewhere.[5.3] As shown schematically in Figure 5.1, power at 13.56 MHz was coupled to 20 cm long quartz tube reactors through an impedance matching network and two copper ring electrodes. Electrode spacing, measured as shown in Figure 5.1, was set at different values between 6 and 90 mm. Power to the matching network was adjusted by changing the peak-to-peak voltage of a continuous sine wave supplied to the input of a linear RF amplifier (E&I Model A150, Rochester, NY). Forward power indicated by the RF amplifier was taken as a measure of input power to the plasma reactor. Reflected power indicated by the RF amplifier was generally less than 5 W.

A silane-argon mixture comprised of 0.5% SiH_4 in 99.5% argon (hereafter referred to as silane), argon, and molecular hydrogen were introduced into the tube reactors though mass flow controllers that could be adjusted to provide different gas flow rate ratios. For the remainder of this contribution gas flow rate ratios are presented in the following format: argon/silane/hydrogen. For example, gas flow rates of 100 sccm of argon, 50 sccm of silane, and 10 sccm of H_2 are designated as 100/50/10. Plasma reactor pressure was measured immediately upstream from the quartz tube and controlled with a pressure regulating valve positioned between the FTIR spectrometer (Nicolet Magna IR, Model 550, Madison, WI) and the vacuum pump (Leybold, Model D90AC, Export, PA). Glow discharges were confined within the quartz tube reactors as shown in Figure 5.1b for all conditions described in this chapter.

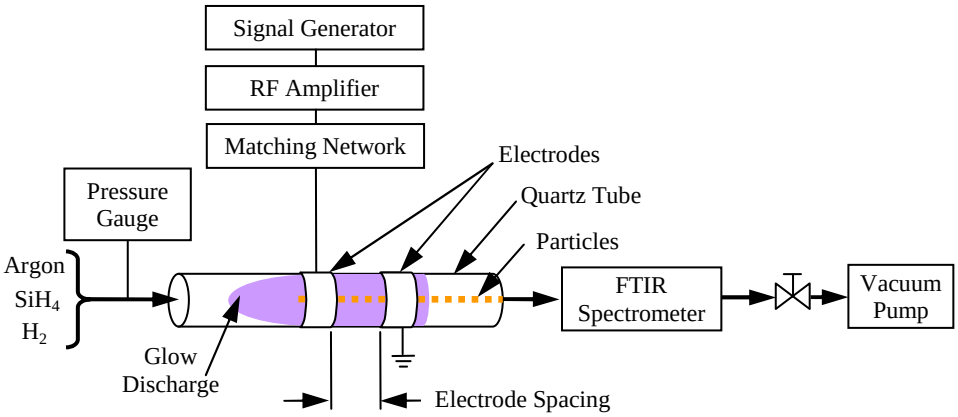

Figure 5.1. The particle synthesis apparatus. (a) A schematic showing the component layout. (b) A picture of the glow discharge contained within a 7 mm i.d. reactor at 7 Torr, gas flow ratios of 100/25/0, ~30 W forward power, and 25 mm electrode spacing. Flow direction is from left to right.

Particles synthesized in the plasma reactor flowed directly into the FTIR spectrometer for *in situ* analysis. Within the spectrometer, a custom flow-through gas cell consisting of a short piece of stainless steel tube capped on both ends by infrared transparent windows was used to collect particles for analysis. Two ports located at opposite ends of the tube provided entry and exit points through which the particles flowed. Inside the tube and between the two ports, a small piece of stainless steel wire mesh was clamped across the entire inner diameter of the gas cell to serve as a filter upon which particles were collected. Particles from the plasma reactor flowed through the gas

cell and were allowed to accumulate on the filter until an infrared spectrum with an acceptible signal-to-noise ratio could be recorded. Particle accumulation times varied with reactor settings but were generally less than two minutes. For the most highly dilute silane concentrations, however, particle collection times of up to 20 minutes were required when no aperture was used to restrict the filter. After a sufficient particle sample was collected, gas flows to the plasma reactor were either shut off or diverted through another vacuum pump, and residual precursor gases within the flow-through gas cell were evacuated. Alternatively, the silane and hydrogen mass flow controllers and the RF power were shut off and the apparatus was continuously purged with argon at approximately the same particle synthesis pressure. During particle collection, the IR beam was directed through the gas cell to monitor the powder sample as particles accumulated on the mesh filter. Intermediate spectra were recorded during the particle collection process to ensure that spectral changes were only due to increases in signal intensity resulting from particle accumulation on the mesh filter. Final spectra were recorded at 2 cm^{-1} resolution from 650 – 4000 cm^{-1} and averaged over 16 scans. When any spectrum baseline exhibited notable shift after particle collection, a linear background was subtracted from the entire spectrum. For the sake of clarity, individual spectra have been offset along the absorbance axis and truncated to the infrared regions from 820 to 950 cm^{-1} and from 2000 to 2150 cm^{-1}.

Particle surface composition was characterized in terms of SiH_x functionality by the integrated intensity ratio, $X = A_{def}/A_{str}$, where A_{def} is the area under absorption peaks between 800 and 950 cm^{-1}, and A_{str} is the area under absorption peaks between 2050 and 2150 cm^{-1}. The ratio can be taken as an approximate measure of the hydrogenated

surface composition since the region between ~800 and 950 cm^{-1} only exhibits absorptions associated with SiH_2, SiH_3, and other poly(silicon) hydrides, not with SiH. Differences in absorption cross sections were assumed to be negligible and independent of particle surface coverage.[5.17]

Particles for characterization by TEM were collected electrostatically onto lacey carbon coated copper grids attached to the end of a copper electrode. The electrode was inserted into the apparatus between the quartz tube reactor and the FTIR spectrometer, and negatively charged particles were collected by applying +300 VDC for ~10 seconds. After particles were collected, the plasma was shut off and residual gases and aerosol were evacuated from the apparatus. Two small valves were used to seal the particle-laden copper grids under vacuum during transport between instrumentation, but particles were still briefly exposed to air (generally < 2 minutes) while the sample was loaded into the microscope. In the TEM, an accelerating voltage of 300kV was employed. To minimize beam heating effects, relatively large spot sizes were used.

5.3 Results

Power

Figure 5.2 shows several representative FTIR spectra demonstrating how different power settings led to changes in the infrared signatures of particles synthesized in a 4 mm i.d. reactor. For these results, the gas flow ratios were 0/20/0, electrode spacing was 25 mm, reactor pressure was maintained at 4 Torr, and power was adjusted to several values between 11 and 46 W. Under this combination of settings, power levels greater than ~50 W caused the glow discharge to extend from the quartz reactor tube downstream into

electrically grounded stainless steel fittings. As indicated in Figure 5.2a, particles produced at less than ~20 W exhibited infrared spectra comprised of several broad peaks. With increasing power levels, sharper peaks evolved at ~2083, 2100, and 2137 cm^{-1} in the region associated with SiH_x stretching vibrations, and at 845, 858, 865, and 907 cm^{-1} in the region associated with SiH_x deformations. Figure 5.2b shows how the integrated intensity ratios varied with forward power. At the lowest power level, 11 W, the integrated intensity ratio was ~0.72. As the power level increased, the ratio passed through a minimum of ~0.35 at 26 W followed by a steady increase to ~0.5 at 46 W.

Representative TEM images of particles produced at 11, 30, and 40 W are shown in Figure 5.3. All other experimental parameters were the same as those used for the spectra presented in Figure 5.2. Particles produced at 11 W (Fig. 5.3a) exhibited highly irregular shapes. No lattice fringes suggestive of crystallinity were observed even at higher magnification. As power was increased, the particles became more spherical and particle crystallinity also improved as suggested by numerous particles exhibiting lattice fringes in Figures 5.3b and c.

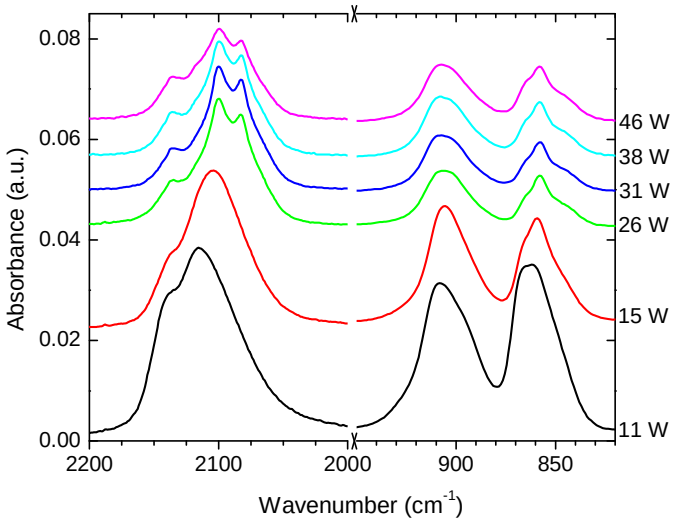

(a)

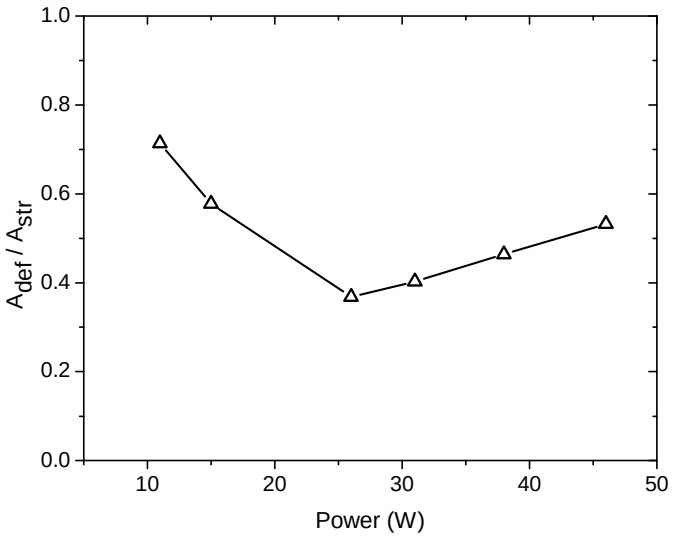

(b)

Figure 5.2. The effect of power on particle surface composition. (a) FTIR spectra showing the silicon-hydrogen stretching and deformation regions, with power levels indicated for each spectrum. (b) The corresponding integrated intensity ratios.

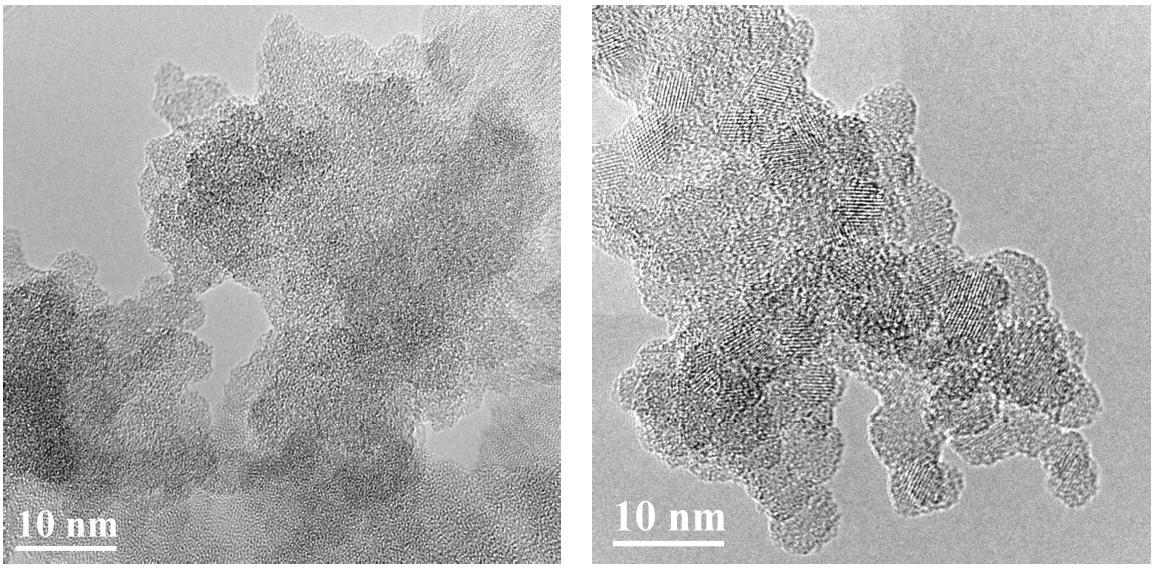

(a) (b)

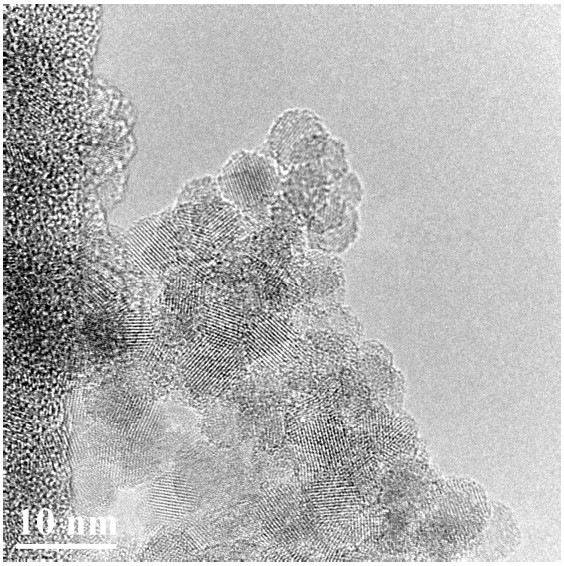

(c)

Figure 5.3. Representative TEM images showing the effect of forward power on structural morphology of particles produced at 0/20/0 flow ratios, 4 Torr, 4mm i.d. reactor tube, 25 mm electrode spacing and (a) 11 W, (b) 30 W, and (c) 40 W.

Hydrogen

Figure 5.4 shows how infrared signatures of particles change as molecular hydrogen is added to a 7 mm i.d. reactor tube at 17.5 Torr, 40 W power, 25 mm electrode spacing, and flow ratios of 400/10/*X*. Each spectrum exhibits broad absorptions with no sharp peaks. Adding hydrogen to the reactor under this set of conditions causes intensity reductions in peaks associated with higher silicon hydrides. For example, the intensity of the shoulder at ~2137 cm^{-1} in the SiH_x stretching region is noticeably reduced when 20 sccm H_2 is added to the precursor gas flows compared to spectra of particles synthesized at lower H_2 flow rates. The local maximum in the stretching vibration region also shifts from ~2112 cm^{-1} to ~2105 cm^{-1} as the H_2 flow rate is increased from 0 to 20 sccm. Peak intensities in the deformation region also decrease as the H_2 flow rate increases. As shown in Figure 5.4b, integrated intensity ratios decrease from ~0.8 when no molecular hydrogen is added to the precursor gas mixture to ~0.35 when 20 sccm H_2 is added to the precursor gas mixture.

Figure 5.5 shows TEM images of particles produced under the same conditions as those used to grow particles whose FTIR spectra are shown in Figure 5.4. When no molecular hydrogen was added to the reactor, numerous particles exhibited lattice fringes suggestive of crystalline particles (Fig. 5.5a). Adding hydrogen to the reactor elicited dramatic changes in the particle crystallinity. Figure 5.5b shows that by adding as little as 5 sccm H_2 to the reactor, lattice fringes were less abundant and primary particle size was slightly reduced. Particles also became less spherical as the H_2 flow rate was increased. When 10 sccm H_2 (Fig. 5.5c) or more was added to the reactor, the particle

shapes were highly irregular, discrete particles were difficult to discern, and particles exhibiting lattice fringes were not observed in any region of the TEM grid.

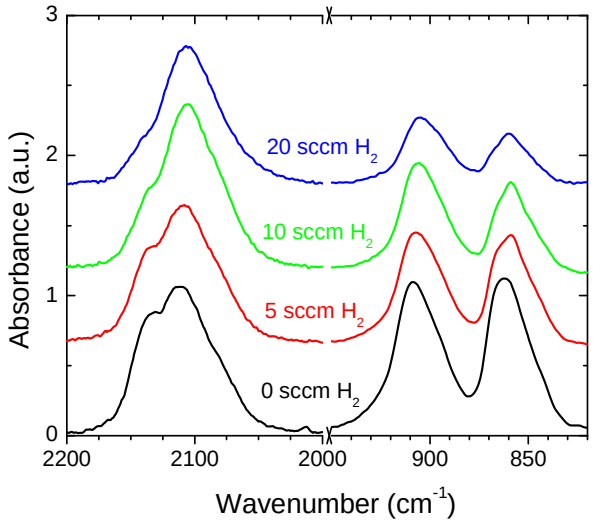

(a)

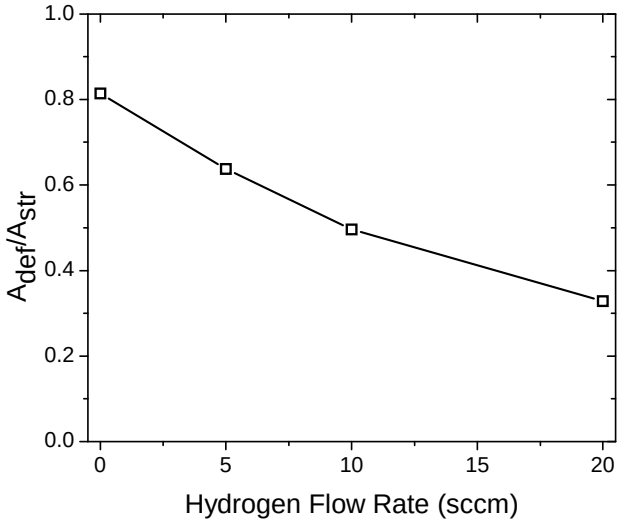

(b)

Figure 5.4. Effect of adding hydrogen to the plasma reactor at 400/10/X flow ratios, 50 W, 25 mm electrode spacing, 17.5 Torr reactor pressure, and a 7 mm i.d. tube reactor: (a) FTIR spectra, and (b) integrated intensity ratios.

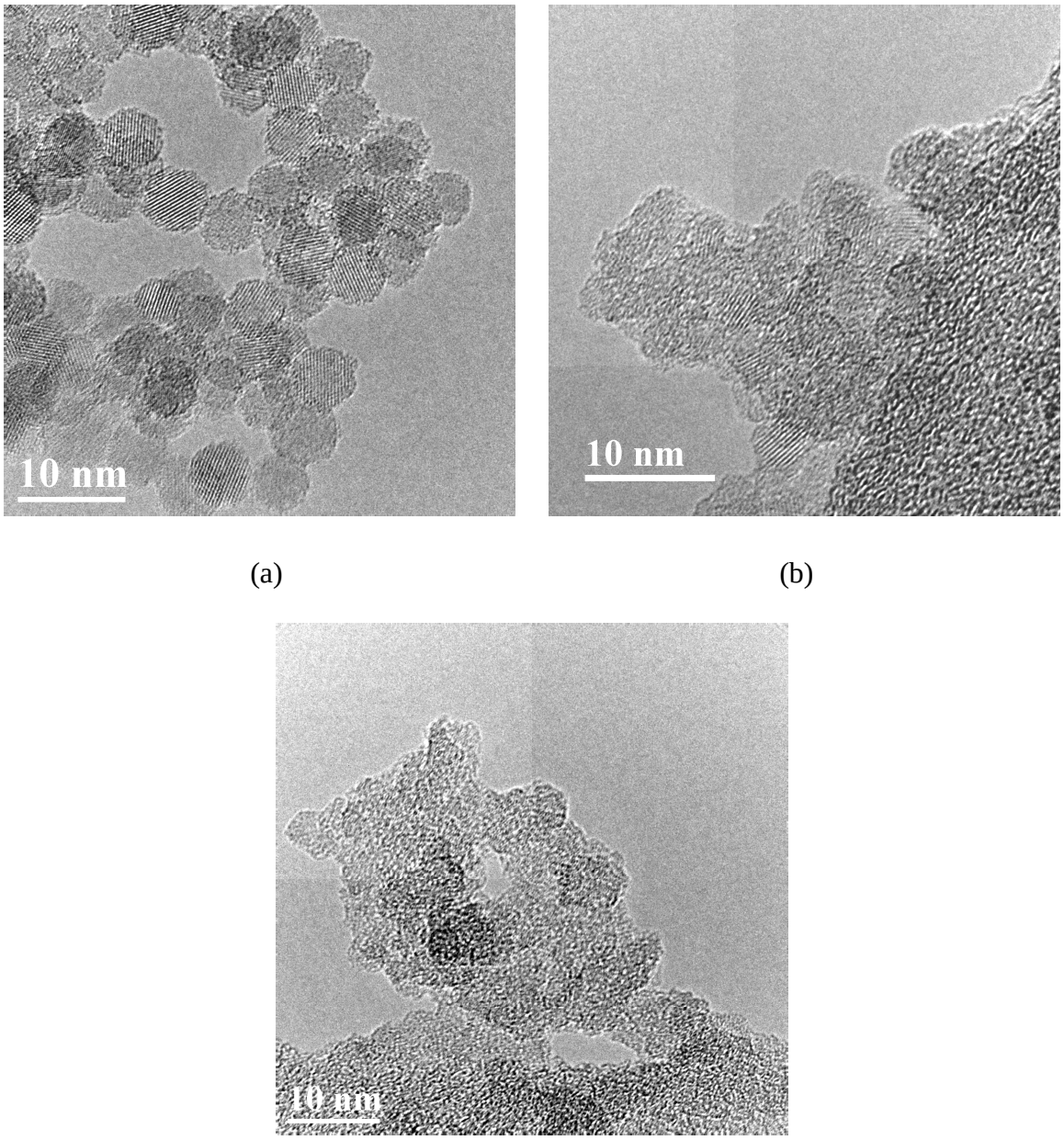

(a) (b)

(c)

Figure 5.5. Representative TEM images showing the effects on particle structural morphology when H_2 is added to the reactor in a 7 mm i.d. reactor tube at 50 W forward power, 25 mm electrode spacing, 17.5 Torr, and 400/10/x gas flow ratios with (a) 0 sccm H_2, (b) 5 sccm H_2, and (c) 10 sccm H_2.

Reactor Pressure

Effects of reactor pressure on particle surface silicon hydride composition are shown in Figure 5.6. Relevant experimental parameters for this set of experiments are: 100/25/0 flow ratios, 25 mm electrode spacing, 33 W, and 4 mm i.d. plasma reactor. Reactor pressure ranged from 7 to 15 Torr. The lowest pressure that was investigated was limited by conditions under which the glow discharge could be fully contained within the quartz tube reactor. For particles synthesized at 7 Torr, the dominant peak in the SiH_x stretching region occurred near 2100 cm^{-1}. In the deformation region of the same spectrum, two low intensity peaks also occurred at ~858 and 902 cm^{-1}. With increasing reactor pressure, additional peaks evolved in both the stretching and deformation regions. Integrated intensity ratios shown in Figure 5.6b steadily increased from ~0.1 to ~0.6 as the pressure was raised from 7 to 15 Torr.

Figure 5.7 shows TEM images of particles produced under the same conditions as those in Figure 5.6. Particles were collected at 7 Torr (Fig. 5.7a) and 15 Torr (Fig. 5.7b). Particles are essentially spherical in both images, and a high level of crystallinity is suggested by the many particles that exhibit lattice fringes. The images also show that particle sizes change with reactor pressure. Particles produced at 7 Torr are generally smaller than those produced at 15 Torr.

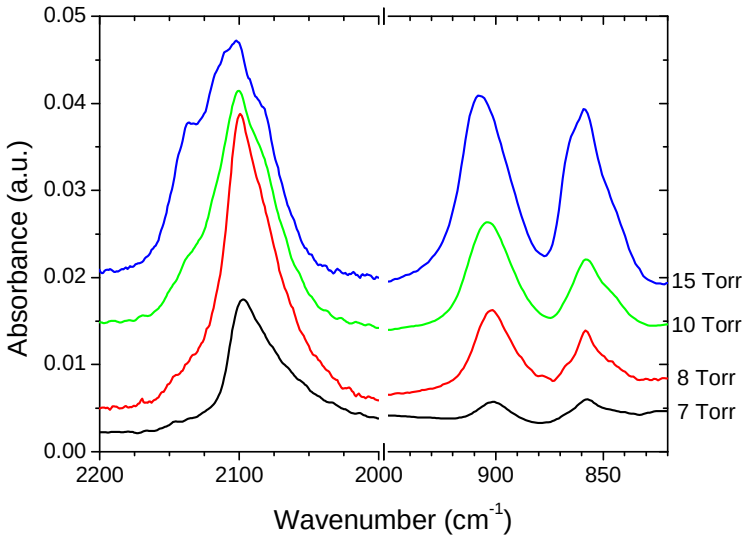

(a)

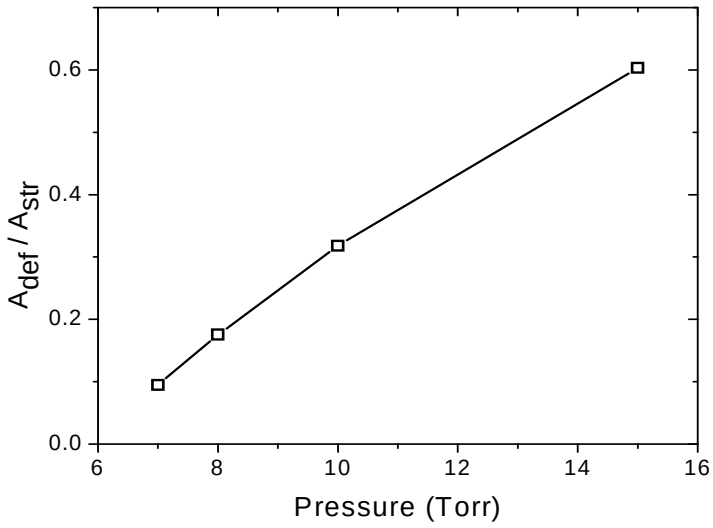

(b)

Figure 5.6. Effect of reactor pressure on the surface silicon hydride composition of particles produced in a 4 mm i.d. reactor tube: (a) FTIR spectra, and (b) the corresponding integrated intensity ratios.

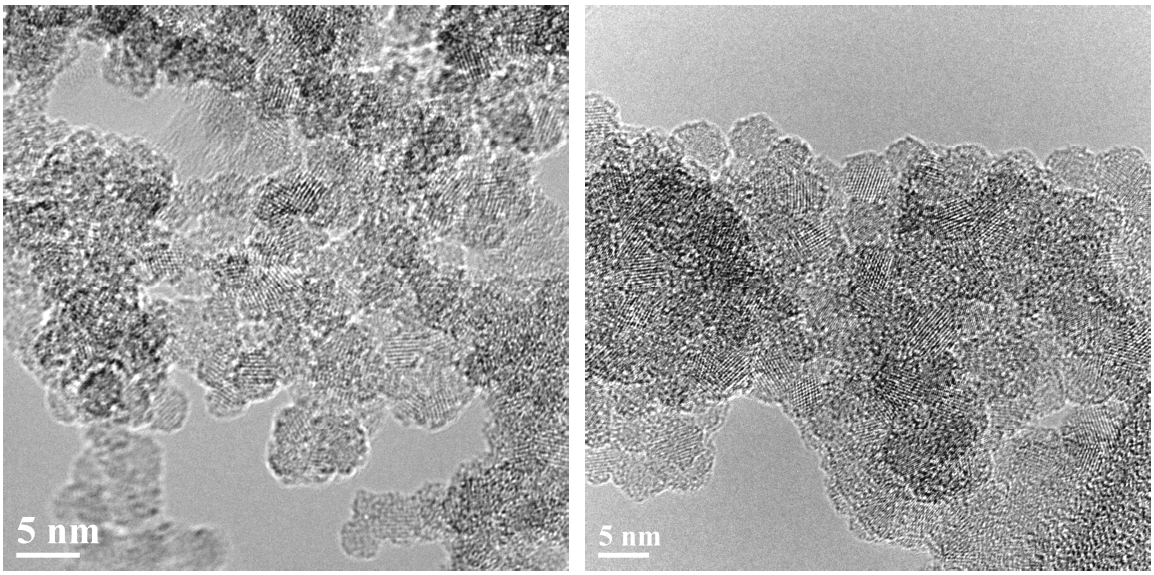

(a) (b)

Figure 5.7. Representative TEM images of particles produced in the 4mm i.d. reactor at 100/25/0 flow ratios, ~33 W, 25 mm electrode spacing, and (a) 7 Torr, (b) 15 Torr.

5.4 Discussion

Power

Under the conditions described here, power has effects on both particle surface composition and structural morphology. The images in Figure 5.3 suggest that crystalline particles can be synthesized at power levels between ~30 and 50 W. Lower power levels produce amorphous particles under these conditions. Although the experimental parameters are slightly different, the power required to produce crystalline particles is similar to that reported previously.[5.3] In that report, Kortshagen and co-workers proposed that a temperature disparity between particles and the surrounding carrier gas was one of the factors responsible for the formation of nanocrystals rather than amorphous nanoparticles. In essence, electron and ion recombination at particle surfaces and the

energy released upon formation of Si–Si bonds contributed to particle heating well above the local gas temperature. Their simulations suggested that small (3nm diameter) particles could experience brief temperature excursions up to ~900 K, several hundred Kelvin above the surrounding gas temperature, while larger particles (10 nm diameter) remained closer in temperature to the surrounding carrier gas. Due to the size-dependent particle melting temperature phenomenon,[5.18] or perhaps a softening of the silicon covalent bonding network due to plasma annealing effects,[5.19] sufficiently small particles heated in the plasma could be in a non-crystalline state. The rapid temperature fluctuations and the accompanying restructuring and relaxation of strained Si–Si bonds would promote the formation of spherical, crystalline particles. According to this hypothesis, 'melting', whether induced thermally or non-thermally presumably occurs at some minimum power level. Under the conditions used here, and for many other combinations of control settings examined for this report, the minimum power level sufficient to elicit crystalline particles was between 20 and 30 W.

Power also appears to influence the particle surface composition in terms of silicon-hydrogen functional groups. The integrated intensity ratios shown in Figure 5.2b exhibit a minimum of ~0.4 at 26 W, suggesting that at this power the population of monohydride functional groups is greater than the population of other surface functional groups comprised of silicon and hydrogen. At 26 W the spectrum in Figure 5.2a also exhibits sharper features than spectra of particles produced at lower power. For example, three distinct peaks appear in the silicon-hydrogen stretching region near 2083 cm^{-1} (SiH), 2100 cm^{-1} (SiH), and 2137 cm^{-1} (SiH_3). Absorption peaks at these locations have been attributed to SiH on strain–free Si(111),[5.20] SiH on highly strained Si(100) 2×1,[5.21]

and SiH_3 on other crystalline silicon substrates including porous silicon.[5.22] The accompanying TEM images do not show evidence of particle surface facets lending support to these peak assignments, and therefore the assignments can only be empirical at best. However, if the particles do experience brief temperature excursions up to 900 K (or possibly greater temperatures for particles smaller than 3 nm in diameter) infrared signatures characteristic of higher hydrides such as SiH_2 or SiH_3 should not exhibit significant intensities since hydrogen desorption from these functional groups should occur.[5.23] If hydrogen desorption from higher order hydrides does indeed occur, then in addition to heating/annealing effects, the resulting unsatisfied silicon bonds at the particle surfaces could induce further restructuring to more energetically stable structural configurations (for example, lower concentrations of unsatisfied bonds, strain-free Si–Si bonds and/or SiH functional groups).[5.22] Persistent SiH (monohydride) functional groups could contribute to the intensity of either the peak at 2100 cm^{-1} or the peak at 2083 cm^{-1} depending on whether or not relaxation of the local structure occurred. Note that this hydrogen desorption hypothesis does not account for higher hydrides on particle surfaces.

Hydrogen

Adding molecular hydrogen to the plasma reactor appears to have significant effects on both the chemical and structural morphology of particles. As Figure 5.5a shows, when no H_2 is added to the reactor under the outlined set of experimental conditions, particles are spherical and crystalline. Individual particles are easily distinguished. Adding as little as 5 sccm H_2, however, severely hinders particle crystallinity, and individual particles become much more difficult to discern (Fig. 5.5b).

Hydrogen can etch silicon[5.24] and could be partially responsible for the crystallinity loss. However, if the sole effect of adding hydrogen to the precursor gases is to etch the particles, one might expect to observe only a reduction in particle size. The images in Figure 5.5b and c do not clearly show evidence of reduced particle size. But they do show that under these conditions, increasing the H_2 flow rate causes particles to exhibit increasing fractions of disordered material.

Adding hydrogen to the plasma reactor also influences the silicon-hydrogen functionality imparted to the particles. As shown in Figure 5.4, spectral features are broad, and absorption bands at higher wavenumbers in the SiH_x stretching region decrease with increasing H_2 flow rate. When H_2 is added as a precursor gas, the concentration of hydrogen atoms and ions formed in the plasma probably also increases. The increased concentration of hydrogen atoms and ions could partially account for the decreased absorption intensities of higher hydrides because the hydrogen could satisfy dangling bonds of molecular fragments or clusters thought to be precursor components of larger particles. Although not shown here, a sharp absorption at 2188 cm^{-1} (a signature of SiH_4) was occasionally observed in FTIR spectra recorded during the particle collection process when H_2 was incorporated as a precursor gas. As demonstrated computationally,[5.6] fully hydrogen-passivated precursor components of larger particles would also inhibit particle growth because the hydrogen adlayer provides a large activation barrier to cluster/particle sintering and coalescence during gas phase particle growth processes, whereas bare silicon cluster/particle surfaces would require little, if any, activation for reactive collision. In contrast to nano-crystalline silicon films which are generally fabricated from silane heavily diluted by H_2,[5.25] it appears that adding only

small amounts of H_2 to the nontraditional reactor employed here can severely impede nanocrystal formation.

In another report,[5.8] Kortshagen and co-workers examined photoluminescence quantum yields of silicon nanoparticles synthesized under slightly different hydrogen partial pressures. When less H_2 was added to their plasma reactor, their particles exhibited better quantum yields and longer emission wavelengths. They hypothesized that the longer wavelengths were due to larger particles, but no size analysis was presented. Based on the results observed here, the wavelength differences observed by Kortshagen et al. could be due to at least two complementary effects. First, as they increased H_2 flow rates, they also increased argon flow rates. Although the hydrogen flow rates were only changed from 1 to 4 sccm, the accompanying argon flow rates were increased from 60 to 110 sccm. Greater precursor gas flow rates would almost certainly reduce the particle residence time in the plasma reactor, thereby reducing particle size. This would partially account for lower emission wavelengths. Second, hydrogen could also participate as a particle etchant and/or combine with other reactive species in the plasma thereby hindering particle growth. Neither of these effects are especially satisfying explanations of the dramatic drops in quantum efficiency when particles were synthesized with increasing hydrogen flow rates. However, note that the particles in Figure 5.5b appear strikingly similar to those presented in that report.[5.8] Neither images show particularly well-formed, spherical nanocrystals like those of Figure 5.5a, which were synthesized without adding H_2 to the plasma reactor. Figure 5.5 clearly shows that adding H_2 to the plasma reactor reduces particle crystallinity under the outlined

conditions. As such, the poorly formed particles probably exhibit numerous defects that can reduce desirable photoluminescent characteristics.

Reactor Pressure

Assuming other parameters are appropriately adjusted, reactor pressure can also be used to control particle size (and perhaps incidentally, the surface hydride composition) while still promoting formation of crystalline particles. Particle size changes are demonstrated in Figure 5.7 where both images show many particles in an appropriate orientation to exhibit lattice fringes. Single-crystalline particles are widespread in both samples. At 7 Torr the primary particle size appears smaller than 5 nm in diameter. The particles produced at 15 Torr presumably experience a greater residence time within the reactor and are consequently larger than 5 nm in diameter.

In addition to particle size changes, reactor pressure also appears to influence the surface hydride composition as suggested by Figure 5.6. Under these circumstances, changing the reactor pressure elicits remarkable changes in the particle surface hydrides. For example, the integrated intensity ratios of particles synthesized in the 4 mm i.d. reactor varied from less than 0.1 at 7 Torr to ~0.6 at 15 Torr (Figure 5.6b). At 7 Torr the majority of the functional groups at particle surfaces are attributed to SiH groups. The asymmetric peak at 2100 cm^{-1} is likely due to a superposition of absorptions from SiH groups in different structural environments that could be expected of spheroidal particles. At 15 Torr, particle surface hydrides are more diverse as suggested by the increasing intensities of peaks due to higher hydrides. Of the parameter settings examined for this report, the 4 mm i.d. tube most readily produced particles with the lowest integrated

intensity ratios, and therefore the greatest number of monohydride functional groups. In regard to particle surface tailoring, this could be considered a rational *starting* point for optimizing particle synthesis conditions for post-synthesis tailoring by hydrosilylation since the particles exhibit good crystallinity, they are sufficiently small to exhibit quantum confinement effects, and the surface composition is better attuned to the proposed hydrosilylation reaction mechanism.[5.9]

That larger particles exhibit more complex surface compositions than smaller particles is something that deserves further consideration. Why should smaller particles synthesized at 7 Torr in the 4 mm reactor exhibit lower concentrations of higher hydrides than larger particles synthesized at 15 Torr? The most obvious explanation is that larger particles have more surface atoms than smaller particles. As such, the larger particles could exhibit a greater number and diversity of structural environments for various bonding configurations and functional groups. Alternatively, smaller particles may be in a more highly strained state than larger particles due to curvature effects, and the smaller particles may therefore not be able to retain higher hydride functional groups. Or as mentioned above, smaller particles are probably heated in the plasma reactor to temperatures sufficient to drive away higher hydrides, but larger particles are not. Somehow though, even larger particles must be sufficiently heated to induce formation of single-crystalline structures, since single-crystalline particles 20 nm in diameter and larger can be synthesized at similar power levels as shown in Figure 5.8. Additionally, at lower reactor pressures there would be fewer collisional cooling events than at higher reactor pressures. This would allow the particles to remain at temperatures above the local gas temperature for longer times, increase the probability of hydrogen desorption,

and reduce the probability of collision between a nascent cluster/particle and other reactive species. Incidentally, when all other parameters are held constant, the glow discharge extends further upstream and downstream from the electrodes when reactor pressures are reduced. At lower pressures then, the particles could experience a longer residence time in the glow discharge.

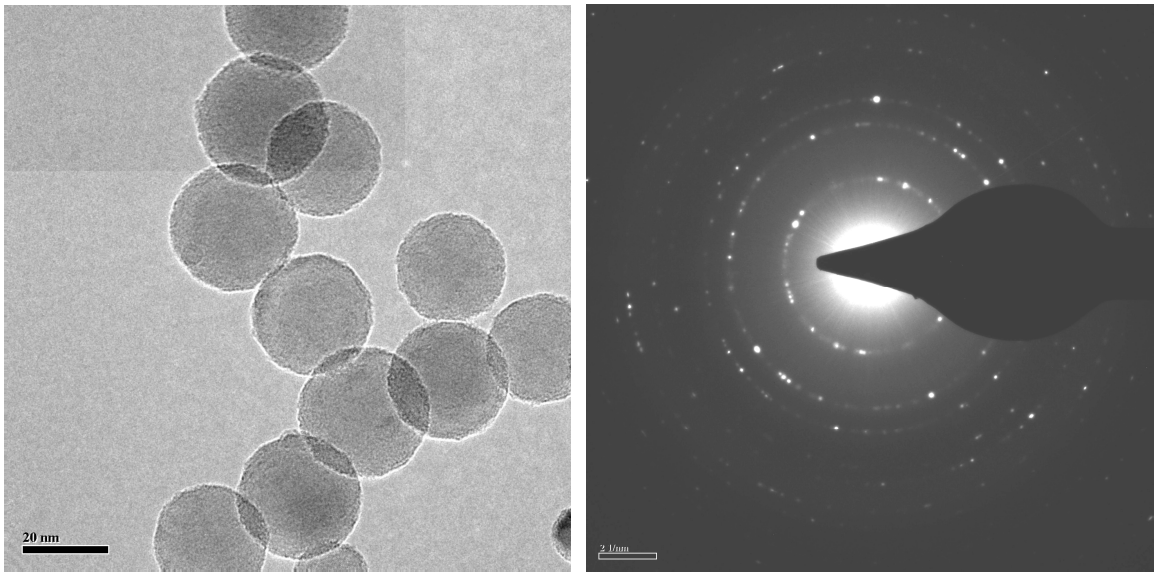

(a) (b)

Figure 5.8. Particles produced in a 25 mm o.d. reactor tube at 30 W, 200/50/0 gas flow ratios, 7 Torr, and 25 mm electrode spacing. (a) A bright field image showing several large spherical particles. (b) The corresponding selected area diffraction pattern. Images were recorded using and FEI Technai T-12 TEM operating at 120 kV.

Another point that deserves further consideration is that higher hydrides were observed in most of the infrared spectra recorded for this report. However, the hypotheses of heating, hydrogen desorption, and restructuring does not necessarily

account for their presence. Where then do the particles acquire those surface functionalities? In a continuous flow plasma of the cylindrical geometry considered here, atoms, ions, electrons, molecular fragments, clusters and other species are all probably continuously passing through the plasma reactor with the flow. Although notable particle heating events can occur in the plasma, the particles must also pass through boundary layers as they emerge from the reactor. This is one place where particles could pick up various silicon-hydrogen functionalities. Does this mean that infrared spectra should be interpreted as signatures of the nonequilibrium end growth stages as the particles leave the plasma? If so, this would imply that to tailor the particle surface hydrides using the plasma reactor, one would have to exert order on the morass of stuff flowing out of the reactor. In the smallest tube (4 mm i.d.) at the lowest pressure (7 Torr) (and the longest length glow discharge), perhaps some components of the heterogeneous mixture of ions, fragments, and clusters have sufficient time to diffuse and stick to the quartz tube reactor walls and thus do not exit with the carrier gas flow for subsequent adsorption at particle surfaces. This hypothesis could partially account for the dominant monohydride functionality observed at 7 Torr in Figure 5.6. If the composition of matter exiting the plasma reactor with the particles could be reasonably estimated, computational investigation of the end growth stages could potentially provide insight into better ways to control the surface composition as particles exit the reactor.

Lastly, the relationship between infrared spectra and particle crystallinity is considered. From some of the results presented here (Figs. 5.2 and 5.3), one could infer that particle crystallinity improves as the infrared signatures of particles become sharper and exhibit absorptions at locations coincident with those of well characterized

crystalline surfaces. However, sharp infrared absorption peaks at locations coincident with those observed on extended crystalline Si surfaces do not necessarily correlate with particle crystallinity. For example, the infrared spectrum corresponding to 11W in Figure 5.2a and the spectrum corresponding to 0 sccm H_2 in Figure 5.4a appear quite similar. The integrated intensity ratios also exhibit comparable values. However, the representative TEM images suggest that the particles can be either amorphous (Fig 5.3a) or crystalline (Fig 5.5a). Without question, infrared spectroscopy is the optimal technique to characterize silicon hydride functional groups on silicon surfaces. But, infrared spectra cannot *a priori* be correlated with particle crystallinity, especially for the nanoparticle samples considered here. Crystallinity must be demonstrated via complementary techniques such as X-ray diffraction, Raman spectroscopy, or electron microscopy.

5.5 Conclusions

Hydrogen-terminated silicon nanoparticles can be synthesized over a broad range of operating parameters in a continuous flow, non-thermal RF plasma. Particle sizes, the surface composition, and the crystallinity can all be modified under the appropriate conditions. Under some conditions, the particle surface compositions can be manipulated such that they are more amenable to post-synthesis modification by hydrosilylation (e.g., predominant monohydride coverage) while still exhibiting crystallinity. Possible explanations for different silicon-hydride functionality were also presented. Although it is important to consider reactions occurring at particle surfaces within the plasma, reactions occurring downstream from the plasma may also play an important role in the

final particle surface chemistry, especially in the continuous-flow reactor used in these experiments.

Chapter 6.

Sintering, Coalescence, and Compositional Changes of Hydrogen-Terminated Silicon Nanoparticles as a Function of Temperature

Sintering, coalescence, and compositional changes of hydrogen-terminated, crystalline silicon nanoparticles were examined as a function of temperature. Monodisperse aerosol particles ~5 nm in diameter were synthesized by gas-to-particle conversion in a plasma reactor and then immediately heated as they flowed through a tube furnace. Particles were also collected as powders and then heated in other apparatuses. Structure and size changes were characterized by X-ray diffraction (XRD) and transmission electron microscopy (TEM), thermal behavior was characterized by differential scanning calorimetry (DSC), and silicon-hydrogen functionality changes were characterized by Fourier transform infrared spectroscopy (FTIR). At ~500 °C, only silicon monohydride functional groups are observed in FTIR spectra. XRD results obtained after heating particles to that temperature indicate a small reduction in crystal size relative to the freshly generated particles, and TEM images show disorganized particle shells surrounding crystalline particle cores. Between 550 and 750 °C extensive sintering occurs and polycrystalline aggregates evolve. At temperatures greater than ~750 °C, no silicon hydrides are observed in FTIR spectra, and extensive coalescence occurs. Temperatures of 1000 °C are required to produce completely coalesced single-

crystalline, spherical particles. Exothermic behavior is exhibited up to 1000 °C with two conspicuous exothermic transitions centered at ~350 °C and 750 °C. The transitions correlate well with desorption of higher hydrides from particle surfaces and coalescence of particle agglomerates, respectively.

6.1 Introduction

Sintering and coalescence are two terms frequently used to describe the behavior of particles when they are heated to sufficiently high temperatures. For silicon particles, sintering temperatures are generally between 0.75 T_m and 0.98 T_m, where T_m is the bulk silicon melting temperature.[6.1] The elevated temperature is maintained until the particles bond together and form a larger, partially fused mass. Coalescence is a process in which particle agglomerates evolve from irregular or fractal shapes to more monolithic, spherical shapes.

Numerous particle synthesis processes and nanoparticle device applications rely upon sintering and coalescence. For example, gas-to-particle conversion processes in aerosol reactors depend on controllable sintering and coalescence of molecular fragments and clusters to produce particles with characteristics such as crystallinity and size monodispersity. Nanoparticles are also being considered for use in the controlled fabrication of polycrystalline thin films and other nanostructured devices. For example, deposition of nanoparticle building blocks into patterned thin films is of interest for various electronics applications.[6.2,6.3] In these devices, deposited nanoparticles are heated until the particles reorganize into compact, polycrystalline structures. One potential benefit of using nanoparticles in these devices is the reduced temperature at which the particles melt compared to the bulk melting temperature.

Optimal particle synthesis and device development both require a comprehensive understanding of the heating effects on the nanoparticle/nanostructure precursors. Naturally, sintering and coalescence have been well studied both experimentally and computationally, and many mathematical models have been developed to represent the

relevant phenomena. Parameters frequently incorporated into aerosol-based models include, but are not limited to, particle size distribution,[6.4] fractal dimension,[6.5] viscous diffusion,[6.6] solid state diffusion,[6.7] surface tension,[6.8] surface area,[6.9] accessible surface area,[6.10] melting temperature,[6.11,6.12] time,[6.13] and temperature.[6.14] Because some of the parameters also exhibit size-dependent behavior, accurate and comprehensive models describing nanoparticle sintering and coalescence are often incomplete and almost always complex. Another important but less frequently considered parameter relevant to nanoparticle sintering and coalescence is particle surface composition. Both computational and experimental studies have shown that a passivating layer, or a less reactive outer shell at particle surfaces, can hinder sintering and coalescence.[6.8,6.15-6.17] However, the effects of the particle surfaces are still not well understood, and rarely are they incorporated into simulations and mathematical models. To that end, silicon nanoparticles synthesized from silane in a non-thermal RF plasma are good candidates for examining how the particle surface chemistry can influence sintering and coalescence of covalently bonded systems. Notable quantities of size monodisperse, single-crystalline silicon nanoparticles can be produced using this technique.[6.8] The particles are also inherently hydrogen-terminated, and as such, the hydrogen adlayer impedes interparticle reaction and other unwanted reactions such as oxidation.

In this chapter, sintering and coalescence of hydrogen-terminated, crystalline silicon nanoparticles are examined. The particles, initially ~5 nm in diameter, are heated in several apparatuses, and the effects of surface hydrogen on sintering and coalescence are considered. Infrared spectroscopy, transmission electron microscopy, X-ray diffraction, and differential scanning calorimetry are employed to examine structural,

compositional, and thermal changes that occur as the particles are heated. As will be shown, hydrogen persists at particle surfaces to temperatures well above the experimentally reported melting point of 5 nm diameter silicon particles (~580 °C),[6.2] and therefore the hydrogen almost certainly influences sintering and coalescence over the time scales of the experiments reported here.

6.2 Experimental

Hydrogen-terminated silicon nanoparticles were synthesized by gas-to-particle conversion in a continuous flow non-thermal RF plasma reactor.[6.18] As described previously, 50 sccm of a mixture of 0.5% SiH_4 in argon and an additional 100 sccm argon were introduced into a 7 mm i.d., 20 cm long quartz tube reactor. Power, ~40 W at 13.56 MHz, was coupled to the reactor through two ring electrodes separated by 25 mm as shown in Figure 6.1. Reactor pressure was measured immediately upstream of the quartz tube and maintained at 7 Torr with a mechanical vacuum pump (Leybold, Model D90AC). Under these conditions the plasma glow discharge was completely contained within the quartz tube.

Nanoparticles were either heated 'in flight' in aerosol form or *ex situ* in powder form. In flight heating occurred as the aerosol-synthesized particles flowed from the plasma reactor through a 10.9 mm i.d. stainless steel flow tube (Inconel 600) located in a single zone tube furnace (Lindberg/Blue, Model HTF 55122A). Temperature settings for the in flight heating experiments ranged from 23 to 1000 °C. Representative temperature profiles along the centerline of the flow tube, several of which are shown in Figure 6.2, were measured as previously described.[6.19]

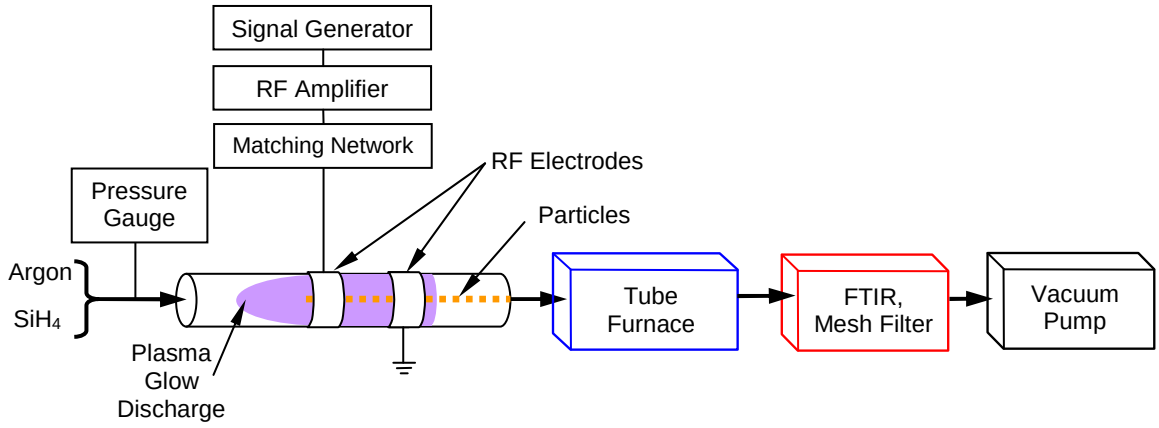

Figure 6.1. A schematic of the particle synthesis apparatus.

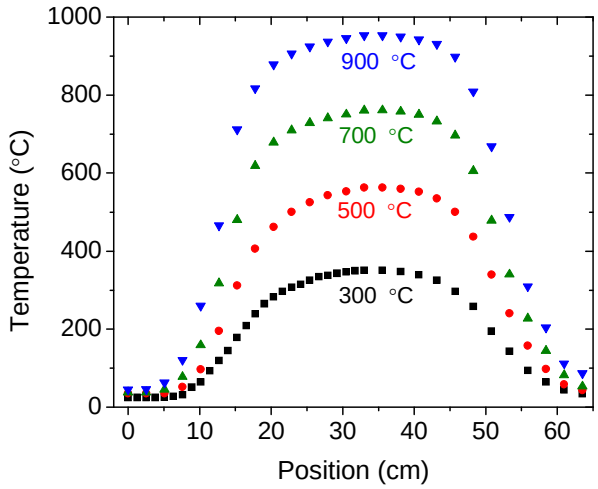

Figure 6.2. Representative temperature profiles along the centerline of the stainless steel flow tube.

A hybrid flow through gas cell located in the analysis chamber of an FTIR spectrometer (Nicolet Magna-IR Model 550, Madison, WI) was used to examine how silicon hydride functional groups at particle surfaces changed with heating.[6.19] Within the gas cell, a piece of fine stainless steel mesh was used as a filter to collect particles while aerosol from the plasma reactor flowed through the apparatus. After enough powder had

collected on the filter to produce an acceptable signal-to-noise ratio, *in situ* spectra were recorded in transmission mode at 2 cm^{-1} resolution from 650 to 4000 cm^{-1} and averaged over 16 scans. With the exception of the spectrum recorded of particles heated to 700 °C, fewer than 2 minutes were required to collect sufficient powder for the spectra of Figure 6.3. At temperatures of 700 °C and higher, particles were collected for at least 10 minutes before spectra were recorded.

Particle size changes were characterized in part by two X-ray diffractometers. One diffractometer, a Bruker-AXS D-5005 (Cu K_α X-rays), was used to examine particles that had been heated in flight as they flowed through the tube furnace with the reactor pressure held at 7 Torr. For these measurements, particles were heated to different temperature settings between room temperature and 1000 °C and then collected on mesh filters located sufficiently downstream from the furnace such that the gas/aerosol had cooled back to room temperature. Clean filters were used to collect particles at each temperature set point. Powder was scraped from the filters onto clean amorphous substrates, and the Si(111) diffraction peak of each sample was recorded.

The other X-ray diffractometer, a Scintag XDS (Cu K_α X-rays) equipped with a water-cooled heating stage, was used to characterize particles heated on a substrate at atmospheric pressure. This additional X-ray characterization was performed in part to compare particles heated in flight to particles heated in powder form on a substrate. For these measurements powder samples were collected on stainless steel mesh filters, and the particles were not heated as they flowed through the tube furnace. Collected powder was scraped from the filters and placed directly onto a resistively heated platinum substrate within the heating stage. Prior to heating, the stage was flushed with dry

nitrogen for 10 minutes at room temperature. Thereafter, the heating stage was continuously flushed with nitrogen during the entire heating/cooling procedure to minimize oxidation. (Without the continuous nitrogen flush, diffractograms did not exhibit peaks after particles were heated to the highest temperatures.) After the initial nitrogen flush, the powder samples were heated at 50 K/min to temperatures from 300 to 1000 °C. Once the heating stage substrate reached the desired temperature set point, the temperature was maintained for 1 minute. The sample was then allowed to cool back to room temperature as rapidly as the cooling water would allow, and the Si(111) diffraction peak was subsequently recorded. Fresh, previously unheated powder samples were used for each temperature set point. MDI Jade software was used to determine the full width at half maximum (FWHM) of the Si(111) diffraction peaks generated by both X-ray diffractometers. Corrections for instrumental broadening effects were not made.

Differential scanning calorimetry (Netzsch, Model STA 409 PC) was used to characterize thermal transitions occurring within the powder samples during heating. For these measurements, particles were collected on stainless steel mesh filters without being heated in the tube furnace. Powder was scraped from the filters and then either firmly compressed or loosely placed into covered platinum crucibles. Prior to heating, ambient air in the calorimeter furnace chamber was evacuated with a mechanical vacuum pump. The chamber was then repressurized to atmospheric pressure with dry nitrogen and thereafter continuously flushed with dry nitrogen during heating. The heating program consisted of a 25 K/min ramp to 1000 °C. Powder sample masses for these measurements were between 5 and 10 mg.

Particles for characterization by transmission electron microscopy (FEI Technai G^2 F30) were heated in flight in aerosol form as they flowed through the tube furnace. At several temperature set points, particles were collected electrostatically (+300 VDC) on lacey carbon coated copper support grids located sufficiently downstream from the tube furnace such that the aerosol had cooled back to room temperature. Samples were sealed in the low pressure environment, immediately transported to the microscope in secondary containers filled with nitrogen or argon, and then characterized at 300 kV accelerating voltage.

6.3 Results

Figure 6.3 shows FTIR spectra recorded of particles heated to different temperature set points. For these spectra, particles were heated in flight as they flowed through the tube furnace. After heating to temperatures below 450 °C, several absorptions are observed between 820 and 950 cm^{-1}, and between 2050 and 2150 cm^{-1}. Absorptions in these two regions are due to silicon-hydrogen deformation and stretching modes, respectively. At 450 °C, absorption intensities in the deformation region are much less intense than those observed of particles heated at lower temperatures, and two distinct peaks evolve in the silicon-hydrogen stretching vibration region. One peak appears at 2083.7 cm^{-1} and the other at 2101.1 cm^{-1}. Note that the peak at ~2083 cm^{-1} is asymmetric on the low wavenumber side. At temperatures of 500 °C and higher, no absorptions occur in the deformation region. The peaks near 2083 and 2100 cm^{-1} persist up to ~650 °C, both exhibit small shifts to lower wavenumbers with increasing temperature as shown in Figure 6.3b, and the intensity of the peak at 2100 cm^{-1} attenuates

more rapidly than the peak at 2083 cm^{-1} with increasing temperatures. At 700 °C, infrared absorptions are minimal. Note that for the spectrum recorded of particles heated to 700 °C the particle collection time was ~5× longer than collection times for spectra recorded of particles heated at lower temperatures.

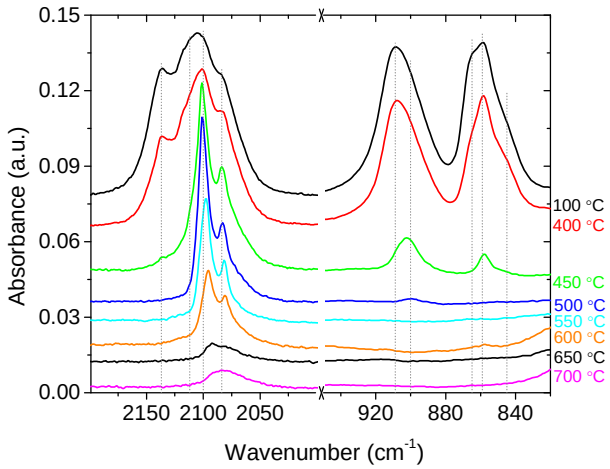

(a)

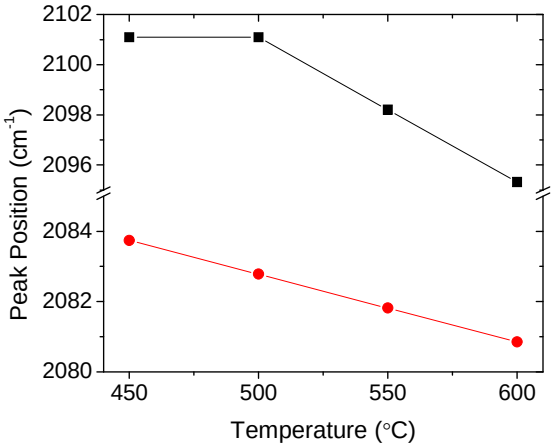

(b)

Figure 6.3. Infrared absorption spectra recorded of particles that were heated in flight as they flowed through the tube furnace. (a) Individual spectra corresponding to several furnace temperature settings. (b) SiH stretching peak positions as a function of temperature.

Figure 6.4 shows how the sum of the areas under the silicon-hydrogen deformation peaks (820–950 cm^{-1}) and stretching peaks (2000–2200 cm^{-1}) changed as a function of temperature. Data presented in this manner can provide qualitative information on hydrogen coverage, and thus, results must be interpreted with caution. First, the implicit assumption is that the particles synthesized in the plasma are completely covered with hydrogen. In fact, electron paramagnetic resonance measurements suggest that unpaired electrons are present in fresh, unheated powder samples as shown in Figure 6.5. Second, differences in absorption cross sections were assumed to be negligible and independent of particle surface coverage. Third, it is not possible to prove that the silicon particles were consistently dispersed across the mesh filter for each infrared spectrum. Although particles were collected in the same apparatus for similar durations at each heating temperature, it is probably the case that the amount of powder interacting with the infrared beam was slightly different at each temperature setting. Because the absorption intensity is proportional to the amount of mass, a rigorous comparison of integrated intensities is not possible. With these caveats in mind, Figure 3 suggests that near 500 ºC, particles exhibit roughly 20% of the hydrogen coverage exhibited by unheated particles.

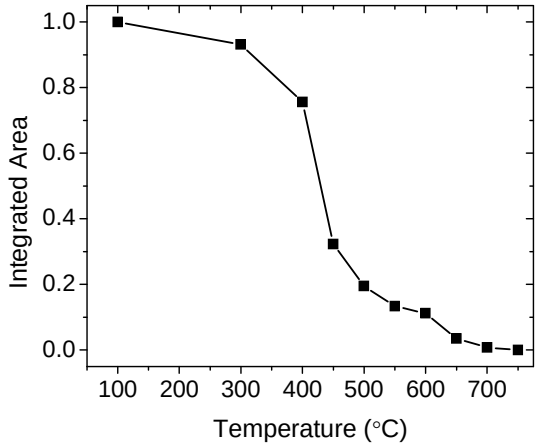

Figure 6.4. Sum of the integrated areas of the SiH stretching (2000-2200 cm^{-1}) and deformation (820-950 cm^{-1}) regions for several heating temperatures. Integrated areas were normalized with respect to room temperature data.

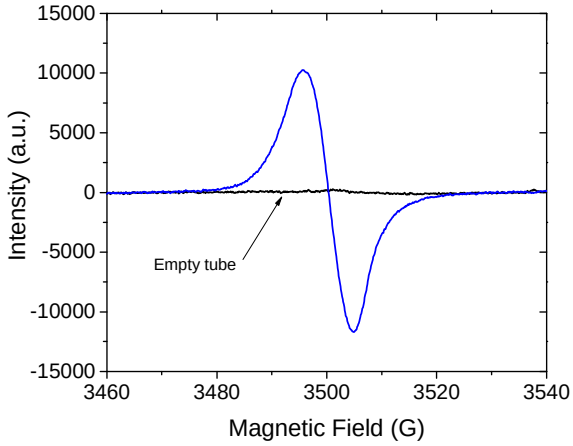

Figure 6.5. Electron paramagnetic resonance spectrum of fresh, unheated particles. Particles were collected on steel mesh and scraped into a 5mm diameter NMR tube for spin characterization.

Figure 6.6 summarizes the X-ray diffraction results. The FWHM of each Si(111) diffraction peak and the corresponding equivalent crystallite size based on the Scherrer equation[6.20] are shown as a function of temperature. Data are shown for particles heated in flight as they flowed through the tube furnace (black markers) and for particles heated in powder form in the X-ray diffractometer heating stage (red markers). Data recorded of unheated particles with both X-ray diffractometers are consistent with ~5 nm diameter nanocrystals. Near 500 °C, both diffractometers indicate a small increase in the FWHM of Si(111) peaks. At temperatures greater than ~500 °C, both diffractometers indicate decreasing FWHM values. Figure 6.6 also shows that the general trends in diffraction behavior are similar for both heating techniques over the range of temperature set points. Therefore, a meaningful correlation can be made between results obtained of particles that were heated in powder form and results obtained of particles that were heated in flight as they flowed through the tube furnace.

Thermal transitions characterized by DSC are shown in Figure 6.7. The black curve represents powder loosely placed in the crucible, and the red curve represents powder firmly packed in the crucible. Exothermic behavior is exhibited by both samples over the entire temperature range, and two distinct peaks appear in both traces. The first peak occurs near 350 °C and is fairly broad. The second peak occurs near 750 °C. Exothermic behavior is similar for both samples, and around 500 °C both traces exhibit a notable decrease in heat release compared to temperatures on either side of 500 °C. At 750 °C the powder loosely placed in the crucible shows a sharper peak than the powder firmly compacted in the crucible. An abrupt drop also appears near 785 °C in both curves. The drop is reproducible, and was observed in many experiments.

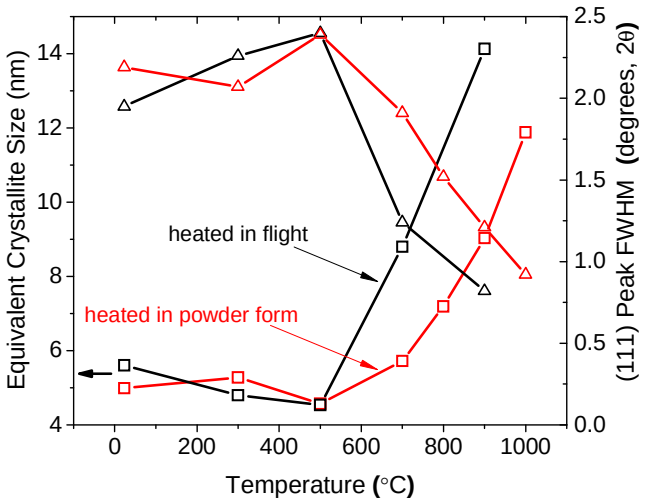

Figure 6.6. Summary of the XRD results. The FWHM of Si(111) diffraction peaks from both heating techniques and the corresponding equivalent crystallite sizes are shown as a function of temperature.

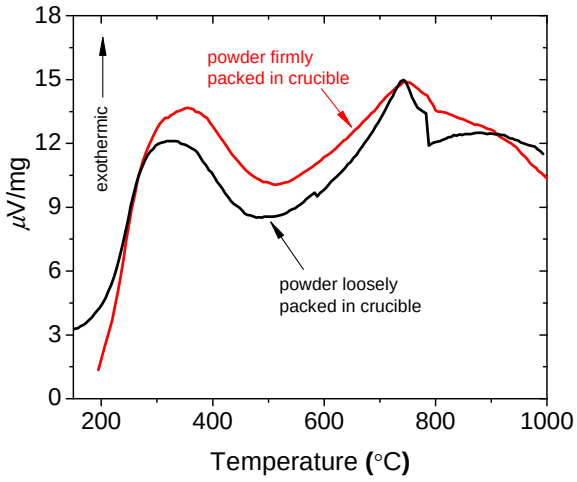

Figure 6.7. Thermal behavior of hydrogen-terminated silicon nanoparticles up to 1000 °C. Heating rates were 25 K/min.

Several representative TEM images recorded after heating particles in flight are shown in Figures 6.8 and 6.9. Figure 6.8 shows lower magnification images and Figure 6.9 shows higher magnification images. Without heating (23 °C) the most probable primary particle size is ~5 nm, the particle size distribution appears fairly narrow ($\sigma_g \approx$ 1.22 based on representative TEM images), and particles are essentially spherical. Crystallinity is also widely apparent as suggested by numerous particles in the appropriate orientation to exhibit lattice fringes. Defects in particle cores, if present, are not obvious. Up to ~500 °C, changes in the structural morphology of individual particles are difficult to discern, and particles appear similar to those that were not heated in the furnace. At temperatures near 500 and 550 °C, however, lattice fringes do not extend as close to the particle surfaces as they do in particles heated to lower temperatures. At 600 °C particles show distinct signs of sintering. Nonspherical particles and crystalline domains similar in size to the original 5 nm particles are visible. At 650 °C, increasingly complex structures evolve. Images show sintered aggregates that are probably composed of several primary particles. The aggregates also appear to be a combination of amorphous and crystalline regions. At 700 °C, the aggregates exhibit less complex shapes. Polycrystallinity is evident in most structures larger than the original 5 nm primary particles. For example, the particle formed at 700 °C shown in Figure 6.9 exhibits several regions of differently-oriented, but locally-aligned lattice fringes. A distinct transition from the irregular shapes to more compact, spheroidal structures occurs near 750 °C. At this temperature the larger particles are still polycrystalline, but smaller particles tend towards single-crystalline and spherical. As the temperature is increased from 750 to 1000 °C the larger particles evolve from spheroidal and polycrystalline to

spherical and single-crystalline. With few exceptions the particles are single-crystalline at 1000 °C, and defects, when present, are twin boundaries occurring at particle mid-planes as shown in the inset of Figure 6.9.

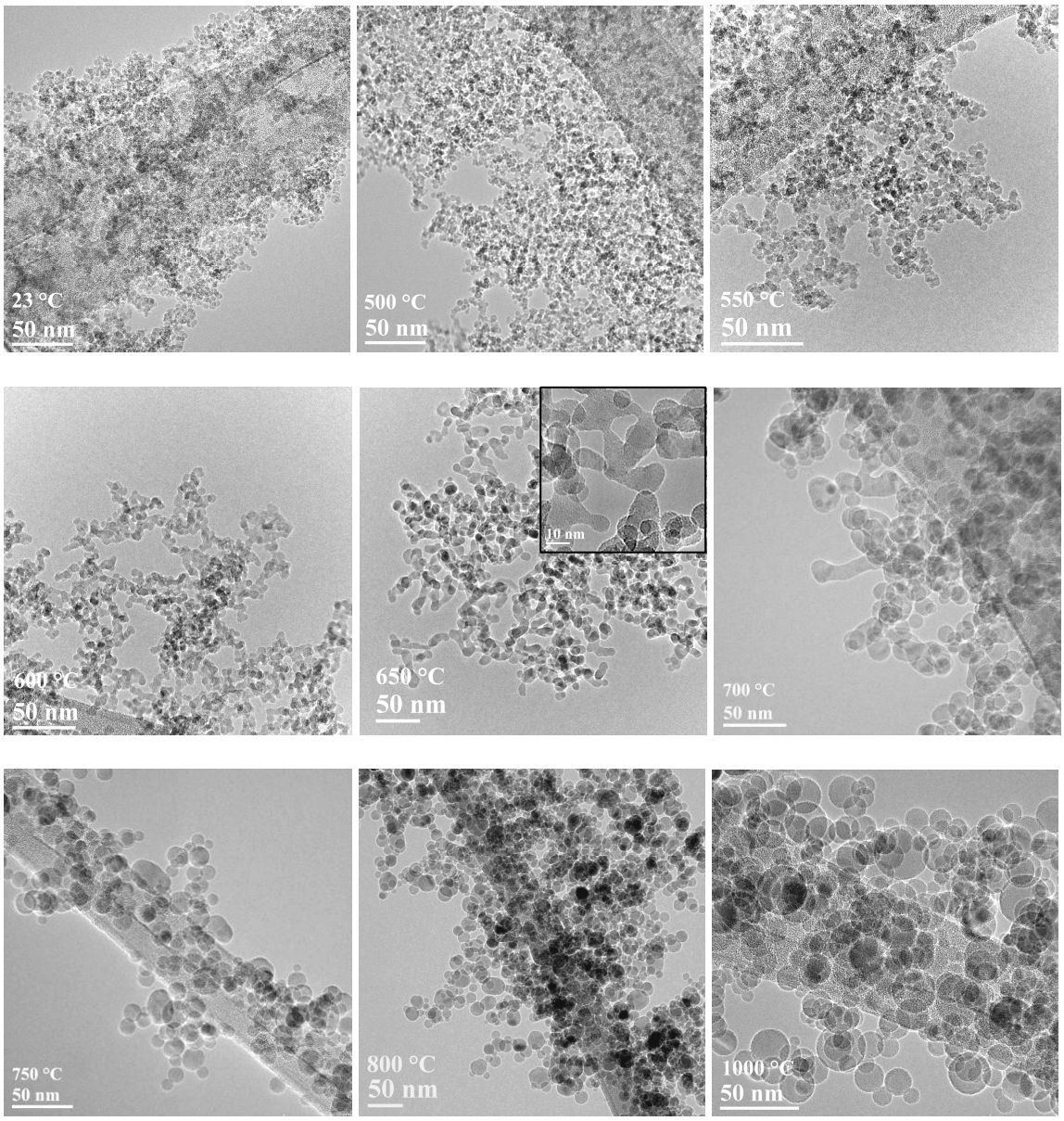

Figure 6.8. Representative low magnification TEM images of particles heated to temperatures ranging from room temperature to 1000 °C. Furnace temperature set points are shown in the images.

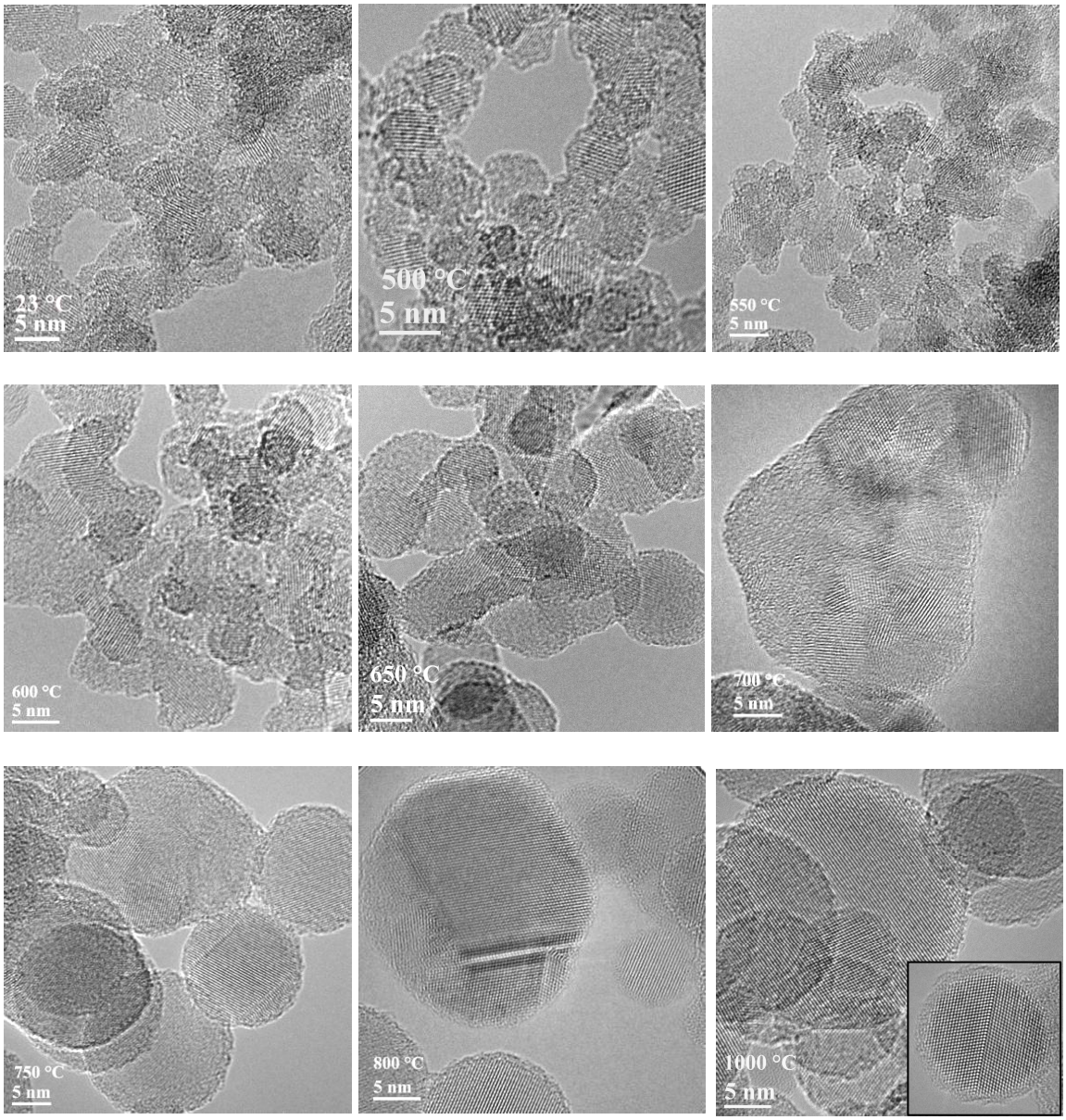

Figure 6.9. Representative high magnification TEM images of particles heated to temperatures ranging from room temperature to 1000 °C. Furnace temperature set points are shown in the images.

6.4 Discussion

Particles synthesized in the plasma reactor were hydrogen-terminated, spheroidal, and single crystalline. The TEM images recorded of unheated particles (23 °C) showed that particles exiting the plasma reactor exhibited low size dispersity and that most particles were between 4 and 6 nm in diameter. Internal defects were not observed in images of unheated particles. XRD results also indicated that fresh, unheated particles exhibited an average equivalent diameter of ~5 nm. The surface composition of unheated particles consisted of a complex mixture of silicon-hydrogen functional groups as demonstrated by the multi-band infrared absorption spectrum of Figure 6.3a. Although individual absorption peaks were not deconvolved, isolated SiH, SiH_2, SiH_3, clustered states, dimerized structures, and other polyhydrides all probably contribute to the spectra of unheated particles.[6.21-6.25]

Distinct changes in surface composition and structural morphology were observed as the particles were heated. Changes primarily occurred in three temperature ranges which are hereafter referred to as low (< 500 °C), medium (500 – 750 °C) and high (> 750 °C). The ranges were primarily defined in terms of silicon hydride functional group signatures that appear in the FTIR spectra. In the low temperature range particles exhibited absorptions in both the silicon-hydrogen stretching and deformation regions; in the medium temperature range particles only exhibited absorptions in the stretching region; and in the high temperature range particles did not exhibit infrared absorptions. Particle residence times in the tube furnace were different at each temperature setting due to gas expansion effects. For example, in the low temperature range, average residence times were estimated to be ~150 ms at room temperature and ~14 ms at 500 °C. At 750

°C the average residence time was ~9 ms, and at 1000 °C the residence time was less than 7 ms.

In the low temperature range, silicon hydride composition changes were readily apparent as the particles were heated to increasingly higher temperatures, but structural morphology changes were subtle. The images of Figures 6.8 and 6.9 indicate that the spherical shapes characteristic of unheated particles persisted throughout the low temperature range. FTIR spectra of Figure 6.3a showed that absorptions occurred in both the silicon-hydrogen stretching and deformation regions up to ~450 °C. At ~500 °C, however, the most intense absorptions occurred near 2083 and 2100 cm^{-1}, and no absorptions occurred in the silicon-hydrogen deformation region. Note that peaks appearing between 820 and 950 cm^{-1} are typically associated with deformation modes of higher order hydrides like SiH_2, SiH_3, and other silicon hydride structures.[6.22-6.24] Peaks in this region have not been associated with silicon monohydride (SiH) functional groups. Therefore, the peaks at ~2083 and 2100 cm^{-1} are probably due to SiH functional groups, but further consideration is warranted (*vide infra*). In light of this comment, however, infrared absorptions at ~2083 cm^{-1} have been attributed to strain-free SiH at Si(111) surfaces,[6.21] and absorptions at ~2100 cm^{-1} have been attributed to strained SiH at Si(100) 2×1 surfaces.[6.26] Alternatively, a common origin for the peaks at 2083 and 2100 cm^{-1} has been proposed.[6.27] In that report, hydrogentated microcrystalline silicon films were annealed while changes in the infrared signatures were monitored. As was shown, two sharp absorptions evolved in the Si–H stretching region at 2083 and 2100 cm^{-1} with heating. The evolved lineshapes and peak locations are similar to those observed in this chapter. The authors of that report concluded that hydrogen predominantly existed in

silicon monohydride functional groups at Si(111) surfaces, and that the doublet was due to optical anisoptropy of the SiH monolayers. The asymmetry on the low wavenumber side of the peak at 2083 cm^{-1} in Figure 6.3 suggests a superposition of absorptions from additional SiH functional groups in different structural environments.

A prominent exothermic transition is also observed in the low temperature range. In both traces of Figure 6.7, the center of the low temperature exothermic transition is near 350 °C. Exothermic transitions at similar temperatures have been experimentally observed of hydrogenated amorphous silicon,[6.28-6.29] porous silicon,[6.24] and polymorphous silicon.[6.30] They were attributed to effects associated with hydrogen desorption. Molecular dynamics simulations of hydrogen-terminated silicon nanoparticles have also demonstrated that hydrogen evolves from silicon nanocrystal surfaces in the same temperature range.[6.31] The exothermic transition centered near 350 °C correlates well with the disappearance of absorptions due to higher hydrides in the FTIR spectra of Figure 6.3a. These phenomena are likely related, and the exothermic transition can therefore be attributed to effects associated with hydrogen desorption.

Near the boundary between the low and medium temperature ranges, subtle changes in equivalent particle size accompany the hydrogen desorption. As suggested by Figure 6.6, particles heated in flight at 7 Torr and particles heated in powder form at atmospheric pressure both exhibit small reductions in the size of coherently diffracting crystalline domains after heating to 500 °C. This phenomenon is further demonstrated in Figure 6.10 which shows a high magnification image recorded of particles that were heated to 500 °C in the flow tube furnace. The image shows a crystalline particle core surrounded by what appears to be a less ordered outer shell. Based only on representative

TEM images it is not possible to deduce whether the disorganized outer layer is composed of amorphous silicon or silicon oxide. The FTIR and DSC results imply that some of the surface hydrogen has desorbed by 500 °C, and therefore that highly reactive unsatisfied silicon bonds probably exist at the particle surfaces. If this is the only phenomenon that occurs with heating one might hypothesize that the heated particles would be more susceptible to oxidation in air than unheated particles. The disordered outer shell could therefore be easily attributed to oxidized silicon. However, preliminary results indicate that particles heated to 500 °C in a similar flow tube furnace oxidize more slowly when exposed to air at room temperature than particles heated to temperatures on either side of 500 °C.[6.32] Moreover, investigations of the thermal oxidation of hydrogen-terminated silicon nanoparticles in a similar flow tube apparatus have demonstrated that even in oxygen-rich conditions, heating particles at 500 °C is unlikely to result in formation of an oxide shell like that shown in Figure 6.10.[6.33] Since the particles were

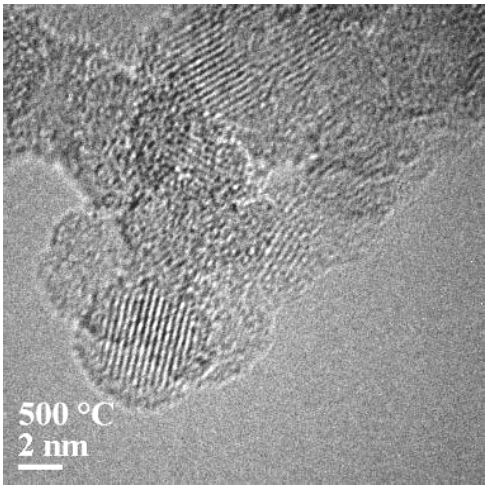

Figure 6.10. An image of particles heated in flight to 500 °C.

sealed at low pressure and transported between the synthesis reactor and the TEM in secondary containers filled with nonreactive gas, it is unlikely that extensive oxidation could have occurred. The disorganized outer shell is probably not largely composed of a stoichiometric or sub-stoichiometric silicon oxide.

An alternative explanation is that the disorganized outer shell is amorphous silicon, the formation of which is a consequence of the hydrogen desorption. It is well known that surface structures are highly coordination-dependent,[6.34] and according to computational simulations,[6.35] removing sufficient amounts of surface hydrogen from crystalline silicon nanoparticles induces reorganization of the diamond cubic structure to more compact, non-crystalline silicon structures. For example, in simulated annealings of hydrogen-terminated crystalline silicon nanoclusters, Yu et al. demonstrated that removal of 70-80% of the surface hydrogen during annealing caused the clusters to reorganize into more compact structures.[6.35] The results shown in Figure 6.4 are in agreement with their conclusion. Other experimental reports provide evidence in support of the simulations. For example, porous silicon, a material akin to hydrogen-terminated silicon nanoparticles in some respects, shows similar behavior at 500 °C.[6.24,6.36] Specifically, when porous silicon was heated in an inert environment, electron paramagnetic resonance techniques indicated a maximum concentration of unsatisfied silicon bonds at 500 °C. At the same temperature, XRD analysis indicated a maximum Si lattice contraction. In another report regarding silicon nanoparticles heated in flight, it was also proposed that hydrogen desorption resulted in a reduction of particle crystallinity.[6.19] Moreover, thin amorphous silicon films have demonstrated notable resistance to oxidation in air.[6.37] Together, these reports suggest that the particle surfaces

reconstruct after sufficient hydrogen desorption, and that the thin shell is probably composed of amorphous silicon with SiH surface functional groups and silicon atoms that are not coordinated to hydrogen.

Taken together, the results suggest that several related phenomena occur within the low temperature range. Hydrogen first desorbs, probably either as H_2 with silicon being incorporated into the particle, or as volatile silicon hydrides.[6.38] Once sufficient hydrogen has desorbed, the highly reactive dangling bonds induce reconstruction of the particle surfaces to more highly compact, less orderly structures. Although particle surfaces likely restructure to lower energy configurations, the crystalline interiors remain intact and particles retain their original spherical shapes. The persistent SiH functional groups at particle surfaces probably hinder extensive sintering in the low temperature range.

In the medium temperature range (500 – 750 °C), structural morphology changes were more apparent than chemical composition changes. Unlike the low temperature range where minimal sintering was observed, hydrogen desorption, sintering, and coalescence all occurred in the middle temperature range. As shown in Figure 6.3, SiH functional groups persisted at particle surfaces up to at least 700 °C, and both peaks in the Si–H stretching vibration region shifted to slightly lower wavenumbers and attenuated with increasing temperature. With increasing temperature, however, the peak at 2100 cm^{-1} attenuated more quickly than the peak at 2083 cm^{-1}. Changes in the relative peak intensities can be partially explained by the different SiH assignments suggested previously. Provided that surface hydrogen was not sufficiently isolated to make

hydrogen desorption unfavorable,[6.39] highly strained SiH functional groups (2100 cm^{-1}) would require less energy to desorb than unstrained SiH functional groups (2083 cm^{-1}).

The TEM images of Figure 6.8 and 6.9 indicate that particles retain their original spherical shapes up to ~550 °C. Although a disorganized silicon shell partially composed of dangling and floating silicon bonds,[6.40,6.41] and SiH functional groups probably exists at particle surfaces, it is difficult to discern from TEM images whether or not sintering has begun to occur. At 600 °C, however, the first distinct signs of sintering and coalescence are visible in the TEM images. Note that this temperature is close to the previously reported melting temperature of 5 nm diameter silicon particles.[6.2] A departure from the original discrete spherical primary particles is evident in the TEM images, and polycrystalline structures partially composed of single-crystalline regions larger than the original 5 nm primary particles are visible. As temperatures approach the upper end of the middle temperature range, rapid sintering occurs with minimal energy barrier in part because the hydrogen desorption has exposed numerous silicon surface radicals[6.16], and probably in part due to melting.[6.2]

XRD results in Figure 6.6 suggest that growth of coherently diffracting crystalline regions (i.e., particle growth) also occurs in the middle temperature range. Note that since the particles are no longer spherical, estimates of particle size based on the Scherrer equation are especially prone to error. The XRD results also indicate that equivalent average sizes of particles heated in flight are slightly different than particles heated in powder from. For example, particles heated in powder form exhibit consistently smaller equivalent crystallite sizes than particles heated in flight at the same temperature. The differences can be partially explained by considering how the particles are able to move

relative to each other during heating. On the one hand, the original 5 nm primary particles may be more highly coordinated to other primary particles in powder form than in aerosol form. Therefore, the relative motion of particles with higher coordination number could be more constrained than particles with lower coordination number. Particles heated in powder form are also in contact, either directly or indirectly, with a stationary substrate that can hinder the motion of coalescing aggregates. On the other hand, aggregates heated in flight, while also subject to the constraints of inter-particle coordination, are not bound to a substrate and are therefore able to tumble, twist, and bend to minimize the particle free surface area. The idea of constrained particle motion could partially explain the equivalent particle size differences in shown in Figure 6.6.

From a local minimum near 500 °C to the maximum near 750 °C, the DSC measurements of Fig. 6.7 indicated a gradually increasing exothermic trend in the middle temperature range. The exothermic behavior is consistent with effects associated with continued hydrogen desorption as suggested by the FTIR results, reduction in free particle surface area due to sintering, and the formation of larger crystalline domains due to coalescence and recrystallization as indicated by the representative TEM images.

In the high temperature range (> 750 °C), sintering and coalescence were extensive. As the FTIR spectra in Figure 3a imply, temperatures greater than ~700 °C were sufficient to eliminate the vast majority of hydrogen from particle surfaces. Therefore, as suggested by Hawa and Zachariah the sintering barrier imposed by hydrogen at particle surfaces is absent.[6.16] The sharp exothermic transition observed at ~750 °C in both DSC traces of Figure 6.7 coincides with the absence of hydrogen in the FTIR spectra. This exothermic transition can be partially attributed to rapid coalescence

of the geometrically complex structures that evolve as the particles are heated, and partly to crystallization. The TEM images of Figures 6.8 and 6.9 support this conclusion by showing that at ~750 °C the geometrically complex structures observed of the middle temperature range are no longer present. In another report describing silicon nanoparticles heated inside a TEM, rapid coalescence was also observed near 750 °C.[6.42] An explanation for the sharp drops in the DSC traces near 785 °C is not immediately apparent and requires further investigation. Although it cannot be assigned at this time, the drop is probably not an instrumental artifact since similar behavior was observed in many experiments and in another DSC apparatus.

Several questions regarding the interaction of hydrogen with the silicon particle structure during heating remain unanswered. For example, are sintering and coalescence hindered by the surface hydrogen? This question cannot be definitively answered from the data shown here and requires a more detailed study of the relevant kinetics. However, consider the heating rates experienced by the particles as they were heated in flight in the tube furnace compared to the heating rates of the DSC and XRD experiments. The in flight heating rate is *significantly* faster than 50 K/min, yet the independent characterization techniques (FTIR, TEM, and DSC) demonstrated notable events at similar temperatures. Specifically, at ~750 °C the exothermic transition occurs almost simultaneously with coalescence of the remaining complex agglomerate shapes and also with the complete loss of surface hydrogen. However, if the particles melt at temperatures nearer to 580 °C as reported previously,[6.2] then why don't the sintered 'molten' particles/agglomerates coalesce into spherical shapes at lower temperatures? Perhaps the timescales and temperatures of the low and middle temperature regions are

not sufficient to allow complete coalescence. Alternatively, SiH surface bonds may inhibit structural rearrangement necessary for coalescence. Since SiH bonds persist to temperatures well above 580 °C, surface hydrogen may enforce localized sp^3 silicon bonding near the particle surfaces. These localized structures could hinder coalescence by inhibiting rearrangement of silicon surface atoms that is necessary for coalescence.[6.17]

Assuming that desorption of surface hydrogen elicits the formation of amorphous silicon shells that surround the crystalline particle cores, how can one come to terms with assigning the infrared absorption bands at 2083 and 2100 cm^{-1} to vibrations associated with crystalline surfaces? The previous peak assignments cannot be definitive since no evidence of surface faceting was apparent in the images of heated particles. However, first principles electronic structure calculations have shown that small silicon clusters ($n < 50$) with four-fold coordinated inner atoms can exhibit features resembling low energy surface reconstructions associated with stable silicon surfaces such as Si(111).[6.43] The larger particles and agglomerates considered here would probably be able to exhibit similar low energy surface reconstructions due to the substantial manifold of possible surface structures. An equally relevant concern with the peak assignments is that hydrogen could exist at the sub-surface and/or dissolved within particle/agglomerate interiors (i.e., in the 'bulk' of crystalline or amorphous regions). As the particles and agglomerates restructure, sinter, and coalesce, hydrogen could become trapped in voids and/or at grain boundaries within the polycrystalline particles. However, if sub-surface hydrogen or hydrogen in the bulk was present at detectable levels, dielectric screening effects[6.23,6.44] should cause absorption bands to appear at wavenumbers closer to 2000 cm^{-1}. No absorptions appear near 2000 cm^{-1} in any of the spectra of Figure 6.3. One

could also argue that the peak at 2100 cm^{-1} is due to SiH_2 functional groups commonly observed of hydrogenated amorphous silicon films.[6.45] However, if higher hydrides were present, additional peaks should appear between ~850 and 910 cm^{-1}. After heating to 500 °C, no absorptions were observed in the deformation region. Therefore, hydrogen probably does not largely exist in voids, in the bulk (crystalline or amorphous), or at interfaces between amorphous and crystalline silicon. Although the peaks at 2083 and 2100 cm^{-1} are difficult to assign to specific surfaces, the lineshapes and peak locations are more consistent with vibrations of SiH functional groups at surfaces than with bulk modes. That the peaks shift to slightly lower wavenumbers with increasing temperatures suggests that hydrogen coverage of the particle/agglomerate surfaces also decreases with increasing temperature.[6.44] Although the infrared peak assignments are not definite, one certainty observed in these experiments is that hydrogen persists at particle surfaces well above the experimentally reported melting temperature of 5 nm diameter silicon particles, and its effects should not be discounted. On the other hand, hydrogen does *not* exist at particle surfaces above ~750 °C, and in future investigations – both computational and experimental – the energetics of hydrogen desorption should not be disregarded.

6.5 Conclusion

Surface hydrogen plays important roles in the sintering and coalescing behavior of crystalline silicon nanoparticles. At temperatures below ~500 °C, surface hydrogen prevents interparticle reactions at the timescales of the experiments reported here. As the particles are heated to ~500 °C, hydrogen desorption occurs and disorganized particle shells form around crystalline silicon cores. However, sintering does not occur until

closer to 600 °C. Coalescence is also facilitated at that temperature, but minimal because of the persistent surface hydrogen. Temperatures of ~750 °C lead to desorption of all surface hydrogen thereby facilitating rapid sintering and coalescence into polycrystalline particles. At the time scales considered here, the largest single-crystalline particles formed from the sintering and coalescence of smaller primary particles are not obtained until temperatures of ~1000 °C are reached.

Chapter 7.

Conclusions and Recommendations for Future Work

The silicon nanoparticles synthesized in the reactor employed here present several benefits and challenges. Three benefits are immediately apparent. First, crystalline particles can be synthesized over a broad range of operating conditions. Second, the reactor can be configured to produce discrete, relatively size-monodisperse particles over a fairly broad range of particle sizes. Third, the particles are inherently hydrogen terminated when using silane as a particle precursor gas. The hydrogen adlayer is especially beneficial in that it can hinder inter-particle reactions such as sintering and coalescence, and other reactions such as uncontrolled particle oxidation, both of which are generally undesirable. Perhaps a more far-reaching benefit of the surface hydrogen, however, is that it can lend itself to sophisticated surface tailoring schemes based on different reactions. To that end, parts of this work have shown that the plasma reactor can synthesize particles with surfaces comprised of different silicon hydride functional groups that may be more amenable to surface tailoring by hydrosilylation.

The plasma reactor and the silicon nanoparticles synthesized therein still present several challenges before optimal synthesis conditions and effective post-synthesis particle surface tailoring schemes can be implemented. For example, even though particles with crystalline cores can be synthesized under different plasma operating conditions, the surfaces are not necessarily well organized. One potential solution to this problem is to heat the particles after synthesis. Reorganization of particle surfaces to

lower energy configurations is possible through heating. However, particle modification schemes that are based on thermal activation/promotion also present their own set of unique challenges. It has been shown that at temperatures as low as 200 °C, particle surface restructuring is probable when particles are heated in refluxing 1-dodecene. At slightly higher temperatures (300–350 °C) desorption of hydrogen and other poly-(silicon) hydrides can occur, and disorganized particle surfaces can restructure. Because the desorption of surface hydrogen and silicon hydrides can lead to undesirable effects such as loss of crystallinity, creation of highly reactive dangling bonds, and particle sintering and coalescence, post-synthesis processing temperatures should be minimized where possible.

While aerosol reactors present several benefits over solution/liquid based reactors, a disadvantage with aerosol systems compared to liquid based reactions is the limited reaction times. This is especially apparent when applying hydrosilylation reactions to nanoparticles. For example, it takes ~15 minutes for refluxing solutions of particles and 1-dodecene to change from cloudy to clear at ~200 °C. If one considers this amount of time an approximate measure of monolayer formation time (at a temperature that does not significantly alter the desirable particle properties), then aerosol reactors might not be appropriate for modifying hydrogen-terminated silicon nanoparticles by hydrosilylation. Even if a flow tube reactor providing 15 minutes residence time could be built, one only has to consider that particles smaller than 5 nm in diameter are especially prone to diffusion, and therefore that many, if not all, particles will be lost to the walls in such a reactor. The conclusion is that aerosol flow tube reactors work well for reactions such as

thermal oxidation which occur quickly. However, reactions which require more time may not be appropriate for aerosol systems.

Suggestions for further research regarding functionalizing silicon nanoparticles with 1-alkenes/1-alkynes and coating particles with other materials are as follows. While high particle mass yield from the plasma reactor is an obvious goal, and has been previously pursued, a more appropriate long term goal may be better control of the particle surfaces. In regard to the hydrosilylation reaction, particles surfaces should be primarily covered by silicon monohydride functional groups. It has been shown that particles with this property can be synthesized in the plasma. However, one also needs to consider what happens to the particle surfaces during and after hydrosilylation to determine whether or not this is an appropriate functionalization strategy. A brief consideration of the proposed radical chain mechanism scheme suggests that one outcome of the reaction is highly reactive dangling bonds which, among other things, are thought to be detrimental to photoluminescent properties. Moreover, steric limitations prevent the attachment of long-chain hydrocarbon molecules to each silicon surface atom. In many applications, contact with air and water is inevitable. Therefore the silicon radicals induced by hydrosilylation and the remaining silicon hydride functional groups will almost certainly react with water to form silicon oxides. If oxide formation is acceptable in end applications, then hydrosilylation should continue to be pursued as a feasible surface modification scheme. If oxide formation is not acceptable (e.g., when attempting to create light emitting devices that display colors spanning the visible spectrum without eventual shift of the colors towards red), then other passivating techniques should be pursued.

Bibliography.

Chapter 2

(2.1) Hua, F.; Erogbogbo, F.; Swihart, M. T.; Ruckenstein, E. *Langmuir* **2006**, *22*, 4363.

(2.2) Nayfeh, M. H.; Rogozhina, E. V.; Mitas, L. *Synthesis, Functionalization and Surface Treatment of Nanoparticles* **2003**, 173.

(2.3) Ding, Y.; Dong, Y.; Bapat, A.; Deneen, J.; Carter, C. B.; Kortshagen, U. R.; Campbell, S. A. *Proceedings of SPIE-The International Society for Optical Engineering* **2005**, 6002.

(2.4) Roca i Cabarrocas, P.; Chaabane, N.; Kharchenko, A. V.; Tchakarov, S. *Plasma Phys. Contr. F.* **2004**, *46*, B235.

(2.5) Buriak, J. M. *Chem. Rev.* **2002**, *102*, 1271.

(2.6) Rogozhina, E.; Belomoin, G.; Smith, A.; Abuhassan, L.; Barry, N.; Akcakir, O.; Braun, P. V.; Nayfeh, M. H. *Appl. Phys. Lett.* **2001**, *78*, 3711.

(2.7) Bent, S. F. *Surf. Sci*. **2002**, *500*, 879.

(2.8) Wang, G. T.; Mui C.; Musgrave C. B.; Bent S. F. *J. Am. Chem. Soc.* **2002**, *124*, 8990.

(2.9) Rader, D. J.; McMurry, P. H. *J. Aerosol Sci.* **1986**, *17*, 771.

(2.10) Kuhn, T.; Krudysz, M.; Zhu, Y.; Fine, P. M.; Hinds, W. C.; Froines, J.; Sioutas, C. *J. Aerosol Sci.* **2005**, *36*, 291.

(2.11) Liao, Y. C.; Nienow, A. M.; Roberts, J. T. *J. Phys. Chem. B* **2006**, *110*, 6190.

(2.12) Liao Y.C.; Roberts J. T. *J. Am. Chem. Soc.* **2006**, *128*, 9061.

(2.13) Biswas, R.; Pan, B. C. *Mater. Res. Soc. Symp. Proc.* **2004**, *808*, 65.

(2.14) Gupta, P.; Colvin, V. L.; George, S. M. *Phys. Rev. B* **1988**, *37*, 8234.

(2.15) Niwano, M.; Terashi, M.; Kuge, J. *Surf. Sci.* **1999**, *420*, 6.

(2.16) Mangolini, L.; Thimsen, E.; Kortshagen, U. *Nano Lett.* **2005**, *5*, 655.

(2.17) Jurbergs, D.; Rogojina, E.; Mangolini, L.; Kortshagen, U. *Appl. Phys. Lett.* **2006**, *88*, 233116.

(2.18) Chen, D. R.; Pui, D. Y. H. *J. Nanoparticle Res.* **1999**, *1*, 115.

(2.19) Karg, E.; Dua, S. K.; Ferron, G. A. *J. Aerosol Sci.* **1992**, *23*, S389.

(2.20) Higgins, K. J.; Jung, H.; Kittelson, D. B.; Roberts, J. T.; Zachariah, M. R. *J. Phys. Chem. A* **2002**, *106*, 96.

(2.21) Schmid, O.; Trueblood, M. B.; Gregg, N.; Hagen, D. E.; Whitefield, P. D. *Aerosol Sci. Tech.* **2002**, *36*, 51.

(2.22) Marra, D. C.; Edelberg, E. A.; Naone, R. L.; Aydil, E. S. *J. Vac. Sci. Tech. A* **1998**, *16*, 3199.

(2.23) Chabal, Y. J. *Physica B* **1991**, *170*, 447.

(2.24) Ogata, Y. H.; Kato, F.; Tsuboi, T.; Sakka, T. *J. Electrochem Soc.* **1998**, *145*, 2439.

(2.25) Sperveslage, G.; Grobe, J.; Egbers, G.; Benninghoven, A. *Fresenius J. Anal. Chem.* **1998**, *361*, 554.

(2.26) Buriak, J. M. *Chem. Rev.* **2002**, *5*, 1272.

(2.27) Joshipura, K. N.; Vinodkumar, M.; Antony, B. K.; Mason, N. J. *Eur. Phys. J. D* **2003**, *23*, 81.

(2.28) Doren, D. J. In *Advances in Chemical Physics*; Progogine, I. and Rice, S. A., Eds.; John Wiley and Sons: Hoboken, NJ, 1996; Vol. 95.

(2.29) Hofmeister, H.; Dutta, J.; Hofmann, H. *Phys. Rev. B* **1996**, *54*, 2856.

(2.30) Marra, D. C.; Edelberg, E. A.; Naone, R. L.; Aydil, E. S. *Appl. Surf. Sci.* **1998**, *133*, 148.

(2.31) Williams, D. B.; Carter, C. B. *Transmission Electron Microscopy*; Springer: New York, 1996.

(2.32) Hinds, W. C. *Aerosol Technology: Properties, Behavior, and Measurement of Airborne Particles 2nd Ed.*; Wiley: New York, 1999.

(2.33) DeCarlo, P. F.; Slowik, J. G.; Worsnop, D. R.; Davidovits, P.; Jimenez, J. L. *Aerosol Sci, Tech.* **2004**, *38*, 1185.

(2.34) Gates, S. M.; Kunz, R. R.; Greenlief, C. M. *Surf. Sci.* **1989**, *207*, 364.

(2.35) Farjas, J.; Das, D.; Fort, J.; Roura, P.; Bertran, E. *Phys. Rev. B* **2002**, *65*, 115403/1.

(2.36) Mahan, A. H.; Beyer, W.; Williamson, D. L.; Yang, J.; Guha, S. *Philos. Mag. Lett.* **2000**, *80*, 647.

(2.37) Chang, K. J.; Chadi, D. J. *Phys. Rev. B* **1990**, *42*, 7651.

(2.38) Yu, D. K.; Zhang, R. Q.; Lee, S. T. *J. Appl. Phys.* **2002**, *92*, 7453.

(2.39) Yu, D. K.; Zhang, R. Q.; Lee, S. T. *Phys. Rev. B* **2002**, *65*, 245417.

Chapter 3

(3.1) (a) Deal, B. E.; Grove, A. S. *J. Appl. Phys.* **1965**, *36*, 3770. (b) Helms, C. R. and Deal, B. E., eds., *The Physics and Chemistry of SiO_2 and the Si-O_2 Interface*; Plenum: New York, 1988. (c) Pantelides, S. T. ed. *The Physics of SiO_2 and its Interfaces*; Pergamon: New York, 1978.

(3.2) Chabal, Y. J.; Weldon, M. K.; Queeney, K. T.; Esteve, A. In *Fundamental Aspects of Silicon Oxidation*; Chabal, Y.J. ed.; Springer-Verlag: New York, 2001; pp 143-160.

(3.3) Ding, Y.; Dong, Y.; Bapat, A.; Deneen, J.; Carter, C. B.; Kortshagen, U. R.; Campbell, S. A. *Proc. of SPIE-The International Society for Optical Engineering* **2005**, *6002*, 60020I/1-60020I/7.

(3.4) Hua, F.; Erogbogbo, F.; Swihart, M. T.; Ruckenstein, E. *Langmuir* **2006**, *22*, 4363.

(3.5) Pi, X. D.; Mangolini, L.; Campbell, S. A.; Kortshagen, U. *Phys. Rev. B* **2007**, *75*, 085243.

(3.6) Nayfeh, M. H.; Rogozhina, E. V.; Mitas, L. in *Synthesis, Functionalization and Surface Treatment of Nanoparticles*, Baraton, M. I. ed.; American Scientific: Stevenson Ranch, CA, 2003.

(3.7) Roca i Cabarrocas, P.; Chaabane, N.; Kharchenko, A. V.; Tchakarov, S. *Plasma Phys. Contr. F.* **2004**, *46*, B235.

(3.8) Heitmann, J.; Mueller, F.; Zacharias, M.; Goesele, U. *Adv. Mater.* **2005**, *17*, 795.

(3.9) Liu, H. I.; Biegelson, D. K.; Ponce, F. A.; Johnson, N. M.; Pease, R. F. W. *Appl. Phys. Lett.* **1994**, *64*, 1383.

(3.10) Ostraat, M. L.; Brongersma, M.; Atwater, H. A.; Flagan, R. C. *Solid State Sci.* **2005**, *7*, 882.

(3.11) (a)Brongersma, M. L.; Polman, A.; Min, K. S.; Boer, E.; Tambo, T.; Atwater, H. *Appl. Phys. Lett.* **1998**, *72*, 2577-2579. (b)Shimura, T.; Yasutake, K.; Umeno, M.; Nagase, M. *Appl. Phys. Lett.* **2005**, *86*, 071903.

(3.12) Jurbergs, D.; Rogojina, E.; Mangolini, L.; Kortshagen, U. *Appl. Phys. Lett.* **2006**, *88*, 233116/1.

(3.13) Mangolini, L.; Thimsen, E.; Kortshagen, U. *Nano Lett.* **2005**, *5*, 655.

(3.14) Liao, Y. C.; Nienow, A. M.; Roberts, J. T. *J. Phys. Chem. B* **2006**, *110*, 6190.

(3.15) Rader, D. J. and McMurry, P. H. *J. Aerosol Sci.* **1986**, *17*, 771.

(3.16) Hinds, W. C. *Aerosol Technology*, 2nd ed.; John Wiley and Sons: New York, 1999.

(3.17) McMurry, P. H. *Atmospheric Environment* **2000**, *34*, 1959.

(3.18) Chen, D. R.; Pui, D. Y. H. *J. Nanoparticle Res.* **1999**, *1*, 115.

(3.19) Nienow, A. N.; Roberts, J. T.; Zachariah, M. R. *J. Phys. Chem. B* **2005,** *109*, 5561.

(3.20) Higgins, K. J.; Jung, H.; Kittelson, D. B.; Roberts, J. T.; Zachariah, M. R. *J. Phys. Chem. A* **2002**, *106*, 96.

(3.21) Holm, J. and Roberts, J. T. *J. Am. Chem. Soc.* **2007**, *129*, 2496.

(3.22) Marra, Denise C.; Edelberg, Erik A.; Naone, Ryan L.; Aydil, Eray S. *J. Vac. Sci. & Tech., A* **1998**, *16*, 3199.

(3.23) (a) Jackson, W. B.; Nickel, N. H.; Johnson, N. M.; Pardo, F.; Santos, P. V. *Mat. Res. Soc. Symp. Proc.* **1994**, *336*, 311. (b) Rivolo, P.; Geobaldo, F.; Rocchia, M.; Amato, G.; Rossi, A. M.; Garrone, E. *Phys. Stat. Sol. A* **2003**, *197*, 217. (c) John, P.; Odeh, M.; Thomas, M. J. K.; Tricker, M. J.; McGill, J.; Wallace, A.; Wilson, J. I. B. *J. Non-Cryst. Sol.* **1980**, *35-36*, 237.

(3.24) Das, D.; Farjas, J.; Roura, P.; Viera, G.; Bertran, E. *Appl. Phys. Lett.* **2001**, *79*, 3705.

(3.25) Pai, P. G.; Chao, S. S.; Tagaki, Y.; Lucovsky, G. *J. Vac. Sci. Tech. A* **1986**, *4*, 689.

(3.26) Stefanov, B. B.; Gurevich, A. B.; Weldon, M. K.; Raghavachari, K.; Chabal, Y. *J. Phys. Rev. Lett.* **1998**, *81*, 3908.

(3.27) Lambers, J. and Hess, P. *J. Appl. Phys.* **2003**, *94*, 2937.

(3.28) Weldon, M. K.; Queeney, K. T.; Chabal, Y. J.; Stefanov, B. B.; Raghavachari, K. et al., *J. Vac. Sci. Tech. B* **1999**, *17*, 1795.

(3.29) Queeney K. T.; Chabal, Y. J.; Weldon, M. K.; Raghavachari, K. *Phys. Stat. Sol.* **1999**, *175*, 77.

(3.30) Queeney, K. T.; Weldon, M. K.; Chang, J. P.; Chabal, Y. J.; Gurevich, A. B.; Sapjeta, J.; Opila, R. L. *J. Appl. Phys.* **2000**, *87*, 1322.

(3.31) Gupta, P.; Dillon, A. C.; Bracker, A. S.; George, S. M. *Surf. Sci.* **1991**, *245*, 360.

(3.32) Petrova, E. A.; Bogoslovskaya, L. A.; Balagurov, L. A.; Kochoradze, G. I. *Mat. Sci. Eng.* **2000**, *B69-70*, 152.

(3.33) Walkup, R. E. and Raider, S. I. *Appl. Phys. Lett.* **1988**, *53*, 888.

(3.34) Liu, H. I.;Biegelsen, D. K.; Johnson, N. M.; Ponce, F. A.; Pease, R. F. *J. Vac. Sci. Technol. B* **1993**, *11*, 2532.

(3.35) Niwano, M. *Surf. Sci.* **1999,** *427-428*, 199.

(3.36) Marcus and Sheng, *Solid-State Science and Technology* **1982**, *129*, 1278.

(3.37) (a) Kao, D. B.; McVittie, J. P.; Nix, W. D.; Saraswat, K. C. *IEEE Trans. Elec. Dev.* **1988**, *ED-35*, 25. (b) Scheer, K. C.; Rao, R. A.; Muralidhar, R.; Bagchi, S.; Conner, J.; Lozano, L.; Perez, C.; Sadd, M.; White, B. E., Jr. *J. Appl. Phys*. **2003**, *93*, 5637. (c) Coffin, H. et al. *J. Appl. Phys*. **2006**, *99*, 044302.

(3.38) Tersoff, J.; Tu, Y.; Grinstein, G. *Appl. Phys. Lett.* **1998**, *73*, 2328.

Chapter 4

(4.1) Roca i Cabarrocas, P.; Chaabane, N.; Kharchenko, A. V.; Tchakarov, S. *Plasma Phys. Contr.F.* **2004**, 46, B235.

(4.2) Ligman, R. K.; Mangolini, L.; Kortshagen, U.; Campbell, S. A. *Appl. Phys. Lett.* **2007**, *90*, 061116.

(4.3) Swihart, M. T. In *Nanotechnology in Biology and Medicine: Methods, Devices, and Applications*; Tuan Vo Dinh, Ed.; CRC: Boac Raton, FL, 2007; Chapter 4.

(4.4) Jurbergs, D.; Rogojina, E.; Mangolini, L.; Kortshagen, U. *Appl. Phys. Lett.* **2006**, 88, 233116/1.

(4.5) Li, Z. F.; Ruckenstein, E. *Nano Lett*. **2004**, *4*, 1463.

(4.6) Linford, M.; Chidsey, C. *J. Amer. Chem. Soc*. **1993**, *115*, 12631.

(4.7) Cicero, R. L.; Chidsey, C. E. D.; Lopinski, G. P.; Wayner, D. D. M.; Wolkow, R. A. *Langmuir* **2002**, *18*, 305.

(4.8) Bateman, J. E.; Eagling, R. D.; Worrall, D. R.; Horrocks, B. R.; Houlton, A. *Angew.Chem., Int. Ed.* **1998**, *37*, 2683.

(4.9) Boukherroub, R.; Morin, S.; Wayner, D. D. M.; Lockwood, D. J. *phys. stat. sol. (a)* **2000**, *182*, 117.

(4.10) Buriak, J. M. *Chem. Rev.* **2002**, *102*, 1271.

(4.11) Nelles, J.; Sendor, D.; Ebbers, A.; Petrat, F. M.; Wiggers, H.; Schulz, C.; Simon, U. *Colloid Polym. Sci.* **2007**, *285*, 729.

(4.12) Zhang, X.; Neiner, D.; Wang, S.; Louie, A. Y.; Kauzlarich, S. M. *Nanotechnology* **2007**, *18*, 1.

(4.13) Coletti, C.; Marrone, A.; Giorgi, G.; Sgamellotti, A.; Cerofolini, G.; Re, N. *Langmuir* **2006**, *22*, 9949.

(4.14) Rogozhina, E. V.; Eckhoff, D. A.; Gratton, E.; Braun, P. V. *J. Mater. Chem.* **2006**, *16*, 1421.

(4.15) Lopinski, G. P.; Wayner, D. D. M.; Wolkow, R. A. *Nature* **2000**, *406*, 48.

(4.16) Kosuri, M. R.; Gerung, H.; Li, Qiming, L.; Han, S. M. *Langmuir* **2003**, *19*, 9315.

(4.17) de Smet, L.; Zuilhof, H.; Sudholter, E.; Lie, L.; Houlton, A.; Horrocks, B. *J. Phys Chem. B* **2005** *109*, 12021.

(4.18) Hattori, T.; Aiba, T.; Iijima, E.; Okube, Y.; Nohira, H.; Tate, N.; Katayama, M. *Appl. Surf. Sci.* **1996** (*104/105*) 323.

(4.19) Mangolini, L. M.; Thimsen, E.; Kortshagen, U. R. *Nano Lett.* **2005**, *5*, 655.

(4.20) Thornton, J.; Williams, R. *Physica Scripta* **1990**, *41*, 1047.

(4.21) Fadley, C. S. *J. Electron Spectrosc. Relat. Phenom.* **1974**, *5*, 725.

(4.22) Burrows, V. A.; Chabal, Y. J.; Higashi, G. S.; Raghavachari, K.; Christman, S. B. *Appl.Phys. Lett.* **1988**, *53*, 998.

(4.23) Chabal, Y. J. In *Internal Reflection Spectroscopy: Theory and Applications*; Mirabella, F. M., Ed.; Marcel Decker: New York, 1993; Chapter 8.

(4.24) Toyoshima, Y.; Matsuda, A.; Arai, K. *J. Non–Cryst. Sol.* **1993**, *164–166*, 103.

(4.25) Belogorokhov, A. I.; Gavrilov, S. A.; Kashkarov, P. K.; Belogorokhov, I. A. *phys. stat. sol. (a)* **2005**, *202*, 1581.

(4.26) Palacios, W. D.; Koropecki, R. R.; Arce, R. D.; Busso, A. *Thin Solid Films* **2008**, *516*, 3729.

(4.27) Sun, X. H.; Wang, S. D.; Wong, N. B.; Ma, D. D. D.; Lee, S. T. *Inorg. Chem.* **2003,** *42*, 2398.

(4.28) Ogata, Y.; Niki, H.; Sakka, T.; Iwasaki, M. *J. Electrochem. Soc.* **1995**, *142*, 195.

(4.29) Boland, J. J. *Surf. Sci.* **1992**, *261*, 17.

(4.30) Bellamy, L, J. *The Infrared Spectra of Complex Molecules*; Chapman and Hall: London, 1975, pg. 29.

(4.31) Holm, J.; Roberts, J. T. *J. Amer. Chem. Soc.* **2007**, 129, 2496.

(4.32) Chidsey, C. E. D.; Loiacono, D. N. *Langmuir* **1990**, *6*, 682.

(4.33) Sieval, A. B.; Linke, R.; Zuilhof, H.; Sudhölter, E. J. *Adv. Mater.* **2000**, *12*, 1457.

(4.34) Sieval, A. B.; van den Hout; Zuilhof, H.; Sudhölter, E. J. *Langmuir* **2001**, *17*, 2172.

(4.35) Zhang, L.; Wesley, K.; Jiang, S. *Langmuir* **2001**, *17*, 6275.

(4.36) Yu, H.; Webb, L. J.; Ries, R. S.; Solares, S. D.; Goddard, W. A. III; Heath, J. R.; Lewis, N. S. *J.Phys. Chem. B* **2005**, *109*, 671.

(4.37) Snyder, R. G.; Strauss, H. L.; Elliger, C. A. J. Phys. Chem. **1982**, 86, 5145.

(4.38) Wright, N.; Hunter, M. *J. Amer. Chem. Soc.* **1947**, *69*, 803.

(4.39) Stewart, M. P.; Buriak, J. M. *J. Am. Chem. Soc.* **2001**, *123*, 7821.

(4.40) Hua, F.; Swihart, M. T.; Ruckenstein, E. *Langmuir*, **2005**, *21*, 6054.

(4.41) MacPhail, R. A.; Strauss, H. L.; Snyder, R. G.; Elliger, C. A. *J. Phys. Chem.* **1984**, *88*, 334.

(4.42) Carter, R. S.; Harley, S. J.; Power, P. P.; Augustine, M. P. *Chem. Mater.* **2005**, *17*, 2932.

(4.43) Lica, G.; Zelakiewicz, B. S.; Tong, Y. Y. *J. Electroanalytical Chem.* **2003**, *554-555*, 127.

(4.44) Templeton, A. C.; Wuelfing, W. P.; Murray, R. W. *Acc. Chem. Res.* **2000**, *33*, 27.

(4.45) Spectral Database for Organic Compounds SDBS, National Institute of Advanced Industrial Science and Technology, http://www.aist.go.jp/RIODB/SDBS/ (accessed March, 3, 2009)

(4.46) Glass, J. A.; Wovchko, E. A.; Yates, J. T. *Surf. Sci.* **1996**, *348*, 325.

(4.47) Miura, T.; Niwano, M.; Shoji, D.; Miyamoto, N. *J. Appl. Phys.* **1996**, *79*, 4373.

(4.48) Pinchas, S. and Laulicht, I. *Infrared Spectra of Labeled Compounds*; Academic: New York, 1971.

(4.49) Bateman, J. E.; Eagling, R. D.; Horrocks, B. R.; Houlton, A. *J. Phys. Chem. B* **2000**, *104*, 5557.

(4.50) Chabal, Y. J. *Physica B* **1991**, *170*, 447.

Chapter 5

(5.1) (a) Lam, C.; Zhang, Y. F.; Tang, Y. H.; Lee, C. S.; Bello I.; Lee, S. T. *J. Crystal Growth* **2000**, *220*, 466. (b) Wiggers, H.; Starke, R.; Roth, P. *Chem. Eng. & Tech.* **2001**, *24*, 261. (c) Zhang, X.; Neiner, D.; Wang, S.; Louie, A. Y.; Kauzlarich, S. M. *Nanotechnology* **2007**, *18*, 095601/1. (d) Dong, Y.; Bapat, A.; Hilchie, S.; Kortshagen, U.; Campbell, S. A. *J. Vac. Sci. Tech. B* **2004**, *22*, 1923.

(5.2) (a) Pi, X. D.; Liptak, R. W.; Nowak, J.; Wells, N.; Carter, B. C.; Campbell, S.; Kortshagen, U. *Nanotechnology* **2008**, *19*, 245603. (b) Roca i Cabarrocas, P.;

Nguyen-Tran, T.; Djeridane, Y.; Abramov, A.; Johnson, E.; Patriarche, G. *J. Phys. D Appl. Phys.* **2007**, *40*, 2258.

(5.3) Mangolini, L.; Thimsen, E.; Kortshagen, U. *Nano. Lett.* **2005**, *5*, 655.

(5.4) Girshick, S. L.; Hafiz, J. J. *J. Phys. D Appl. Phys.* **2007**, *40*, 2354.

(5.5) Ostraat, M. L.; De Blauwe, J. W.; Green, M. L.; Bell, L. D.; Atwater, H. A.; Flagan, R. C. *J. Electrochem. Soc.* **2001**, *148*, G265.

(5.6) Hawa, T.; Zachariah, M. R. *Phys. Rev. B* **2004**, *69*, 035417.

(5.7) Bent, S. *Surf. Sci.* **2002**, *500*, 879; Buriak, J. M. *Chem. Rev.* **2002**, *102*, 1271; Li, X.; He, Y.; Talukdar, S. S.; Swihart, M. T. *Langmuir* **2003**, *19*, 8490.

(5.8) Jurbergs, D.; Rogojina, E.; Mangolini, L.; Kortshagen, U. *Appl. Phys. Lett.* **2006**, *88*, 233116.

(5.9). Holm, J.; Roberts, J. T. *Langmuir* **2009**, *25*, 7050.

(5.10) Hua, F.; Swihart, M. T.; Ruckenstein, E. *Langmuir* **2005**, *21*, 6054; Gupta, A.; Swihart, M. T.; Wiggers, H. *Adv. Funct. Mater.* **2009**, *19*, 696.

(5.11) Sun, X.H.; Wang, S.D.; Wong, N.B.; Ma, D. D. D.; Lee, S. T. *Inorg. Chem.* **2003**, *42*, 2398.

(5.12) Ogata, Y.; Niki, H.; Sakka, T.; Iwasaki, M. *J. Electrochem. Soc.* **1995**, *142*, 195.

(5.13) Burrows, V.A.; Chabal, Y. J.; Higashi, G. S.; Raghavachari, K.; Christman, S. B. *Appl. Phys. Lett.* **1988**, *53*, 998.

(5.14) Drosd, R.; Washburn, J. *J. Appl Phys* **1982**, *53*, 397.

(5.15) (a) Fridman, A. A.; Boufendi, L.; Hbid, T.; Potapkin, B. V.; Bouchoule, A. *J. Appl. Phys.* **1996**, *79*, 1303. (b) Bouchoule, A. ed. *Dusty Plasmas: Physics, Chemistry, and Technological Impacts in Plasma Processing*; Chichester: New York, **1999**.

(c) Das, U. K.; Chaudhuri, P.; Kshirsagar, S. T. *J. Appl. Phys.* **1996**, *80*, 5389. (d) De Bleecker, K.; Bogaerts, A.; Goedheer, W.; Gijbels, R. *IEEE Trans Plasma Science* **2004**, *32*, 691. (d) Kortshagen, U. K.; Bhandarkar, U. V.; Swihart, M. T.; Girshick, S. L. *Pure Appl. Chem.* **1999**, *71*, 1871. (e) Lieberman, M. A.; Lichtenberg, A. J. *Principles of Plasma Discharges and Materials Processing; 2nd Ed.*; John Wiley & Sons: Hoboken, New Jersey, Chapter 17. (f) Swihart, M. T.; Girshick, S. L. *J. Phys. Chem. B* **1999**, *103*, 64.

(5.16) (a) Wang, X.; Zhang, R. Q.; Lee, S. T.; Frauenheim, T.; Niehaus, T. A. *Appl. Phys. Lett.* **2008**, *93*, 243120. (b) Yu, D. K.; Zhang, R. Q.; Lee, S. T. *J. Appl. Phys.* **2002**, *92*, 7453. (c) Pizzagalli, L.; Galli, G. *Mat. Sci. Eng. B* **2002**, *96*, 86.

(5.17) Marra, D. C.; Kessels, W. M.; van de Sanden, M.; Kashefizadeh, K.; Aydil, E.S. *Surf. Sci.* **2003**, *530*, 1.

(5.18) (a) Wautelet, M. *J. Phys.: Condens. Matter* **2004**, *16*, L163. (b) Silvestrelli, P.L.; Alavi, A.; Parrinello, M.; Frenkel, D. *Phys. Rev. B* **1997**, *56*, 3806.

(5.19) Van Vechten, J. A.; Tsu, R.; Saris, F. W. *Phys. Lett.* **1979**, *74A*, 422.

(5.20) Chabal, Y.J. *Physica B* **1991**, *170*, 400.

(5.21) Chabal, Y. J.; Raghavachari, K. *Phys. Rev. Lett.* **1984**, *53*, 282.

(5.22) (a) Burrows, M. Z.; Das, U. K.; Opila, R.L.; De Wolf, S.; Birkmire, R. W. *J. Vac. Sci. Technol. A* **2008**, *26*, 683. (b) Ogata, Y; Kato, F.; Tsuboi, T.; Sakka, T. *J. Electrochem. Soc.* **1998**, *145*, 2439.

(5.23) Holm, J.; Roberts, J. T. *J. Am. Chem. Soc.* **2007**, *129*, 2496.

(5.24) Vepřek, S.; Sarott, F. A. *Plasma. Chem. Plasma. Proc.* **1982**, *2*, 233.

(5.25) He, Y.; Yin, C.; Cheng, G.; Wang, L.; Liu, X.; Hu, G. Y. *J. Appl. Phys.* **1994**, *75*, 797.

Chapter 6

(6.1) Dutta, J.; Hofmann, H.; Houriet, R.; Hofmeister, H.; Hollenstein, C. *Colloids and Surfaces A* **1997** (*127*) 263.

(6.2) Goldstein, A. N. *Appl. Phys. A* **1996** (*62*) 33.

(6.3) Bet, S.; Kar, A. *Mat. Sci. Eng. B* **2006** (*130*) 228.

(6.4) Hawa, T.; Zachariah, M. R. *Aerosol Sci.* **2006** (*37*) 1-15.

(6.5) Kruis, F. E.; Kusters, K. A.; Pratsinis, S. E. *Aerosol Sci and Tech*. **1993** (*19*) 514.

(6.6) Frenkel, J. *J. Phys.* **1945** (*9*) 385.

(6.7) Friedlander, S. K.; Wu, M. K. *Phys. Rev. B* **1994** (*49*) 3622-3624.

(6.8) Hawa, T.; Zachariah, M. R. *J. Chem. Phys*. **2004** (*121*) 9043.

(6.9) Cho, K.; Biswas, P. *Aerosol Sci.* **2006** (*37*) 1378.

(6.10) Artelt, C.; Schmid, H.; Peukert, W. *J. Aerosol Sci.* **2005** (*36*) 147.

(6.11) Wautelet, M. *J. Appl. Phys., D* **1991** (*24*) 343.

(6.12) Mukherjee, D.; Sonwane, C. G.; Zachariah, M. R. *J. Chem. Phys.* **2003** (*119*) 3391.

(6.13) Tsantillis, S.; Pratsinis, S. E. *AIChE* **2000** (*46*) 407.

(6.14) Tsantillis, S.; Briesen, H.; Pratsinis, S. E. *Aerosol Sci. Tech.* **2001** (*34*) 237.

(6.15) (a) Olynick, D. L.; Gibson, J. M.; Averback, R. S. *Appl. Phys. Lett.* **1996** (*68*) 343. (b) Sakka, Y. and Uchikoshi, T. *Powder Metall.* **1993** (*36*) 179. (c) Sakka, Y.; Uchikoshi, T.; Ozawa, E. *J. Mater. Sci.* **1993** (*28*) 203.

(6.16) Hawa, T.; Zachariah, M. R. *Phys. Rev. B* **2004** (*69*) 035417.

(6.17) Hawa, T.; Zachariah, M. R. *Phys. Rev. B* **2005** (*71*) 165434.

(6.18) Mangolini L.; Thimsen E.; Kortshagen U. *Nano Lett.* **2005** (*5*) 655.

(6.19) Holm, J. and Roberts, J. T. *J. Amer. Chem. Soc.* **2007** (*129*) 2496.

(6.20) Langford, J.; Wilson, A. *J. Appl. Cryst.* **1978** (*11*) 102.

(6.21) (a) Chabal, Y. J. *Physica B* **1991** (*170*) 447. (b) Chabal, Y. J. In *Internal Reflection Spectroscopy: Theory and Applications*; Mirabella, F. M. Ed., Marcel Dekker: New York, 1993.

(6.22) Ogata, Y. H.; Kato, F.; Tsuboi, T.; Sakka, T. *J. Electrochem. Soc*. **1998** (*145*) 2439.

(6.23) Marra, D.; Edelberg, E.; Naone, R.; Aydil, E. *J. Vac. Sci. Tech. A* **1998** (*16*) 3199.

(6.24) Ogata, Y. H.; Yoshimi, N.; Yasuda, R.; Tsuboi, T.; Sakka, T. *J. Appl. Phys.* **2001** (*90*) 6487.

(6.25) Sun, X. H.; Wang, S. D.; Wong, N. B.; Ma, D. D. D.; Lee, T. S. *Inorg. Chem*. **2003** (*42*) 2398.

(6.26) Chabal, Y. J.; Raghavachari, K. *Phys. Rev. Lett.* **1984** (*53*) 282.

(6.27) Stryahilev, D.; Diehl, F.; Schröder, B.; Scheib, M.; Belogorokhov, A. *Philos Mag. B* **2000** (*80*) 1799.

(6.28) Roura, P.; Farjas, J.; Rath, C.; Serra-Miralles, J.; Bertran, E.; Roca i Cabarrocas, P. *Phys. Rev. B* **2006** (*73*) 085203.

(6.29) Battezzati, L.; Demichelis, F.; Pirri, C. F.; Tresso, E. *Physica B* **1992** (*176*) 73.

(6.30) Rath, C.; Farjas, J.; Roura, P.; Kail, F.; Roca I Cabarrocas, P.; Bertran, E. *J. Mater, Res.* **2005** (*20*) 2562.

(6.31) Biswas, R. and Pan, B. C. *Mat. Res. Soc. Symp. Proc.* **2004** (*808*) 65.

(6.32) Winters, B.; Holm, J.; Roberts, J. T. **2009** *in progress*.

(6.33) (a) Holm, J. and Roberts, J. T. *Langmuir* **2007** (*23*) 11217. (b) Liao, Y. C.; Nienow, A. N.; Roberts, J. T. *J. Phys. Chem. B* **2006** (*110*) 6190.

(6.34) Huang, W. J.; Sun, R.; Tao, J.; Menard, L. D.; Nuzzo, R. G.; Zuo, J. M. *Nature Materials* **2008** (*7*) 308.

(6.35) (a) Yu, D. K.; Zhang, R. Q.; Lee, S. T. *J. Appl. Phys.* **2002** (*92*) 7453. (b) Zhang, R. Q.; Costa, J.; Bertran, E. *Phys. Rev. B* **1996** (*53*) 7847.

(6.36) Chelyadinski, A. R. et al. *J. Electrochem. Soc*. **1997** (*144*) 1463.

(6.37) Mills, R.; Dhandapani, B.; He, J. *Solar Energy Mat. Solar Cells* **2003** (*80*) 1.

(6.38) John, P.; Odeh, M.; Thomas, M.; Tricker, M.; McGill, J.; Wallace, A.; Wilson, J. *J Non-Cryst. Sol.* **1980** (*35&36*) 237.

(6.39) Farjas, J.; Das, D.; Fort, J.; Roura, P.; Bertran, E. *Phys. Rev. B* **2002** (*65*) 115403.

(6.40) Da Silva, C.; Fazzio, A. *Phys. Rev. B* **2001** (*64*) 075301.

(6.41) Pantelides, S. T. *Phys. Rev. Lett.* **1986** (*57*) 2979.

(6.42) Schiering, G.; Thiessmann, R.; Wiggers, H.; Sudfield, D.; Ebbers, A.; Franke, D.; Witusiewicz, V.; Apel, M. *J. Appl. Phys.* **2008** (*103*) 084305.

(6.43) (a) Kaxiras, E. *Phys. Rev. Lett.* **1990** (*64*) 551. (b) Kaxiras, E. *Phys. Rev. B* **1997** (*56*) 13455.

(6.44) Cardona, M. *phys. stat. sol. b* **1983** (*118*) 463.

(6.45) Wagner, H.; Beyer, W. *Sol. St. Comm.* **1983** (*48*) 585.

Appendix A.

Summary of Particle Synthesis Conditions

Particles synthesized in three quartz plasma reactor tubes of 4, 7 and 10 mm i.d. were examined most thoroughly, but smaller and larger tubes were also employed. The effects of forward power were examined from ~10–90 W, but the ranges were limited depending on other settings. For example, if all other conditions were held constant, smaller diameter reactors were restricted to less forward power in order to keep the glow discharge contained within the quartz reactor tube as shown in Figure 5.1b. The effects of reactor pressure were examined at several values between 4 and 20 Torr. Electrode spacings were varied from ~6 to 90 mm. Different combinations of precursor gases were also examined under various other reactor settings, but gas flow rates were kept within 0–400 sccm argon, 10–100 sccm silane, and 0–20 sccm hydrogen.

Table A1. Ranges of plasma reactor control parameters.

Control Parameter	Reactor inner diameter		
	4 mm	7 mm	10 mm
Electrode spacing (mm)	6-90	6-90	6-90
Forward power (W)	5-40	16-90	30-90
Pressure (Torr)	4-15	4-20	7-20
Argon (sccm)	0-200	0-200	0-400
Silane (sccm)	10-80	5-80	5-80
Hydrogen (sccm)	0-20	0-20	0-20